

Titre: Characterization of an 8 x 8 Terahertz Photoconductive Antenna Array for Spatially Resolved Time-Domain Spectroscopy and Imaging Applications
Title:

Auteur: Raphaël Henri
Author:

Date: 2021

Type: Mémoire ou thèse / Dissertation or Thesis

Référence: Henri, R. (2021). Characterization of an 8 x 8 Terahertz Photoconductive Antenna Array for Spatially Resolved Time-Domain Spectroscopy and Imaging Applications [Mémoire de maîtrise, Polytechnique Montréal]. PolyPublie.
Citation: <https://publications.polymtl.ca/9966/>

 **Document en libre accès dans PolyPublie**
Open Access document in PolyPublie

URL de PolyPublie: <https://publications.polymtl.ca/9966/>
PolyPublie URL:

Directeurs de recherche: Maksim A. Skorobogatiy
Advisors:

Programme: Génie physique
Program:

POLYTECHNIQUE MONTRÉAL

Affiliée à l'Université de Montréal

**Characterization of an 8 x 8 Terahertz Photoconductive Antenna Array for
Spatially Resolved Time-domain Spectroscopy and Imaging Applications**

RAPHAËL HENRI

Département de génie physique

Mémoire présenté en vue de l'obtention du diplôme de *Maîtrise ès sciences appliquées*

Génie physique

Novembre 2021

© Raphaël Henri, 2021.

POLYTECHNIQUE MONTRÉAL

affiliée à l'Université de Montréal

Ce mémoire intitulé :

Characterization of an 8 x 8 Terahertz Photoconductive Antenna Array for Spatially Resolved Time-domain Spectroscopy and Imaging Applications

présenté par **Raphaël HENRI**

en vue de l'obtention du diplôme de *Maîtrise ès sciences appliquées*

a été dûment accepté par le jury d'examen constitué de :

Denis SELETSKIY, président

Maksim SKOROBOGATIY, membre et directeur de recherche

Caroline BOUDOUX, membre

DEDICATION

To my father and to my mother

À mon père et à ma mère

ACKNOWLEDGEMENTS

First of all, I would like to thank Professor Maksim Skorobogatiy for welcoming me into his research group and for advising me throughout my whole M.Sc. degree. I learned a lot under his supervision, and I am very grateful for his support. I would also like to thank Professor Denis Seletskiy and Professor Caroline Boudoux for reading and commenting my thesis.

I would like to thank my colleagues Ph.D. Kathirvel Nallappan, Ph. D. Hichem Guerboukha, Quentin Chapedelaine, Yang Cao, Guofu Xu and Mathieu Poulin for your precious help and advice. I'm grateful for all the interesting discussions that we had in the office on a wide variety of topics. I would like to thank Jean-Paul Lévesque and Yves Leblanc for their great technical assistance throughout the project.

Enfin, j'aimerais remercier ma famille pour leur soutien et pour leurs mots d'encouragement. Un merci spécial à mon père, sans qui rien de tout cela ne serait possible. Merci à ma copine Arielle Simard pour son amour et son soutien inconditionnel. Enfin, merci à mes deux frères Félix et Julien de me motiver à me dépasser constamment.

RÉSUMÉ

Le rayonnement térahertz (THz) a reçu beaucoup d'attention ces dernières années en raison de ses caractéristiques uniques. Sa capacité à pénétrer la plupart des matériaux diélectriques, sa nature non ionisante et le fait qu'il soit absorbé par les molécules d'eau en font un excellent choix pour les applications d'imagerie dans le domaine biomédical, en sécurité et bien plus encore. Le système de domaine temporel THz est l'un des systèmes d'imagerie les plus couramment utilisés où de courtes impulsions THz sont générées. Ces systèmes sont principalement utilisés en imagerie hyperspectrale, puisque toute l'information fréquentielle est acquise en un seul balayage. Selon le choix du détecteur, ces systèmes permettent une détection cohérente où les informations de phase et d'amplitude sont récupérées et trouvent des applications pratiques dans la caractérisation des matériaux.

L'un des principaux défis de l'imagerie cohérente avec un système THz dans le domaine temporel est le manque de détecteurs multipixels efficaces. L'approche la plus populaire consiste à utiliser une seule antenne photoconductrice (PCA) comme détecteur et à procéder à un balayage en 2 dimensions de l'objet ou du détecteur. Cette technique prend du temps et n'est pas adaptée à l'imagerie en temps réel. Dans ce travail, nous présentons une matrice d'antennes photoconductrices de 8x8 pixels pour des applications en spectroscopie et en imagerie dans le domaine temporel résolue spatialement. Le substrat du réseau PCA est composé de LT-GaAs et chaque antenne est séparée de 700 μm .

Dans un article publié dans IEEE Access intitulé : «Fabrication and characterization of an 8x8 terahertz photoconductive antenna array for spatially resolved time-domain spectroscopy and imaging applications», nous présentons une nouvelle technique où un modulateur spatial de lumière (SLM) est utilisé pour adresser chaque pixel de la matrice d'antennes. Le SLM est utilisé pour focaliser et diriger le faisceau infrarouge (IR) femtoseconde (fs) sur le gap de chaque antenne du détecteur. Pour ce faire, un patron de type lentille de Fresnel est affiché sur le SLM et une détection cohérente hyperspectrale est réalisée pour les 8 canaux du détecteur. De plus, un amplificateur virtuel de type lock in est implémenté dans *Labview* pour augmenter le signal sur bruit (SNR) de la matrice PCA.

Une technique de calibration complète utilisant un multimètre numérique et le rayonnement THz lui-même a été développée pour trouver la position optimale des antennes dans le référentiel du SLM. Une caractérisation du détecteur est proposée où des paramètres tels que le *crosstalk* entre les canaux et la résolution du détecteur sont déterminés. Finalement, des expériences d'imagerie d'un objet imprimé en 3D et d'un masque métallique sont réalisées avec succès.

ABSTRACT

Terahertz (THz) radiation has received a lot of attention in recent years due to its unique characteristics. Its ability to penetrate most dielectric materials, its non-ionizing nature, and the fact that it is absorbed by water molecules make it an excellent choice for imaging applications in the biomedical field, in security screening and much more. The THz time-domain system is one of the most common imaging systems where short THz pulses are generated. These systems are mainly used in hyperspectral imaging since the whole frequency information is acquired in a single scan. Depending on the choice of the detector, these systems allow coherent detection where both phase and amplitude information is retrieved and find practical applications in material characterization. One of the main challenges in coherent imaging with a THz time-domain system is the lack of efficient detector array. The most common approach is to use a single photoconductive antenna (PCA) as a detector and proceed with a 2D raster scan to image an object. This technique is time consuming and is not well-suited for real-time imaging. In this work, we present a PCA array of 8x8 pixels for spatially resolved time-domain spectroscopy and imaging applications. The substrate of the PCA array is made of LT-GaAs and each antenna is separated by 700 μm .

In an article published in *IEEE Access* entitled: "Fabrication and characterization of an 8x8 terahertz photoconductive antenna array for spatially resolved time-domain spectroscopy and imaging applications," we present a novel technique where a spatial light modulator (SLM) is used to address each pixel of the PCA array. The SLM is used to focus and steer the femtosecond (fs) infrared (IR) probe beam on the gap of each antenna of the detector. A Fresnel lens pattern is displayed on the SLM and hyperspectral coherent detection is achieved for the 8 channels of the detector. Furthermore, a multichannel virtual lock-in amplifier is implemented in *Labview* to increase the signal-to-noise (SNR) of the PCA array. A complete calibration technique using a digital multimeter and the THz radiation itself was developed to find the optimal position of the antennas in the SLM's referential. A characterization of the detector is proposed where parameters like channels' crosstalk and detector resolution are determined. Finally, imaging experiments of a 3D printed object and a metallic mask are successfully carried out.

TABLE OF CONTENTS

DEDICATION	III
ACKNOWLEDGEMENTS	IV
RÉSUMÉ.....	V
ABSTRACT.....	VII
TABLE OF CONTENTS	VIII
LIST OF TABLES	XI
LIST OF FIGURES.....	XII
LIST OF SYMBOLS AND ABBREVIATIONS	XV
CHAPTER 1 INTRODUCTION.....	1
CHAPTER 2 LITERATURE REVIEW.....	5
2.1 Terahertz time-Domain System	6
2.1.1 Photoconductive Antenna Emitter	7
2.1.2 Lock-in amplifiers	10
2.1.3 Extraction of optical parameters with coherent detection.....	14
2.1.4 Imaging applications with a THz time-domain system.....	16
2.2 Thermal Detectors	18
2.2.1 Golay Cells	18
2.2.2 Microbolometer Arrays	19
2.2.3 Pyroelectric Detectors	22
2.3 Photon Detectors	24
2.3.1 Photoconductive Antennas.....	24
2.3.2 Electro-Optic Detectors.....	27
2.3.3 Air Biased Coherent Detection	29

2.3.4	Schottky Barrier Photodiodes.....	30
2.3.5	Field Effect Transistor (FET) Detectors.....	32
2.3.6	Photomixers.....	33
2.4	Summary	34
CHAPTER 3	METHODOLOGY	37
3.1	Building a Classic THz time-Domain System	37
3.2	Implementing a virtual lock-in amplifier	38
3.3	Integrating the PCA array	40
3.4	Spatial Light Modulator Integration.....	41
CHAPTER 4	ARTICLE 1: FABRICATION AND CHARACTERIZATION OF AN 8 X 8 TERAHERTZ PHOTOCONDUCTIVE ANTENNA ARRAY FOR SPATIALLY RESOLVED TIME-DOMAIN SPECTROSCOPY AND IMAGING APPLICATIONS.....	45
4.1	Information.....	45
4.2	Authors.....	45
4.3	Abstract	46
4.4	Introduction.....	46
4.5	Design and fabrication of the Photoconductive Antenna array.....	50
4.6	THz Time-domain system with SLM-Driven parallelized acquisition	51
4.7	Calibration of the THz Photoconductive Antenna array.....	53
4.8	Imaging using the THz PCA array	58
4.9	Conclusion.....	64
4.10	Acknowledgment	65
CHAPTER 5	GENERAL DISCUSSION.....	66
CHAPTER 6	CONCLUSION.....	72

REFERENCES..... 74

LIST OF TABLES

Table 1. Parameter values for the study presented in Figure 2-3	9
Table 2 : Detectors for THz time-domain systems. (Coherent detection, Lock-in amplification, Frame per second (FPS), Signal to noise ratio (SNR), Noise equivalent power (NEP)	36
Table 3 : Main components of the THz time-domain system built.....	37

LIST OF FIGURES

Figure 1-1 Terahertz gap in the electromagnetic spectrum	2
Figure 2-1 Schematic diagram of a typical configuration for a THz time-domain system.....	6
Figure 2-2 Generation of THz pulses with a photoconductive antenna a) The fs pulse is focused on the gap of the antenna where a voltage bias is applied b) Photocarriers are generated and accelerated by the voltage bias c) Emission of a THz pulse.	7
Figure 2-3 Drude-Lorentz model simulation with <i>Matlab</i> for THz generation with a PCA emitter based on Ref. [20] a) THz pulse emitted in the time-domain. b) Frequency spectrum of the signal depicted in panel (a).....	10
Figure 2-4 Schematic representation of a dual-phase lock-in amplifier. Phase-locked loop (PLL), Low pass filter (LPF)	14
Figure 2-5. 46-year-old Caucasian woman diagnosed with infiltrating ductal carcinoma (IDC). a) Low-power pathology image used for correlation. b) THz time-domain image of the sample. c) Frequency-domain image at 1.5 THz. d) Frequency-domain image at 1.75 THz. e) Diagram of the pulsed THz system in the reflection imaging mode [35]	17
Figure 2-6 a) Principle of a gas Golay detector with the optical read-out system b) Schematic of a laser-driven wire-guided undulator for terahertz emission. The THz beam was collected by a pair of off-axis parabolas and focused onto a 1-mm-thick ZnTe crystal, or onto the Golay cell detector [58]	19
Figure 2-7 a) Schematic representation of THz bolometer detector b) Uncooled microbolometer camera MICROXCAM-384I-THZ from l’Institut National d’Optique (INO)[61]	20
Figure 2-8 a) Schematic of the real-time multichannel spectrometer with diffraction grating. b) Setup for the experiment. A high-power THz pulse source and a high-sensitivity THz camera were used. c) Frequency-resolved profiles of the THz beams obtained using the THz camera with bandpass filters (BPP) whose center frequency were 1.3 THz (top), 1.6 THz (middle), and 1.9 THz (bottom). d) Horizontal profile of the camera images integrated in the vertical direction. [66]	21

- Figure 2-9 . **a)** Schematic diagram of a typical pyroelectric detector[68] **b)** Pyroelectric camera *PyrocamTM III Series*[70].....22
- Figure 2-10 **a)** A linear array of 8 photoconductive antennas. **b)** THz waveforms measured simultaneously with an array of 8 photoconductive antennas and an array of 8 NOG1 amplifiers. (The offsets are arbitrary.) [84]25
- Figure 2-11 **a)** 16 channels photoconductive switch array **b)** Microlens array attached to the photoconductive switch array: schematic **c)** Simultaneous measurement of 16 ultrashort THz pulses (each pulse was shifted in time for 2 ps for a better overview) [18].....26
- Figure 2-12 **a)** Schematic diagram of the plasmonic photoconductive terahertz FPA **b)** Block diagram of the time-domain spectroscopy setup used for characterizing the fabricated plasmonic photoconductive terahertz FPA **c)** Optical microscopy image of the fabricated 9×7 plasmonic photoconductive terahertz FPA. The magnified section shows one pixel **d)** The time-domain electric field detected by a center and corner pixel of the FPA. The color plot of the FPA output (the color of each pixel represents the peak photocurrent pulse level detected at each pixel after normalization).27
- Figure 2-13 Schematic of EO detection method.....28
- Figure 2-14 Schematic setup of the terahertz real-time imaging system with balanced electro-optic (EO) detection. Abbreviations : Beam splitter (BS), Quarter-wave plate(QWP), Polarized beam splitter(PBS), Lens (L1,L2) [90].29
- Figure 2-15 **a)** THz detection with air biased coherent detection(ABCD)method [93] **b)** Schematic diagram of the experimental setup. A laser pulse from a Ti:sapphire regenerative amplifier is focused through a BBO crystal to generate its second harmonic, and generates a terahertz wave at the ionizing plasma spot. The terahertz and optical beams are separated by a sheet of ITO-coated glass, and recombined in the detection region after the optical beam is filtered and variably delayed. A 500 Hz electric field is applied to the generation region, supplying a second harmonic local oscillator for coherent detection via a photomultiplier tube [92]30
- Figure 2-16 In a Schottky photodiode, light is absorbed in the depletion region of an n-type semiconductor after passing through a semitransparent metallic film [98].31

Figure 2-17 a) Log-spiral antenna and zero-bias InGaAs Schottky diode form an ultrawideband detector.[99] b) Terahertz field intensities measured at 80 MHz pulse rate. Shown is a reference trace and pulses transmitted through three different samples (PA polyamide, GFC glass fiber composite) [95] c) Schematic of the measurement setup. RX broadband receiver (Schottky diode model 3DL 12C LS2500, ACST GmbH) [95].....	32
Figure 2-18 Schematic representation of a CW system with photomixer antennas for both emitter and detector.....	34
Figure 3-1 a) TERA8-1 PCA from Menlo System mounted on a PCB board b) Optomechanical mount T8-H2 from Thorlab c) Schematic representation of the gap of the PCA and a close look at the chip [113]	38
Figure 3-2 Schematic representation of the acquisition system.....	39
Figure 3-3 Schematic representation of the THz time-domain system with the PCA array mounted on a motorized 3D stage.....	40
Figure 3-4 a) Working principle of LCOS SLM b) Schematic representation of the setup in which the SLM is used with the PCA array.....	42
Figure 3-5 Phase function for thin lens, a Fresnel lens and a discretized multi-level phase lens ..	44
Figure 5-1 a) The 2 x 2 phase Fresnel Lens (PFL) array b) The 2 x 2 optical traps array generated from PFL array method[162]	67
Figure 5-2 Position array associated with each PCA of the array detector. Each coordinate represents a position of the Fresnel lens pattern in the SLM's referential (X pixel, Y pixel). The SLM is slightly tilted compared to the PCA array and therefore each channel or line is not perfectly horizontal in the SLM's referential.	68
Figure 5-3 a) Photographs of fabricated THz lenses (10x10 in ABS) [167] b) Fabricated array of silicon shallow lenses [171].	70

LIST OF SYMBOLS AND ABBREVIATIONS

This list presents the symbols and abbreviations used in the thesis or dissertation in alphabetical order, along with their meanings.

CW Continuous waveform

DAQ Data Acquisition Card

FFT Fast Fourier transform

FPS Frame per second

FWHM Full width at half maximum

fs Femtosecond

LCD Liquid-crystal display

LCOS Liquid Crystal on Silicon

NEP Noise-equivalent power

PCA Photoconductive antenna

PMT Photomultiplier tube

ps Picosecond

QCL Quantum cascade laser

SNR Signal-to-noise-ratio

THz Terahertz

CHAPTER 1 INTRODUCTION

In recent years, terahertz (1 THz = 10^{12} Hz) electromagnetic waves have emerged due to the growing number of their technological applications. The THz range is usually defined as going from 0.1 THz ($\lambda = 3$ mm) to 10 THz ($\lambda = 30\mu\text{m}$). This region of the electromagnetic spectrum situated between microwaves and infrared waves is known as the “THz gap”. This expression refers to the lack of efficient emitters and detectors compared to its neighboring spectral regions, as mature electronic and optical technologies can be used for microwaves and infrared waves, respectively. THz radiation has unique characteristics and is well suited for imaging applications since it can penetrate most dielectric materials, it is non-ionizing and it is absorbed by water molecules. THz waves are thus not harmful to biological material and find many practical applications in the biomedical field[1, 2] such as cancer detection and plant health monitoring for agriculture. Although microwaves can also penetrate materials like plastic and clothing, the shorter wavelength of THz waves provides better resolution and several security applications have been demonstrated[3, 4]. Furthermore, THz radiation is currently the highest frequency where electric field can be measured directly using nanoJoule-level femtosecond pulses. This means that not only the amplitude of the wavefront can be measured but also its shape (phase). Phase sensitive measurements open a large variety of applications in beam front detection for beam front correction and improvement of resolution and image quality

Another important research field is THz telecommunications since the next generation of network (6G) is set to have an operational frequency at low THz frequencies[5]. . Many applications in telecommunication would benefit from phase sensitive measurements where the detection of the source position and its properties could be acquired. This is, however, outside the scope of this thesis where the emphasis will be on imaging and sensing with THz radiation.

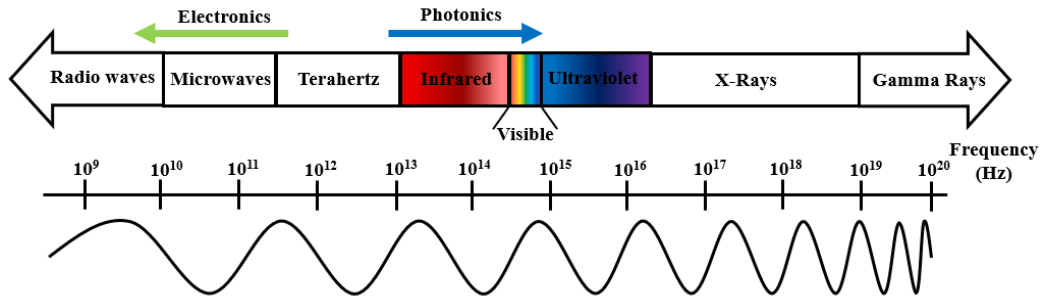


Figure 1-1 Terahertz gap in the electromagnetic spectrum

There are two main THz imaging system options: the THz time-domain system and the continuous waveform (CW) system. For the THz time-domain system, a broadband THz pulse is generated, and the frequency spectrum can be obtained via fast Fourier transform. As for the CW system, a narrowband signal is usually generated with photomixing techniques or with a quantum cascade laser (QCL). To obtain the complete THz frequency spectrum, the frequency is tuned sequentially. Each system has its advantages and disadvantages, and it is the technological needs that will dictate the choice of the system. The pulse system is usually more expensive and complex due to the necessity of a femtosecond ($1 \text{ fs} = 10^{-15} \text{ s}$) laser. This technique is well suited for spectroscopy and hyperspectral imaging since the whole spectral information is measured in a single scan. The resolution and the maximum frequency will depend on the length and the step size of the optical delay line. High peak power can be generated with repetition rates in the MHz order depending on the fs laser characteristics. One major application of the THz time-domain system is material characterization[6]. By measuring the time delay of the THz pulse with the sample and comparing it to a reference, important parameters such as refractive index and absorption coefficient can be easily obtained. On the other hand, the CW system offers better spectral resolution where the frequency is tuned with the accuracy of the order of 1 GHz. These systems are generally slower in this approach and can also be expensive when two lasers are necessary in a photomixing setup. The CW system tends to have a better signal-to-noise ratio (SNR) since the power is not spread over the whole frequency spectrum, compared to the pulse system. Moreover, in a single frequency imaging experiment, it's possible to optimize the detector and the optics accordingly to further increase the SNR. The frequency can also be chosen carefully to avoid the different absorption peaks caused by the presence of water molecules in the air.

In this thesis, the focus will be on the THz time-domain system due to its faster acquisition speed in hyperspectral and coherent imaging. We find many practical applications of the THz time-domain system in chemistry[7], pharmaceutical[8], biomedical[9, 10], food inspection[11] and much more. Two main factors limit the acquisition speed of a THz time-domain system. The first one is the presence of a slow mechanical optical delay line to scan the THz pulse. Some solutions have been proposed like asynchronous sampling where two fs lasers are used[12, 13]. However, this comes with a great financial cost considering the heavy price of fs lasers. Other cheaper solutions like fast rotary optical delay line[14] and oscillating optical delay lines[15] have been proposed to further increase the acquisition speed. The second factor is that most of the THz time-domain system are single pixel. Thereby, the detector or the object must be moved mechanically with precision to create an image (2D raster scan). The most common setup used photoconductive antennas (PCA) for both the detector and the emitter with different combinations possible in transmission or reflection[16]. An intuitive solution would be to simply take multiple PCA and use them as an array of pixels[17]. Some works have been done in this direction and up to 128 PCA have been placed in parallel to create a 1D detector of 128 channels[18]. Also, a recent work where a 63 channels 2D array of 9x7 pixels of nano-plasmonic antenna arrays has been proposed[19].

The main challenge to successfully use a PCA array detector is the optic to focus the fs probe beam on the gap of each antenna. Complex optics and alignments are needed, and this is the main reason why there's no multipixel PCA detector commercially available. In Ref. [19], they used a commercial diffuser to create multiple beams to address all the pixels of their detector simultaneously. However, this approach has the downside of distributing the optical probe power unevenly over the array. Indeed, the SNR and bandwidth were quite different between the central pixels (80 dB and 3 THz) and those on the periphery (60 dB and 2 THz). Another challenge is the read-out circuit for the different channels of the PCA array. In a single-pixel setup, a single-channel lock-in amplifier is used to increase the SNR. Commercial lock-in amplifier with a large number of channels are not yet available. In Ref. [19], they built a read-out circuit to sequentially address their pixel in combination with a single-channel lock-in amplifier. Therefore, they could only read the signal from one pixel at a time and thus limiting the acquisition speed of their system.

In this thesis, we propose an elegant solution combining an 8x8 PCA array and a spatial light modulator (SLM) to focus and steer the fs probe beam. We used a novel approach where 8 PCA

are combined to form one detection channel. Therefore, the detector had 8 detection channels instead of 64 as proposed in other similar studies. Furthermore, a multichannel virtual lock-in amplifier was implemented in *Labview*. This thesis is organized as follows. In Chapter 2, we present a complete literature review where the main physical concepts, mathematics and applications of THz time-domain systems are explained. A complete review of the available THz pulse detectors is elaborated to fully understand the objectives of this thesis. In Chapter 3, we explain the methodology behind this project. From a classic THz time-domain system to our final system, each modification is detailed with the motivations and objectives behind it. The main part of the thesis is then presented in Chapter 4 with our published paper in the *IEEE Access* Journal in the *photonic section* entitled: “Fabrication and Characterization of an 8 x 8 Terahertz Photoconductive Antenna Array for Spatially Resolved Time-Domain Spectroscopy and Imaging Applications”. In Chapter 5, a general discussion is finally proposed with future considerations and perspectives for the project.

CHAPTER 2 LITERATURE REVIEW

In this chapter, we first present the main concepts of a classic THz time-domain system. The goal is to give the reader a general understanding of how these systems work and to give an overview of its components. The theory behind the generation of THz pulses with a PCA is explained by the Drude-Lorentz model. One of the main elements of the THz time-domain system is the lock-in amplifier which greatly improves the SNR, and an entire subchapter is dedicated to its basic mathematics. In the next section, the main equations behind the extraction of the optical parameters such as the refractive index and the extinction coefficient of material are presented. Finally, a section is devoted to the technological applications of THz time-domain systems.

The second part of this chapter presents the different detectors found in the literature for THz pulse detection. We can divide THz pulse detectors into two large groups: “thermal” and “photon” detectors. The first one is based on the principle that energy in the form of heat is released when THz photons are absorbed by a medium. Among notable detectors using this mechanism, we find microbolometer arrays, pyroelectric detectors and Golay cells. For thermal detectors, only incoherent detection is possible and therefore only the amplitude of the signal is detected. As for the “photon” detectors, their name comes from the fact that the electric field of the terahertz photon will be measured and not its energy. For photon detectors, both coherent and incoherent detection are possible. A coherent detector is defined by its ability to measure both the phase and the amplitude of the signal. The choice between coherent and incoherent detection will be based on the application purposes. Phase information can be highly desirable in practical applications since it allows the measurement of dielectric constant/refractive index and sample geometry.. In the design of an imaging experiment, other criteria must be met such as sensitivity, spectral resolution, frame rate, frequency bandwidth, etc. and the choice of the detector will depend on it. Among photon detectors for THz pulse detection, we find photoconductive antennas, electro-optic detectors, air-biased coherent detection (ABCD), Schottky barrier photodiodes and field-effect transistors (FET). Each detector mentioned previously has its own section in this chapter where we present the physical mechanisms behind the detection, some examples of THz time-domain systems where they have been used and we finish by presenting cameras or arrays, if possible. It is also interesting to understand how photomixers detect THz radiation coherently in a CW system and a section is dedicated to it. In the final section of this chapter, a table summarizing all the

available detectors and their characteristics is proposed with a discussion on their advantages and disadvantages.

2.1 Terahertz time-Domain System

Terahertz time-domain system is a powerful tool where a coherent detection of the electric field of the THz light is possible. The THz time-domain system can measure a broadband THz pulse in a single acquisition scan. Via Fourier transform of the time-domain pulse, fast hyperspectral imaging is possible. A schematic diagram of a THz-TDs is shown in Figure 2-1. While there are many possible configurations of emitter/detector, we present the most common one and the one used in the context of this thesis. In this system, a photoconductive antenna-based on Lt-GaAs is used for both emitter and detector. The physical mechanisms behind the generation of THz pulses with a PCA are explained in the next section.

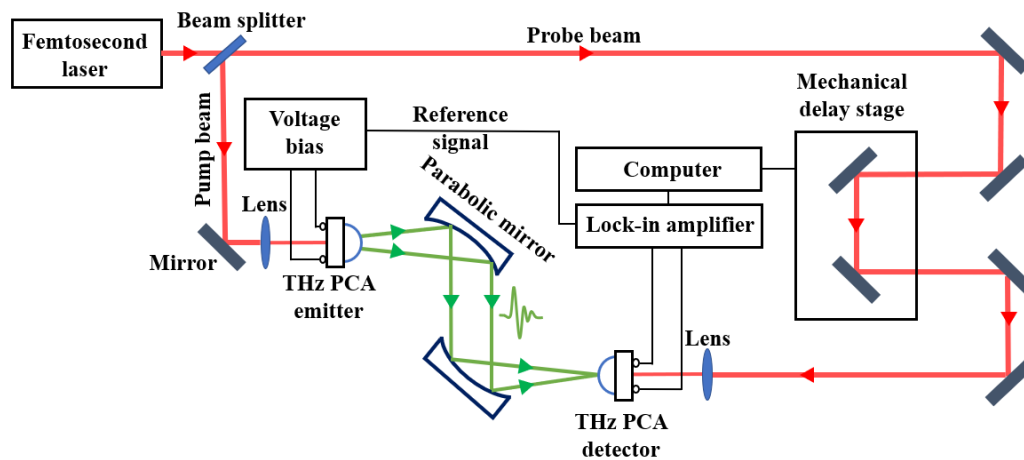


Figure 2-1 Schematic diagram of a typical configuration for a THz time-domain system

First, we have a femtosecond laser with pulse duration of approximately 100 fs, a repetition rate of around 100 MHz and a wavelength of 800 nm. The infrared (IR) fs beam is separated into a probe beam and a pump beam with a beam splitter. For the emission side, the pump beam is focused on the gap of the PCA, where a voltage bias is applied, and a THz pulse of a few picoseconds ($1 \text{ ps} = 10^{-12} \text{ s}$) is created. The emitted THz pulse is then collimated and focused on the PCA detector with a pair of parabolic mirrors. Furthermore, a silicon lens is positioned as close as possible of both emitting and detecting PCA to focus or collimate the THz pulse and to reduce back reflections.

On the detection side, the probe beam is also focused on the gap of the PCA detector while a mechanical delay stage is used to change the optical path length of the probe beam. By moving the delay stage, the THz pulse is scanned step by step. While Figure 2-1 is not to scale for ergonomic representation, the path length of the probe and the pump beam need to be balanced. Finally, a lock-in detection is done to achieve high SNR. The output signals of the lock-in amplifier can be read with a data acquisition card (DAQ) and a computer.

2.1.1 Photoconductive Antenna Emitter

The architecture of a PCA is simple. It consists of two metal plates on a semiconductor which acts as a photoconductive substrate. The two most commonly used semiconductors are gallium arsenide (GaAs) and indium gallium arsenide (InGaAs) [16]. The first one can be used at an optical excitation of around 800 nm and the other one at 1.55 μm . An example of a PCA architecture is shown in Figure 2-2. As for dimensions, the width of the gap can vary from a few micrometers (small gap PCA) to around 100 μm (large gap PCA). The thickness of the substrate will change depending on the semiconductor used. The substrate is then mounted on a printed circuit board (PCB) to allow an electrical connection to be made.

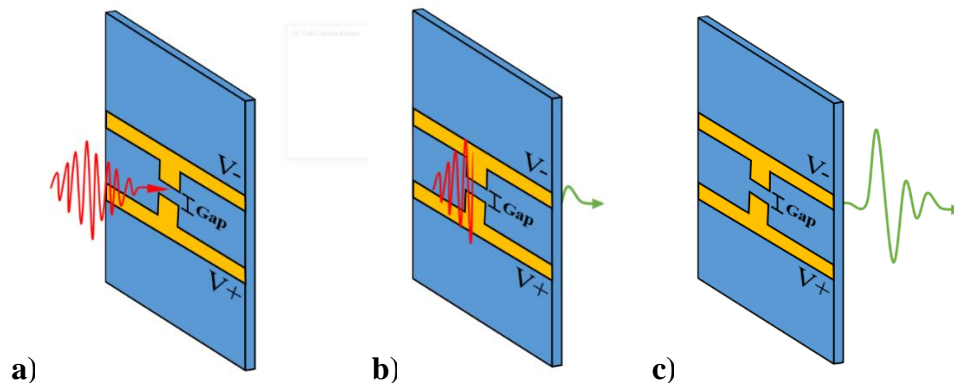


Figure 2-2 Generation of THz pulses with a photoconductive antenna **a)** The fs pulse is focused on the gap of the antenna where a voltage bias is applied **b)** Photocarriers are generated and accelerated by the voltage bias **c)** Emission of a THz pulse.

The generation of a THz pulse with a PCA starts with an incoming fs pulse focused on its gap. Since the substrate is photoconductive, photons with higher energy than the band gap will generate photocarriers in the gap of the antenna. By applying a voltage bias, an electric field is produced and will thus accelerate the electrons and the holes created towards the cathode and anode,

respectively. Thereby, a transient current is generated which drives the antenna and will therefore emit THz radiation[16] according to Maxwell's equations.

One of the most common models to explain the emission of THz radiation with PCA is the Drude-Lorentz model[20, 21]. It is a system of 3 differential equations based on the density of the carriers n , the velocity of the carriers v and the polarization P caused by the separation between the electrons and the holes. The first equation gives the rate at which the carriers are created. It depends on the carrier trapping time τ_c and the generation rate of the carriers $G(t)$ from the excitation of the fs laser. The generation rate of the carriers $G(t)$ can be approximated to a Gaussian function over time, where δt is the full width at half maximum (FWHM) of the fs pulse and n_0 the carrier generation density at $t = 0$ s[20].

$$\frac{dn}{dt} = \frac{-n}{\tau_c} + G(t) \quad (1)$$

$$G(t) = n_0 e^{-\left(\frac{t^2}{\delta t^2}\right)} \quad (2)$$

The third equation gives the acceleration of the carriers and depends on the scattering time τ_s , the local electric field produced in the gap E_{loc} , the elementary charge e and the effective mass m^* of the electrons.

$$\frac{dv}{dt} = \frac{-v}{\tau_s} + \frac{e}{m^*} E_{loc} \quad (3)$$

The local electric field E_{loc} will be smaller than the applied electric field E_{bias} due to a screening field represented by the third term in equation (4). This opposing field is simply caused by the presence of mobile charges and depends on a geometrical factor α and the dielectric constant of the photoconductive material ϵ .

$$E_{loc} = E_{bias} - \frac{P}{\alpha \epsilon} \quad (4)$$

The fifth equation gives the rate at which the polarization changes and depends on the recombination time between the electron and hole τ_r and the transient current created J .

$$\frac{dP}{dt} = \frac{-P}{\tau_r} + J \quad (5)$$

The transient current is given by the equation (6) and can be substituted into equation (5).

$$J = env \quad (6)$$

The solving of this system of ordinary differential equations will give the form of the transient current J . Based on Maxwell's equations, the time-dependent current will lead to the emission of an electromagnetic wave. Furthermore, it is more interesting to know the form of the electric field emitted since it is the information that will be measured by the detecting PCA. The electric field emitted E_{THz} will be proportional to the time derivative of the transient current J based on the Hertzian dipole theory[22].

$$E_{THz} \propto \frac{\partial J}{\partial t} \quad (7)$$

A simulation of the Drude-Lorentz model for THz generation with a PCA emitter was carried out to study the impact of the different parameters. The system of differential equations was solved in *Matlab* and most of the parameters presented in Table 1 comes from Ref. [20]. In Figure 2-3, we can see the impact of the FWHM size of the fs laser. For shorter pulse duration, higher frequencies are emitted which can be highly desirable in hyperspectral imaging since higher frequencies will provide better resolution. However, this comes with a significant financial cost since the price of fs laser increase for shorter pulses.

Table 1. Parameter values for the study presented in Figure 2-3

Parameter	Symbol	Value
Carrier trapping time	τ_c	0.1 ps
Carrier generation density at t = 0	n_0	10^{18} cm^{-3}
Scattering time	τ_s	30 fs
Relative electrons effective mass	m^*	0.0067
Applied electric field	E_{bias}	$20 * 10^5 \text{ V/cm}$
Geometrical factor	α	3
Dielectric constant of GaAs	ϵ	12.9 F/m
Recombination time	τ_r	10 ps

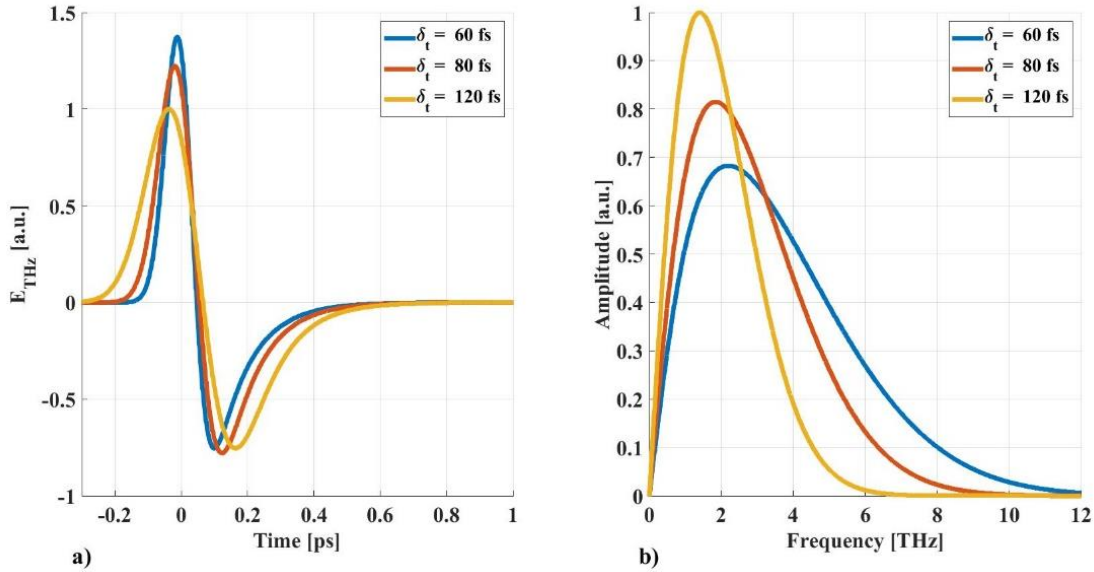


Figure 2-3 Drude-Lorentz model simulation with *Matlab* for THz generation with a PCA emitter based on Ref. [20] **a)** THz pulse emitted in the time-domain. **b)** Frequency spectrum of the signal depicted in panel (a).

2.1.2 Lock-in amplifiers

Lock-in amplifiers are used in multiple applications that require the extraction of a weak AC signal drowned in high noise. These amplifiers are commercially available and for the first part of this project where a standard THz time-domain was built, the *SR830* from *Stanford research*, a single-channel lock-in amplifier, was used. Since a multichannel lock-in amplifier is needed for the second part of the project, one was implemented by software with *Labview*. The purpose of this section is to set the main equations and to understand the main algorithms used in a lock-in amplifier.

2.1.2.1 Basic equations in lock-in amplification

Let us consider a modulated sinusoidal signal $E_{sig}(t)$ with an amplitude A_{sig} , a frequency ω_{sig} and a phase θ_{sig} buried in noise that need to be measured.

$$E_{sig}(t) = A_{sig} \sin(\omega_{ref}t + \theta_{sig}) \quad (8)$$

A reference signal $E_{ref}(t)$ is also needed with its own amplitude A_{ref} , frequency ω_{ref} and phase θ_{ref} .

$$E_{ref}(t) = A_{ref} \sin(\omega_{ref} t + \theta_{ref}) \quad (9)$$

The first operation that a lock-in amplifier does is multiplying the signal with the reference. One can prove with a simple trigonometric identity that the result of this multiplication $E_M(t)$ is given by equation (10).

$$E_M(t) = \frac{1}{2} A_{sig} A_{ref} [\cos((\omega_{sig} - \omega_{ref})t + \theta_{sig} - \theta_{ref}) - \cos((\omega_{sig} + \omega_{ref})t + \theta_{sig} + \theta_{ref})] \quad (10)$$

Since the signal $E_{sig}(t)$ is modulated at the same frequency then the reference, the equation (10) can be divided into an AC signal and a DC signal when $\omega_{sig} = \omega_{ref}$ and we obtain equation (11).

$$E_M(t) = \frac{1}{2} A_{sig} A_{ref} [\cos(\theta_{sig} - \theta_{ref})] - \frac{1}{2} A_{sig} A_{ref} [\cos(2\omega_{ref} t + \theta_{sig} + \theta_{ref})] \quad (11)$$

Therefore, by applying a low pass filter (LPF) on the mixed signal $E_M(t)$, only the DC component will remain and we obtain equation (12).

$$E_X(t) = R \cos \theta \quad (12)$$

The amplitude $R = \frac{1}{2} A_{sig} A_{ref}$ is proportional to the one of the signal by a factor of $\frac{1}{2} A_{ref}$. The relative phase difference between the signal and the reference can also be defined as one constant θ . As a matter of fact, the phase difference $\theta_{sig} - \theta_{ref}$ needs to remain constant over time. Otherwise, there would be no more DC component in equation (10). Lock-in amplifiers use what is called a phase-locked loop (PLL) algorithm to keep the phase difference between the signal and the reference constant. As for the noise, which is not modulated at frequency ω_{ref} , the vast majority will be in the AC component of equation (10) and will therefore be cut out by the low-pass filter. In the case of the noise at the modulation frequency, it will still be attenuated since the power spectral density of noise typically drops with the frequency.

The goal of all this process is to determine the value of R and θ . Another equation is then needed. It can be done by simply multiplying the signal $V_{sig}(t)$ by the same reference signal but with a phase shift of 90° via a second mixer. A schematic representation of a dual-phase lock-in amplifier is shown in Figure 2-4.

$$E_Y(t) = R \sin \theta \quad (13)$$

With equation (12) and (13) it is now possible to get the amplitude R and the phase difference θ .

$$R = \sqrt{E_X^2 + E_Y^2} \quad (14)$$

$$\theta = \text{atan} \frac{E_Y}{E_X} \quad (15)$$

The complex electric field is then given by equation (16)

$$E(t) = E_X(t) + iE_Y(t) \quad (16)$$

The spectral amplitude can finally be obtained via fast Fourier transform (FFT) with equation (17) and phase information with equation (18).

$$E(\omega) = \text{FFT}(E(t)) \quad (17)$$

$$\phi(\omega) = \arg(E(t)) \quad (18)$$

Most lock-in amplifiers have an auto-phase function to reduce the imaginary part of the THz pulse and therefore maximizing $E_X(t)$. In case we do not have this function, it is possible to maximize the real part of the signal when doing the data analysis. To do so, we simply need to multiply $E(t)$ from equation (16) by $e^{-i\varphi}$ where we need to find the angle φ that will minimize $E_Y(t)$.

$$E(t) = e^{-i\varphi}(E_X(t) + iE_Y(t)) \quad (19)$$

$$E(t) = (\cos \varphi - i \sin \varphi)(E_X(t) + iE_Y(t)) \quad (20)$$

$$E(t) = (E_X(t)\cos \varphi + E_Y(t)\sin \varphi) + i(E_Y(t)\cos \varphi - E_X(t)\sin \varphi) \quad (21)$$

We define the function Q representing the summation of the imaginary part's norm in equation (21) as:

$$Q = \sum_t |E_Y^t \cos \varphi - E_X^t \sin \varphi|^2 \quad (22)$$

$$Q = \sum_t (E_Y^t)^2 \cos^2 \varphi - 2E_Y^t E_X^t \sin \varphi \cos \varphi + (E_X^t)^2 \sin^2 \varphi \quad (23)$$

To determine the optimal angle φ , we simply derive equation (23) and find where $\frac{\delta Q}{\delta \varphi} = 0$.

$$0 = -2 \sin \varphi \cos \varphi \sum_t (E_Y^t)^2 - 2 \cos 2\varphi \sum_t E_Y^t \sum_t E_X^t + 2 \sin \varphi \cos \varphi \sum_t (E_X^t)^2 \quad (24)$$

$$0 = \sin 2\varphi \left(\sum_t (E_X^t)^2 - \sum_t (E_Y^t)^2 \right) - 2 \cos 2\varphi \sum_t E_Y^t \sum_t E_X^t \quad (25)$$

$$\tan 2\varphi = \frac{2 \sum_t E_Y^t \sum_t E_X^t}{\sum_t (E_X^t)^2 - \sum_t (E_Y^t)^2} \quad (26)$$

Finally, we obtain equation (26) and we find a value of φ and we use it in equation (19). To be sure that we really minimize the imaginary part and not maximize it, the second derivative of Q must be calculated and must respect: $\frac{\delta Q^2}{\delta \varphi^2} > 0$. While this method can help maximize the real part of the signal, it won't completely remove the imaginary part and therefore equation (16) still need to be used for the calculation of the FFT.

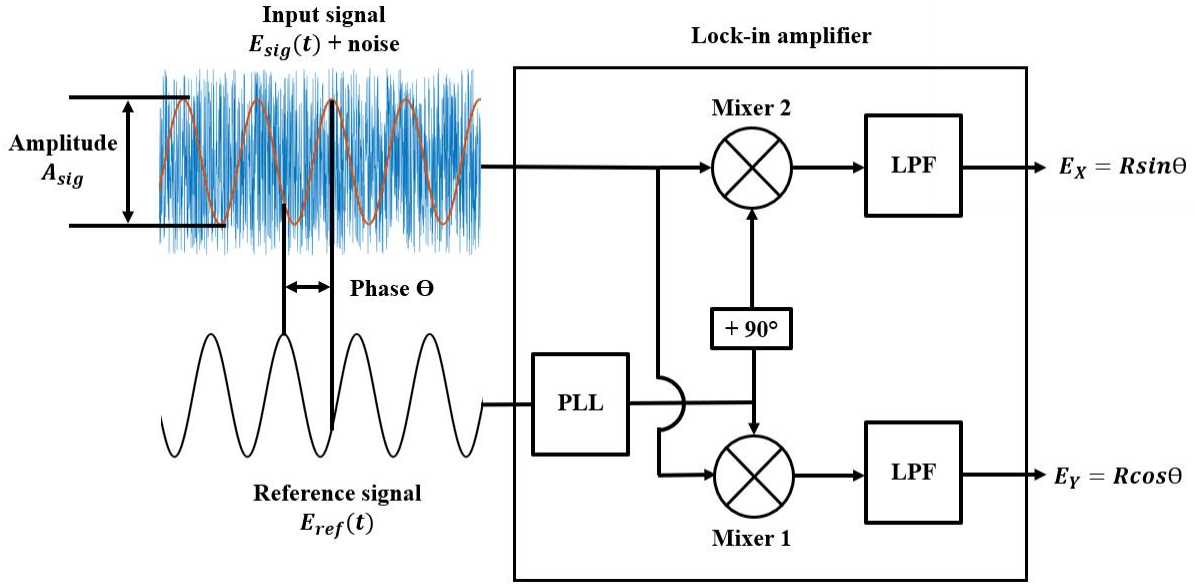


Figure 2-4 Schematic representation of a dual-phase lock-in amplifier. Phase-locked loop (PLL), Low pass filter (LPF)

2.1.3 Extraction of optical parameters with coherent detection

The fact that both phase and amplitude can be measured with coherent detection opens a lot of applications in material characterization via the measurement of optical parameters. A full description of how to extract the complex refractive index is presented for example in Refs. [23-27] and here we will present the main equations. One way to extract optical parameters in THz time-domain system is to compare two signals in the frequency domain: the reference signal $E_{ref}(\omega)$ and the sample signal $E_{samp}(\omega)$. The first one is simply the system without anything in the optical path of the THz pulse and the second one is the transmitted signal through an object. We defined the complex refractive index of the sample as $\hat{n}_{samp}(\omega) = n_{samp}(\omega) - i\kappa_{samp}(\omega)$ where $n_{samp}(\omega)$ is the real refractive index and $\kappa_{samp}(\omega)$ the extinction coefficient. We can define $E_{ref}(\omega)$ and $E_{samp}(\omega)$ with equation (27) and equation (28) where η is the transmission factor of free space [23], c the speed of light and $E_0(\omega)$ is the electric field of the incident wave. In this particular case, the sample is in the form of a plate with parallel sides with a thickness L

$$E_{ref}(\omega) = \eta e^{\left[-i\frac{\omega L}{c}\right]} E_0(\omega) \quad (27)$$

$$E_{samp}(\omega) = \eta \frac{4\hat{n}_{samp}(\omega)}{(\hat{n}_{samp}(\omega) + 1)^2} e^{[-i\hat{n}_{samp}(\omega)\frac{\omega L}{c}]} E_0(\omega) \quad (28)$$

We have the transfer function defined by equation (29).

$$H(\omega) = \frac{E_{samp}(\omega)}{E_{ref}(\omega)} \quad (29)$$

$$H(\omega) = \frac{4\hat{n}_{samp}(\omega)}{(\hat{n}_{samp}(\omega) + 1)^2} e^{[-i\frac{\omega L}{c}(\hat{n}_{samp}(\omega) + 1)]} \quad (30)$$

$$H(\omega) = \frac{4\hat{n}_{samp}(\omega)}{(\hat{n}_{samp}(\omega) + 1)^2} e^{[-i\frac{\omega L}{c}(n_{samp}(\omega) - 1)]} e^{[-\frac{\omega L}{c}\kappa_{samp}(\omega)]} \quad (31)$$

Based on equation (31) we can finally extract the refractive index and the extinction coefficient assuming $\kappa_{samp}(\omega) \ll n_{samp}(\omega)$.

$$n_{samp}(\omega) = 1 - \arg(H(\omega)) \frac{c}{\omega L} \quad (32)$$

$$\kappa_{samp}(\omega) = \frac{c}{\omega L} \ln \left[\frac{4n_{samp}(\omega)}{(n_{samp}(\omega) + 1)^2} - \ln|H(\omega)| \right] \quad (33)$$

Another simple way to calculate the refractive index of a material with a THz time-domain system is with the arriving times of the THz pulses to the detector. The time delay \mathbf{t}_d represents the time difference of the THz pulse between the sample and the reference. We can get the refractive index with equation (34). It is important to note that equation (34) is only valid for samples with relatively small chromatic dispersion, since we assume that the THz pulse shape is conserved or is slightly affected. It is important to mention that this time-domain method will give the group refractive index associated with the group velocity of the THz pulse.

$$n_{samp} = 1 + \frac{ct_d}{L} \quad (34)$$

This last equation is directly related to equation (32) and by using the phase difference $\Delta\phi(\omega) = \phi_{samp}(\omega) - \phi_{ref}(\omega)$, we have the frequency dependant refractive index of the sample given by equation (35).

$$n_{samp}(\omega) = 1 + \frac{c\Delta\phi(\omega)}{\omega L} \quad (35)$$

2.1.4 Imaging applications with a THz time-domain system

While really good reviews on THz imaging already exist in Refs. [28-32], this section gives a brief overview of the different imaging applications of THz time-domain systems. The first imagery experiment with a THz time-domain system was done in 1995 by B. B. Hu and M. C. Nuss in Ref. [33]. They used a similar system to the one presented in section 2.1 where they did a raster scan (they mechanically moved their sample in the focal plane) to create an image while using a single pixel PCA detector. In their first experiment, they were able to image a semiconductor integrated circuit through a plastic packaging. The THz radiation was absorbed by the presence of metal and the semiconductor, whereas little absorption was observed for the plastic. In their second experiment, they mapped the water distribution of a leaf over time. Their work paved the way for many technological applications and some interesting examples will be discussed.

In the biomedical field, THz time-domain systems are used in cancer detection[34-37], the studies of proteins, cells and tissues[1], burn depth diagnosis[38], bacteria detection[39], virus detection[40] and much more. Due to the low energy of THz photons and their non-ionizing nature, THz radiation is a good candidate for non-destructive imagery purposes. This means that no protective measures are necessary, which is not the case with X-ray devices, for example. In Ref. [35] they successfully distinguish cancer and non-cancer tissue in a reflective THz time-domain system and Figure 2-5 presents some of their results. They did their experiment on a paraffin section of the tissue ex-vivo. Most of the articles on cancer detection are done ex-vivo due to the considerable size of the THz time-domain systems. There is however in-vivo applications like in Ref. [41] where they determined the corneal tissue water content of rabbits.

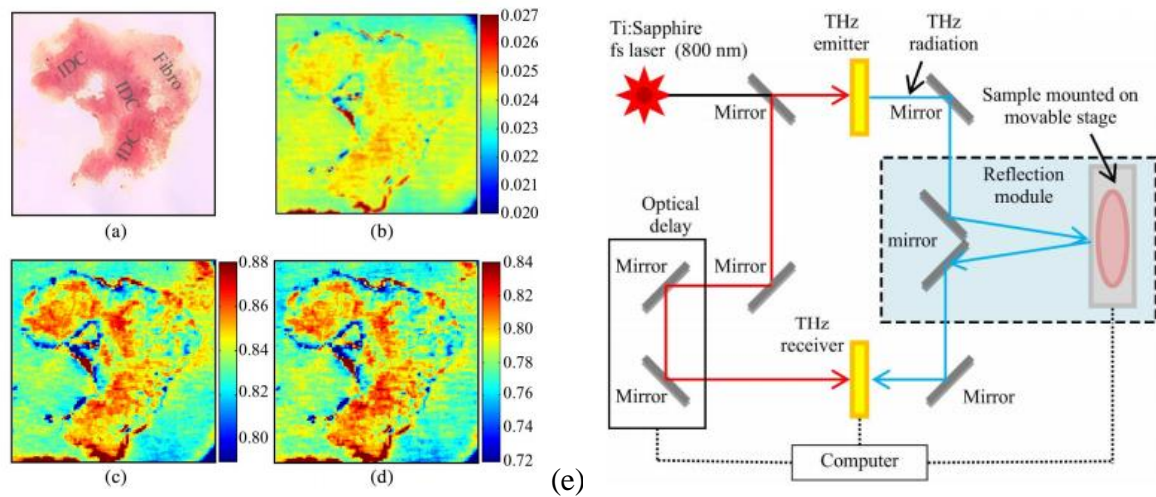


Figure 2-5. 46-year-old Caucasian woman diagnosed with infiltrating ductal carcinoma (IDC). **a)** Low-power pathology image used for correlation. **b)** THz time-domain image of the sample. **c)** Frequency-domain image at 1.5 THz. **d)** Frequency-domain image at 1.75 THz. **e)** Diagram of the pulsed THz system in the reflection imaging mode [35]

In the security domain, THz time-domain systems find many practical applications. As mentioned previously, THz radiation can penetrate most dielectric materials and can be used for security screening[4, 42, 43]. They have been used to detect drugs[44, 45], explosives[43, 46] and weapons [47]. In Ref. [48], they built a single pixel scanner for drugs and explosives detection in mail envelopes. They used fiber-couple PCA as emitter and detector, and they used a XY scanner to do a raster scan of the envelope. Each pixel is recording a full time-domain spectrum of 100 ps and by FFT the spectral information is available. Since a slow mechanical movement of the sample is necessary, it would be impossible to scan thousands of envelopes rapidly for a national post service for example. Their system is more suited for small offices and correctional facilities. They have built a system where a surface of $324 \times 229 \text{ mm}^2$ can be examined in a few minutes. Due to the raster scan, if they want to properly examine each corner of the sample, the scanning area needs to be at least four times larger than the sample itself. Their system is not compact and this main disadvantage limits its applications. This kind of system is the perfect example where an array of PCA would be of great benefit since the size of the raster scan could be partially reduced.

Finally, THz time-domain systems find many other practical applications in food quality and inspection[49], archaeology[50], material sciences[51-54], chemistry[7], etc. As a final example, in Ref. [55], they used a THz time-domain system to characterize the electrical properties such as

conductivity, scattering time, carrier density and mobility of graphene. The non-contact, relatively rapid and non-destructive nature of THz time-domain system make it an excellent choice for graphene characterization. For their experiment, they used a commercial THz time-domain system (Picometrix T-Ray 4000 [56]) where both emitter and detector are PCA[57]. They did a raster scan of the graphene sample to map the electrical properties mentioned above in order to optimize graphene growth.

2.2 Thermal Detectors

In this section, three types of thermal detectors for THz time-domain system are presented. The first one is the Golay cell which is the simplest one. The second one is the microbolometer arrays where uncooled cameras are available commercially. Finally, pyroelectric detectors are presented. One of the advantages of thermal detectors is that they respond to a broad spectral range. On the other hand, they are relatively slow because it takes a certain time between each measurement for the temperature to reach an equilibrium.

2.2.1 Golay Cells

The concept of Golay cell was first described by Marcel Golay in 1947. The detector is composed of a small gas chamber with a thin absorbing film to allow a heat transfer from the radiation to the gas. While radiation increase, temperature and pressure increase in the gas chamber and a membrane at one end of the chamber is pushed. An optical system is then used to precisely measure the movement of the membrane. Figure 2-6 (a) shows a typical Golay cell for THz detection. The main advantages of this kind of detector are that they can be operated at room temperature, they are low cost, they are broadband, and the design is simple. On the other hand, they are not precise, they are susceptible to thermal fluctuations of the environment, their frame rate is quite low since the temperature rise is not instantaneous and it is practically impossible to build an array of Golay cells.

In THz time-domain system, Golay cells are rarely used for actual measurement experiments. However, they can be useful in the system calibration process and to determine the THz power emitted. As can be seen in Figure 2-6 (b) from Ref. [58], they used a removable mirror to compare the total THz pulse energy measured with their designed electro-optic detector and a Golay cell

detector. In Ref. [59] they did something similar where they replaced their fiber-coupled PCA detector by a Golay cell detector to investigate the power of their PCA emitter.

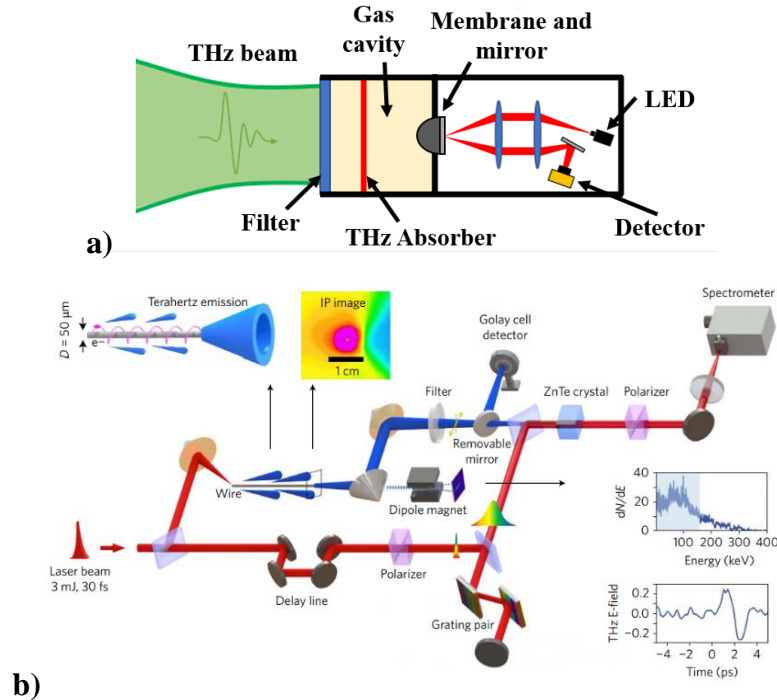


Figure 2-6 **a)** Principle of a gas Golay detector with the optical read-out system **b)** Schematic of a laser-driven wire-guided undulator for terahertz emission. The THz beam was collected by a pair of off-axis parabolas and focused onto a 1-mm-thick ZnTe crystal, or onto the Golay cell detector [58]

2.2.2 Microbolometer Arrays

Microbolometer are thermal-based detectors that will measure a change of electric resistance when heated or cooled. A schematic representation of such detector is presented in Figure 2-7 (a). The temperature of the microbolometer absorbance layer will increase due to the absorption of THz radiation. Based on the temperature coefficient of resistance, the resistance will increase or decrease with the temperature and can thus be measured and calibrated as a function of THz light intensity. Microbolometer detectors can be divided into two major categories: cooled and uncooled detectors. The cooled microbolometer detectors can be based on metal, composite, semiconductors and superconductor[60]. They have higher sensitivity and shorter integration times resulting in faster frame rates. They usually need a complex cooling system with liquid helium to operate at low Kelvin temperatures. This results in expensive systems with huge dimensions that are not yet

practical for commercial applications. On the other hand, uncooled microbolometer cameras are commercially available and are mostly based on technology developed for infrared detection. However, uncooled microbolometer arrays have significantly lower SNR due to thermal noise. In Figure 2-7 (b) we can see the MICROXCAM-384I-THZ TERAHERTZ CAMERA from the Institut National d'Optique (INO).

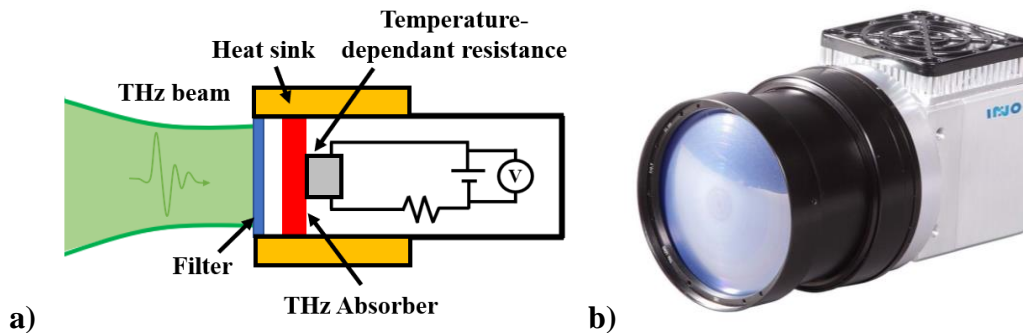


Figure 2-7 **a)** Schematic representation of THz bolometer detector **b)** Uncooled microbolometer camera MICROXCAM-384I-THZ from l'Institut National d'Optique (INO)[61]

These sensors find practical applications in CW systems where they can be used in security screening for example[61]. There are, however, a few recent works where they have been used in THz time-domain systems[62, 63]. One of the main challenges in THz time-domain system is the alignment of the THz beam due to the lack of highly sensitive detector arrays. For the system presented in section 2.1, the first step of the calibration is to simply try to detect a THz pulse. This is done by moving the PCA emitter, the PCA detector, the two Si lenses, the parabolic mirrors and the incoming IR fs optical beam. Each time a component is moved, the mechanical delay stage need to be moved to see if a THz pulse is detected. By doing multiple iterations, a THz pulse can be detected. The signal is then optimized by doing the same manipulations to maximize the amplitude of the THz pulse. This technique is time consuming and could be improved with a camera. Even if the detection would not be coherent, the microbolometer camera could make the first alignment step and give a good knowledge of the THz beam position. The main advantage would be the higher acquisition speed since the mechanical delay stage would not need to be moved and the fact that the camera would work at multiple frames per second (FPS). The camera could then be replaced by a coherent detector if the application requires it. In Ref. [64], they used a 320 x 240 (50 μm pixel pitch) array of highly sensitive antenna-coupled microbolometers with

integrated CMOS read-out electronics at 25 FPS to characterize a THz beam emitted by a PCA. They obtained a SNR of 10 in the time-domain and they were able to measure a THz beam of 25 nW. Similarly, a commercial camera is proposed by Ref. [65] and is compatible with THz pulse system with a noise-equivalent power (NEP) below $1.5 \text{ pW}/\sqrt{\text{Hz}}$.

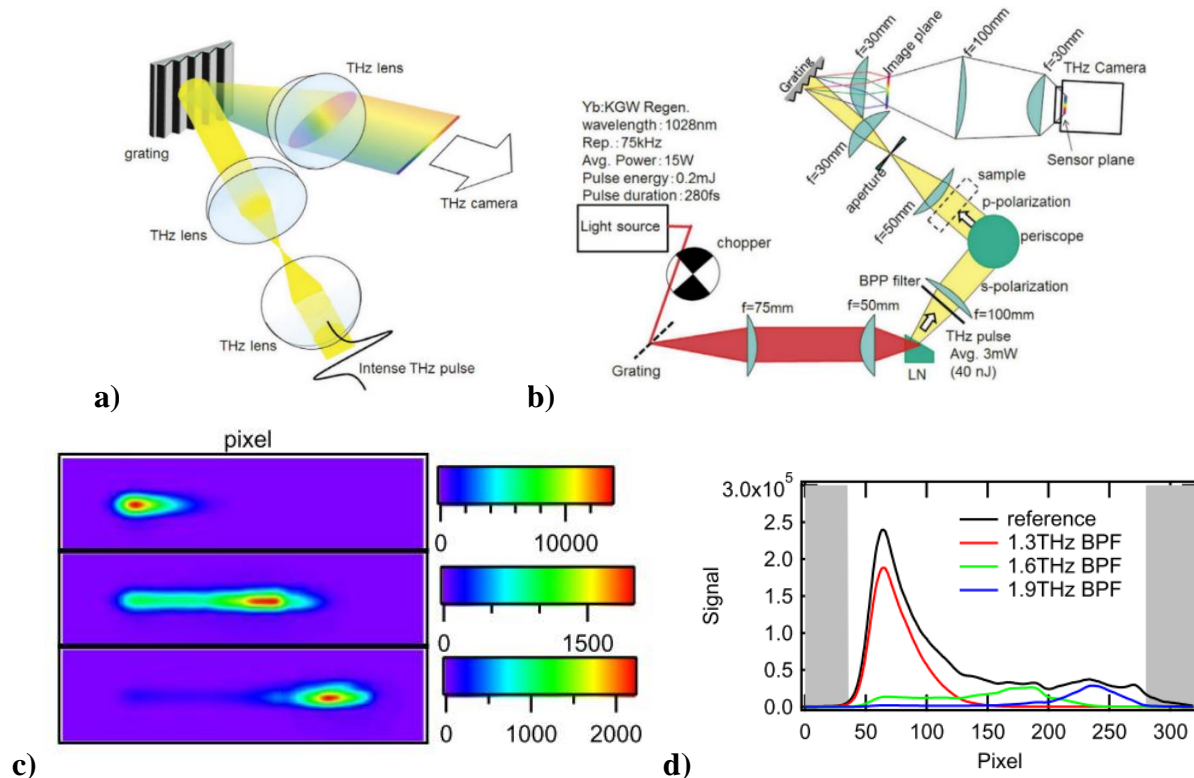


Figure 2-8 **a)** Schematic of the real-time multichannel spectrometer with diffraction grating. **b)** Setup for the experiment. A high-power THz pulse source and a high-sensitivity THz camera were used. **c)** Frequency-resolved profiles of the THz beams obtained using the THz camera with bandpass filters (BPF) whose center frequency were 1.3 THz (top), 1.6 THz (middle), and 1.9 THz (bottom). **d)** Horizontal profile of the camera images integrated in the vertical direction. [66]

While in Ref. [64] they measured all the frequencies of the THz pulse simultaneously, they couldn't differentiate them. In Ref. [66], they used a grating to spatially separate THz frequencies. Each frequency would therefore hit their camera at a specific location and a frequency spectrum was acquired. The microbolometer array camera they used is presented in Ref. [67] can detect signal as low as 100 pW at a frequency of 1 THz. In Figure 2-8 (a) and (b), we can see schematic

representations of their system. In Figure 2-8 (c) and (d), we can see the result of their experiment when bandpass filters are applied. We can clearly see that frequencies are being cut off.

2.2.3 Pyroelectric Detectors

The pyroelectric detectors are based on the principle that the spontaneous electric polarization of a pyroelectric material varies with a change in temperature. The pyroelectric crystals like triglycine sulfate (TGS), deuterated triglycine sulfate (DTGS), lithium tantalate (LiTaO₃), and barium titanate (BaTiO₃) are commonly used[68]. As can be seen in Figure 2-9, the pyroelectric crystal is in between two electrodes where the top electrode is designed to absorb THz radiation and heats the crystal. With an increase of temperature, the spontaneous electric polarization will change resulting in a detectable current I . This technology is commercially available, and it is possible to buy cameras like the one presented in Figure 2-9 (b). However, these cameras are mainly used in CW systems[69] due to their low sensitivity. In fact, no study was found where imagery was done with a THz time-domain system and a commercial pyroelectric camera.

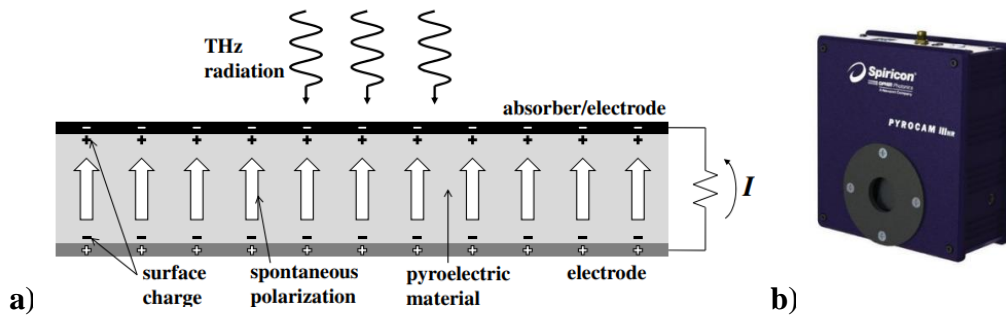


Figure 2-9 . a) Schematic diagram of a typical pyroelectric detector[68] b) Pyroelectric camera

PyrocamTM III Series[70]

Regarding the use of pyroelectric detectors for THz time-domain systems, their main utility is power measurement. In Ref. [71], they characterized the spectral response of a large-area pyroelectric detector. Within a certain uncertainty interval, they proved that the spectral response was flat from 300 GHz to 30 THz. They used three different emitters to cover the range mentioned previously. However, their detector had a noise equivalent power (NEP) of 200 nW/ $\sqrt{\text{Hz}}$ limiting its applications to specialized high-power emitters. They mentioned that they could further improve the NEP of their detector to use it in a conventional THz time-domain system as a power detector.

In Ref [72, 73], they proposed a novel ultrathin pyroelectric thin film (UPTF) detector that can precisely detect $1 \mu\text{W}$ of THz radiation with a spectrally flat responsivity from 100 GHz to 5 THz. In Refs [74, 75], while their works are focused on new ways of emitting THz pulses, they both used a calibrated broadband pyroelectric detector for energy measurements.

2.3 Photon Detectors

This section presents five photon detectors that can be used in THz time-domain system. In 1984, Auston and al. were the first to generate and detect THz pulses with PCA [76]. PCA detectors are nowadays commonly used in THz time-domain systems and since this thesis particularly focuses on PCA array detector, a complete review of what has been done in the literature so far is presented. Furthermore, sections on electro-optic detectors, air biased coherent detection (ABCD), Schottky barrier photodiode and Field effect transistors (FET) are presented.

2.3.1 Photoconductive Antennas

The principle of THz pulse detection with PCA is similar to the emission presented previously in section 2.1.1. The design for the PCA detector is identical as the one presented in Figure 2-2. The IR fs laser is also focused on the gap of the PCA to create photocarriers. The difference is that there is no bias voltage applied. It is the electric field of the incoming THz pulse that will accelerate the carriers to create a short photocurrent. The generated photocurrent is proportional to the THz field amplitude. A transimpedance amplifier is then used to convert this current into a measurable voltage.

There are few papers where solutions have been proposed to increase the sensitivity of PCA detector. In Ref. [77], they added an array of optical nanoantennas and a distributed Bragg reflector in order to form a hybrid cavity. This cavity would trap the optical pulse within the photoconductive layer and therefore increase the absorption of the IR photons. In Ref. [78], they integrated optical nanorods of ZnO in the gap of the PCA to further increase the generated photocurrent. Another promising way to improve detection is the incorporation of plasmonic antenna array in the gap of the PCA [79-82]. In Ref. [83] for example, they were able to increase the generated photocurrent by an incredible factor of 15400% with their nano-plasmonic antenna array compared to a classic PCA detector.

2.3.1.1 Array of Photoconductive Antennas

In order to understand the goal of this thesis, it is important to understand what has been done in the field of THz multipixel PCA detectors. This section is therefore a review of the main articles

where such devices have been developed. The goal is to explain the basic principles of the systems, their advantages and their disadvantages and to present the main results.

The first array of photoconductive antennas was presented in 2002 by Herrmann M. in *Towards multichannel time-domain terahertz imaging photoconductive antennas* [84] where they have developed a chip with 8 PCA. The focus of their article was more on the electrical circuit needed to operate their device, i.e., the read-out circuit they called Alternate Pulse locked Gated Integrator (APOGI) to replace a commercial multichannel lock-in amplifier which was expensive. They were able to measure a signal for each antenna but with considerable differences. The results are presented in Figure 2-10 b). This is because their optic alignment was far from optimal and the amount of light on each gap was not the same. Their photoconductive material was the LT-GaAs with a conductive material made of gold for the electrodes. The PCA's gap width was $5\ \mu\text{m}$ and each antenna was separated by $0.5\ \text{mm}$. They were able to successfully image a diagonally mounted wire with their multichannel detector and multichannel lock-in amplifier.

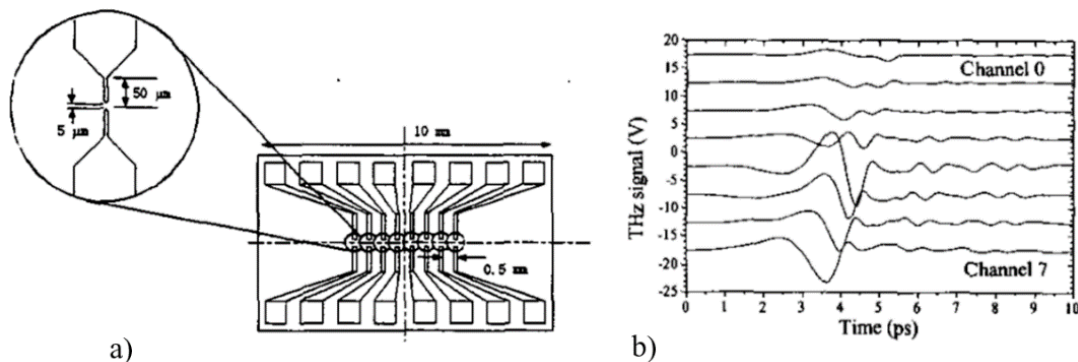


Figure 2-10 **a)** A linear array of 8 photoconductive antennas. **b)** THz waveforms measured simultaneously with an array of 8 photoconductive antennas and an array of 8 NOG1 amplifiers. (The offsets are arbitrary.) [84]

The second published research on an array of PCA was made by B. Pradarutti in 2008 and is entitled *Terahertz line detection by a microlens array coupled photoconductive antenna array* [18]. They also used LT-GaAs as the substrate, but they double the number of antennas to create a 1D array of 16 PCA (see Figure 2-11). The antennas also had a gap of $5\ \mu\text{m}$ and the distance between each of them was $500\ \mu\text{m}$. The focus of this article was more on the optical side with the goal to increase the efficiency of the detection. They used a focus laser line to excite all the antennas at the same time. By doing so, just a small amount of the laser power would be really used so they placed

an array of 16 micro-lens in front of their chip. The signal-to-noise ratio (SNR) was increased by a factor of 7 with the micro-lens array. They were able to do simultaneous measurement of THz signals with the 16 channels and the results are presented in Figure 2-11. The main advantage of using an array of micro-lens is the relatively easy alignment of the laser beam. It is also possible to add more antennas to create a larger array. Furthermore, A. Brahm and B. Pradarutti went in this direction and designed a 1D emitter/detector with 128 PCA in 2009 [85]. In 2012, they presented a 128 channels lock-in amplifier to use with their detector [86]

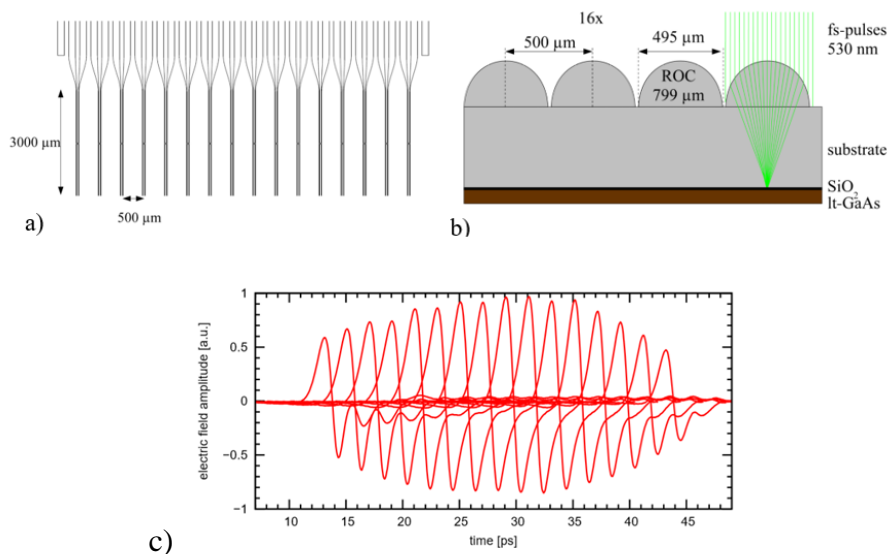


Figure 2-11 **a)** 16 channels photoconductive switch array **b)** Microlens array attached to the photoconductive switch array: schematic **c)** Simultaneous measurement of 16 ultrashort THz pulses (each pulse was shifted in time for 2 ps for a better overview) [18]

The third article discussed in this section was published by A. Brahm in 2014 and is entitled *Multichannel terahertz time-domain spectroscopy system at 1030 nm excitation wavelength* [17]. The main difference with the articles presented previously is the photoconductive material. In this research, they have developed an array of 15 PCA on a InGaAs/InAlAs multi-layer heterostructures (MLHS) substrate. They were thus the first ones to design a 1D array of PCA used at a wavelength of 1030 nm.

The fourth article analyzed in this section was published by Xurong and al. in 2020 and is entitled *A 63-Pixel Plasmonic Photoconductive Terahertz Focal-Plane Array*[19]. As mentioned previously, the incorporation of nano-plasmonic antenna arrays in the gap of the PCA increase the sensitivity of the detector. In their work, they built an array of 9x7 pixels of nanoplasmonic antenna

array. They achieved SNR > 60 dB and broadband detection > 2 THz. Each pixel covers $270 \times 240 \mu\text{m}^2$ and is made of 3 rows of 1500 nano-antennas. The total area of their detector is $2.43 \times 1.68 \text{ mm}^2$. As can be seen in Figure 2-12 (c), they used a diffuser and an objective lens to focus the 200 mW optical pump beam on the gap of each pixel. As mentioned previously, this technique had the major drawback of unevenly distribute the probe power over the detector. The center pixel had an SNR of 80 dB and a bandwidth of 3 THz whereas the pixel at the periphery had an SNR of 60 dB and a bandwidth of 2 THz. They also built a custom read-out circuit to sequentially record the signal of the 63 pixels of the detector in combination with a commercial single-channel lock-in amplifier. They could therefore only read one pixel at the time.

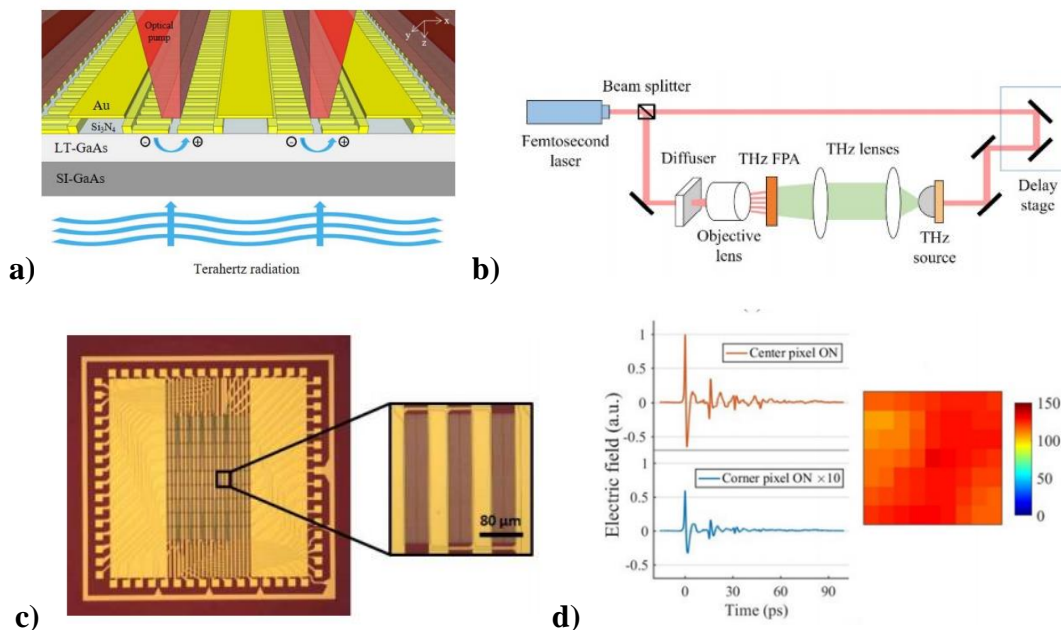


Figure 2-12 **a)** Schematic diagram of the plasmonic photoconductive terahertz FPA **b)** Block diagram of the time-domain spectroscopy setup used for characterizing the fabricated plasmonic photoconductive terahertz FPA **c)** Optical microscopy image of the fabricated 9×7 plasmonic photoconductive terahertz FPA. The magnified section shows one pixel **d)** The time-domain electric field detected by a center and corner pixel of the FPA. The color plot of the FPA output (the color of each pixel represents the peak photocurrent pulse level detected at each pixel after normalization).

2.3.2 Electro-Optic Detectors

Electro-optic (EO) detectors use the Pockels effect to directly measure the electric field of a broadband THz pulse [68]. The Pockels effect is the appearance of a birefringence in a nonlinear

crystal under the effect of an electric field. A birefringent medium is defined as being anisotropic and therefore the refractive index depends on the direction of the polarization of the light. In the case of THz EO detectors, the induced birefringence is proportional to the amplitude of the THz electric field. In Figure 2-13, we can see a schematic representation of these sensors to understand their principle. At first, let's consider the case where there is no THz radiation and only the linearly polarized optical probe beam. In that case, the polarization of the optical beam will not be changed by the presence of the EO crystal, and we will have a circular polarization at the exit of the quarter-wave plate (QWP). The circularly polarized optical probe beam will then go through a Wollaston prism that will basically split the light into two linearly polarized beams with orthogonal polarization. In the particular situation with no THz radiation, the orthogonal components will be equal. Now let's consider the case where the THz pulse induced a birefringence in the EO crystal. In this situation, the polarization of the optical probe beam will be slightly elliptical at the exit of the EO crystal. After passing through the QWP wave plate, the polarization of the optical pulse is almost circular but still elliptical. The balanced photodiodes will then measure a small difference between the two orthogonal polarizations that are no longer equal. The difference in the signals is directly related to the induced ellipticity of the optical pulse and therefore to the electric field of the THz pulse. A complete description of the mathematics behind this differential detection technique is described in Ref. [87].

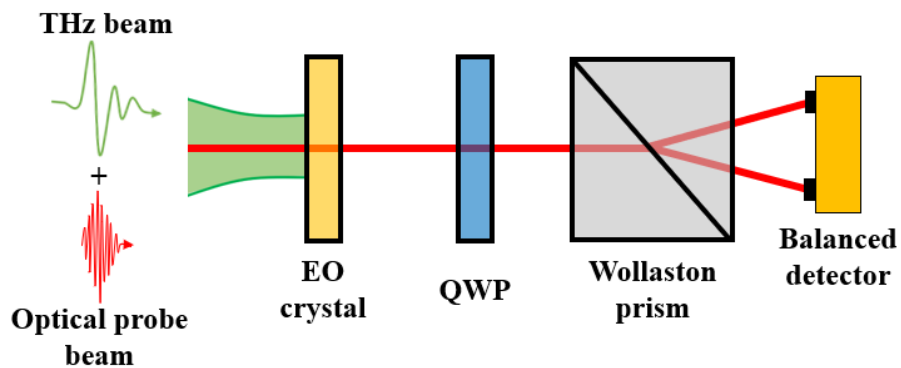


Figure 2-13 Schematic of EO detection method.

2.3.2.1 Arrays or cameras in electro-optic detection

In Ref. [88], they demonstrated coherent detection with an array of 8x1 balanced detectors. They used a laser line to probe the object and a multichannel lock-in amplifier was used to increase the

SNR. One of the main advantages of the electro-optic technique is the fact that it's the optical light that is measured by the detector. This means that conventional infrared/visible CCD/CMOS cameras can be used to measure the signal and real-time image can be acquired in two dimensions. The drawback of this situation is that a lock-in amplifier cannot be used and therefore resulting in relatively poor SNR. Furthermore, the THz beam needs to be spread all over the sample surface and thus reducing the illuminance and the SNR. In 1996, Wu and al. [89] demonstrated the two dimensions electro-optic (2D-EO) imaging for the first time with a thermoelectrically cooled CCD digital camera (576x384 pixels). At the time, they achieved SNR of 700 while the SNR of conventional balanced photodiodes with a lock in amplifier was higher than 20000. Since then, multiple articles were published with the aim of increasing the SNR. In Figure 2-14, a schematic representation of 2D-EO detection system with a camera is presented from Ref. [90]. Finally, in Ref. [91] they proposed a new interferometric technique called cross-polarized spectral-domain interferometry (CP-SDI) in combination with a CCD camera. Their technique had a dynamic range 4 times higher than a conventional electro-optic sampling setup.

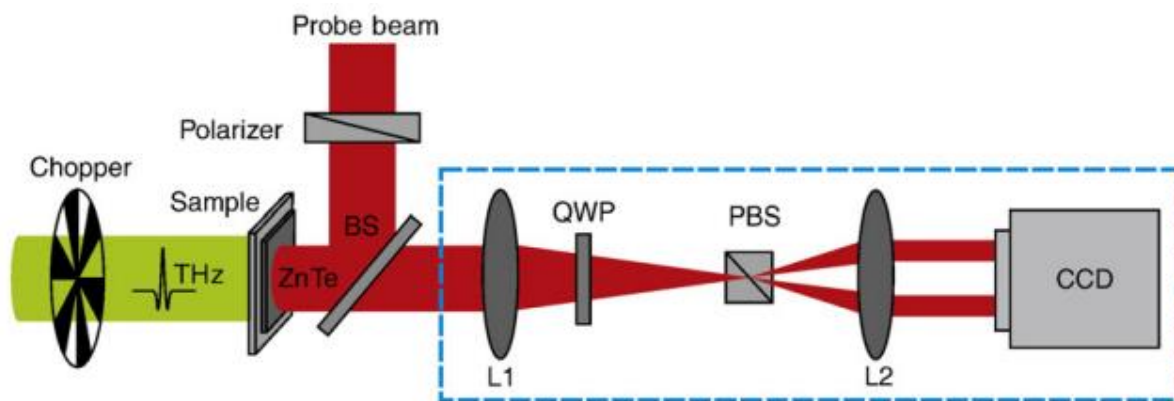


Figure 2-14 Schematic setup of the terahertz real-time imaging system with balanced electro-optic (EO) detection. Abbreviations : Beam splitter (BS), Quarter-wave plate(QWP), Polarized beam splitter(PBS), Lens (L1,L2) [90].

2.3.3 Air Biased Coherent Detection

The air biased coherent detection (ABCD) was first introduced in Ref. [92] by Karpowicz and al. They used the fact that a third order nonlinear process will happen when the THz pulse and the fs laser pulse ($\omega = 800$ nm) are tightly focused on a gas. A second harmonic (2ω) proportional to the electric field of the THz pulse will be emitted and can be detected with a photomultiplier tube

(PMT). This detection technique can cover a large part of the THz spectrum and will be limited only by the pulse duration of the fs. In Ref. [91], they were able to generate frequencies up to 200 THz with the two-color laser-induced air plasma technique which is simply the reverse mechanism of ABCD. They used a 10 fs laser pulse with its second harmonic to generate the THz pulse. In Ref. [93], they were able to detect up to 40 THz with ABCD and system similar to the one presented in Figure 2-15. There is no multipixel ABCD setup in the literature to this day and the technical challenges to achieve it are still considerable.

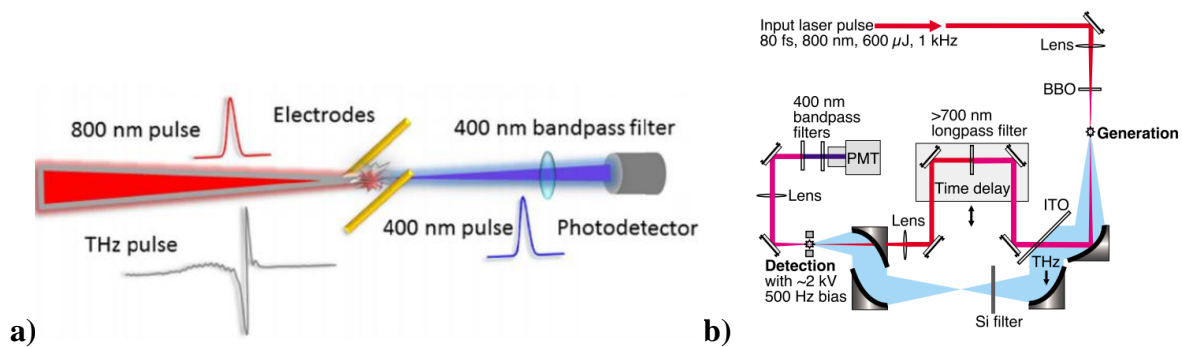


Figure 2-15 **a)** THz detection with air biased coherent detection (ABCD) method [93] **b)** Schematic diagram of the experimental setup. A laser pulse from a Ti:sapphire regenerative amplifier is focused through a BBO crystal to generate its second harmonic, and generates a terahertz wave at the ionizing plasma spot. The terahertz and optical beams are separated by a sheet of ITO-coated glass, and recombined in the detection region after the optical beam is filtered and variably delayed. A 500 Hz electric field is applied to the generation region, supplying a second harmonic local oscillator for coherent detection via a photomultiplier tube [92]

2.3.4 Schottky Barrier Photodiodes

Schottky barrier photodiodes are mostly used in CW systems and telecommunications systems[94]. They have also been used as a detector in THz time-domain systems in Refs. [95, 96] and a commercial option is proposed by *Toptica Photonics* [97]. In the context of THz pulses detection, Schottky barrier photodiodes act as an incoherent detector and phase information is thus lost. Schottky barrier photodiodes are formed by a heterojunction between a metal and an n -type semiconductor. When a photon goes through the semitransparent metal and is absorbed in the depletion region of the n -type semiconductor, a pair of electron-hole is created. A photocurrent is then generated due to the movement of the charge carriers under the influence of a built-in electric field. A simple schematic representation of such diode is presented in Figure 2-16. The main

advantage of the Schottky barrier photodiode compared to $p-n$ or $p-i-n$ photodiodes is their rapid time response in the picosecond regime making them an interesting choice for ultrafast resolution.

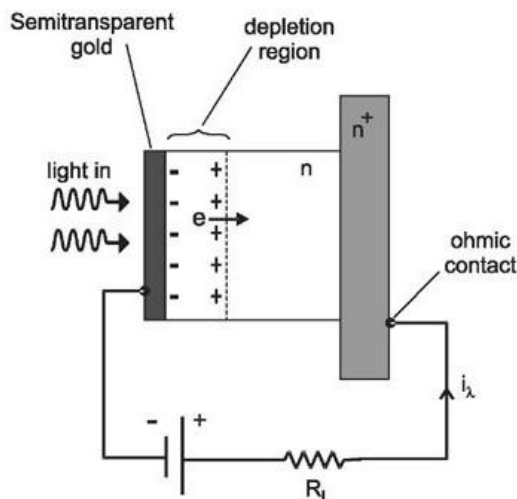


Figure 2-16 In a Schottky photodiode, light is absorbed in the depletion region of an n-type semiconductor after passing through a semitransparent metallic film [98].

In Refs. [95, 99], they present a system resolving THz pulse at 80 MHz repetition rate using a zero-bias Schottky diode as a detector (see Figure 2-17). The acquisition speed of their system was not limited by the detector but by the repetition rate of the femtosecond laser. They achieved it by building a system that does not require an optical delay line, a lock-in amplification or an averaging of the signal. This is mostly due to their high-power THz (25 μW) source and the high sensitivity of the Schottky photodiode. They achieved a diode sensitivity of 10^3 V/W and an NEP of $5 \times 10^{-10} \text{ W}/\sqrt{\text{Hz}}$. The main application of such system is in the biomedical field where protein dynamics occur in the microsecond's regime. They claim to have achieved acquisition speed 10,000 to 10,000,000 times faster than a conventional THz time-domain system.

In Refs. [96, 100], they present an array of 1×20 InGaAs Schottky barrier diode for THz imagery. In their papers, however, they did imagery on a knife with only a single-channel Schottky barrier diode, and they do not present imagery results with the whole array. They only present imagery results with the whole array in a CW setup. Finally, in Ref. [101] they present a Schottky contact LED for THz pulse detection. The structure of their detector is, however, different from a classic Schottky barrier diode. They also proposed a THz-LED camera prototype.

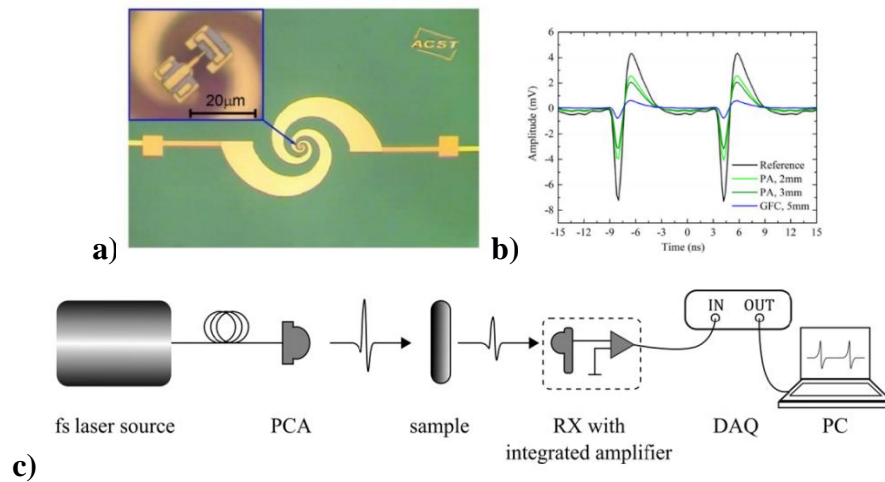


Figure 2-17 **a)** Log-spiral antenna and zero-bias InGaAs Schottky diode form an ultrawideband detector.[99] **b)** Terahertz field intensities measured at 80 MHz pulse rate. Shown is a reference trace and pulses transmitted through three different samples (PA polyamide, GFC glass fiber composite) [95] **c)** Schematic of the measurement setup. RX broadband receiver (Schottky diode model 3DL 12C LS2500, ACST GmbH) [95]

2.3.5 Field Effect Transistor (FET) Detectors

The principle and the basic mathematics of THz detection with a plasma wave field-effect transistor (FET) are well described in Refs. [28, 102]. In short, a DC bias voltage is applied between the gate and the source, and the incoming THz radiation will induce an alternate voltage by optical rectification. This voltage will be proportional to the power of the THz radiation. The main advantage of the FET detector is that Complementary metal–oxide–semiconductor (CMOS) technique can be used to build arrays and cameras[103]. These cameras are commonly used in the CW system for imagery purposes.

For THz time-domain system, however, there are only a few examples where FET detector has been used. In Ref. [104], they present a plasma wave GaAs nanometer FET detector at room temperature to detect terahertz pulses. In Ref. [105], they present a similar detector where they did imagery (2D raster scan) of a metallic paper clip at 1 THz. They used 1 THz since it was the frequency with the highest power in the THz pulse. Finally, in Ref. [106] they built a broadband bow-tie antenna-coupled THz detector based on a CMOS FET (TeraFET) for an autocorrelation experiment. They achieved an optical voltage responsivity of 100 V/W and NEP of 67 pW/ $\sqrt{\text{Hz}}$ at 0.6 THz.

2.3.6 Photomixers

While photomixers are only used in CW systems, it is still interesting to understand how they work since they can coherently detect THz radiation. Coherent generation and detection of THz radiation with photomixers was first demonstrated by a research group at MIT in 1998[107]. A schematic representation of a CW system is presented in Figure 2-18 where photomixer antennas are used for both emitter and detector. In this system, two CW lasers are used where their frequencies are slightly different. A beat frequency equal to the frequency difference of the two lasers is created using a 3dB fiber coupler. This frequency beat is then focused on the gap of the photomixer antenna where photocarriers are generated. The voltage bias will then accelerate the photocarriers to create a photocurrent and THz radiation is emitted. The mathematics behind the generation and detection of THz radiation with a photomixer antenna are well described in Ref. [108]. On the detection, the photocarriers will be accelerated by the electric field of the THz radiation and the photocurrent will be measured with a lock-in amplifier. One way to do spectroscopy with a system like this is to use tunable lasers to change the frequency difference and therefore sweep the THz frequency domain. Distributed feedback lasers can be used where the current and the temperature of the laser are modified to change the emitted wavelength. These systems are widely used in imaging experiments and can also be used in telecommunications with a few additional components to the system. They can generate strong THz signal with good SNR. Their major drawback is their expensive nature where the use of two tunable lasers comes with considerable costs.

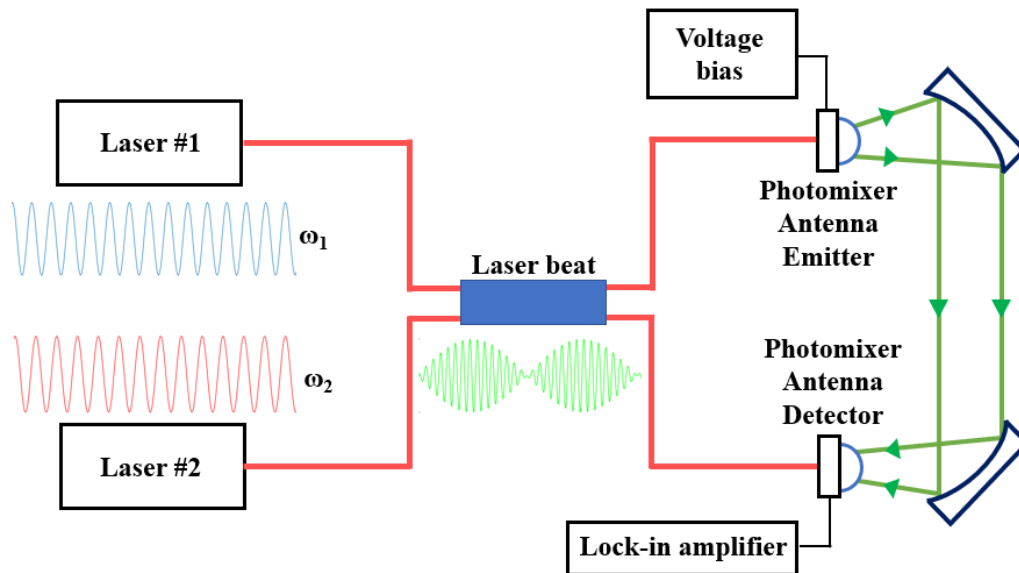


Figure 2-18 Schematic representation of a CW system with photomixer antennas for both emitter and detector

2.4 Summary

First, we can divide the detectors in two major categories: coherent and incoherent detectors. As mentioned previously, thermal detectors are incoherent detectors. They are mainly used for power measurement and alignment purposes. For photon detectors, no proof of coherent detection was found in the literature of the Schottky barrier diode and the FET detectors in THz time-domain systems. This does not mean that coherent detection is not possible, however. Furthermore, no camera based on these technologies are available commercially for pulse detection due to the low sensitivity. This means that for a particular application where phase information is desirable, only three detectors are available to this day: PCA, EO sampling and ABCD. While multipixel imaging was proved for PCA and EO sampling, the ABCD is still a single pixel technique and a 2D raster scan is necessary for imagery. For the PCA, arrays of 128 pixels (1x128) and 63 pixels (9x7) have been proposed in the literature. Each pixel corresponding to a single channel and therefore a lock-in amplifier channel is needed for each pixel. For the EO sampling, coherent detection has been done with an array of 8 pixels (1x8 PMT) and a multichannel lock-in amplifier. While CCD

cameras have been used to increase the number of pixels, the fact that a lock-in amplifier cannot be used decrease the SNR and limits this method to specific applications.

The main advantage of EO sampling over PCA is its wide broadband detection and the fact that it is the optical light that is detected. However, smaller SNR are observed for similar probe power. While considering the advantages and the drawbacks of each detector presented, we think a 2D array of PCA would be of great benefit for hyperspectral imaging. In Table 2, we present the important parameters such as SNR, NEP, FPS, array size, etc. from the articles discussed previously when the parameters are available.

Table 2 : Detectors for THz time-domain systems. (Coherent detection, Lock-in amplification, Frame per second (FPS), Signal to noise ratio (SNR), Noise equivalent power (NEP))

Detector type	Coherent	Lock-in	FPS (Hz)	SNR (dB)	NEP (pW/vHz)	Sensitivity (V/W)	Bandwidth (THz)	Array size	Pixel Pitch (μm)	Reference	Year
Thermal											
Golay cell											
	No	No	100	-	-	-	-	1	-	[109]	2012
Microbolometer											
	No	No	25	10	-	0.28nW/pix	0.1-2	320x240	50	[64]	2013
	No	Yes	15	-	-	-	0.5-2	320x240	23.5	[66]	2017
	No	No	9	-	1.5	-	0.1-18	160x120	25	[62]	2021
	No	No									
Pyroelectric											
	No	No	-	-	-	-	0.3-21	1x1	-	[75]	2012
	No	No	-	-	2×10^5	-	0.3-30	1x1	-	[71]	2015
	No	No	100	-	-	7nJ/pix	0.1-282	160x160	80	[70]	2021
Photon											
Photoconductive antenna											
	-	Yes	-	-	-	-	-	1 x 8	500	[84, 110]	2002
	Yes	Yes	-	-	-	-	-	1 x 16	500	[18]	2008
	Yes	Yes	-	-	-	-	-	1 x 128	500	[85, 86]	2009
	-	Yes	-	35	-	-	0.1-0.8	1 x 15	1000	[111]	2014
	-	Yes	-	>60	-	-	>2	9 x 7	270x240	[19]	2020
Electro-optic sampling											
	Yes	No	-	-	-	-	>100	1x1	-	[91]	2012
	Yes	Yes	-	-	-	-	-	1x8	500x1000	[88]	2007
	No	No	7.5	28.45	-	-	-	576x384	22	[89]	1996
	No	No	2	-	-	-	-	1030x1300	-	[90]	2010
ABCD											
	Yes	Yes	-	-	-	-	0.3-10	1x1	-	[92]	2008
	Yes	Yes	-	15.68	-	-	>40	1x1	-	[93]	2016
	Yes	Yes	-	30	-	-	0.5-35	1x1	-	[112]	2010
Schottky barrier diode											
	No	No	80×10^6	-	500	120-200	0.1-2	1x1	-	[95, 99]	2015
	No	Yes	-	-	106.6	98.5	0.1-3	1x1	500	[96]	2013
	No	No	-	-	-	-	0.05-1.5	1x1	-	[97]	2021
FET											
	-	Yes	-	-	-	-	0.1-3	1x1	-	[105]	2005
	-	Yes	-	15	67	100	-	1x1	1	[106]	2018

CHAPTER 3 METHODOLOGY

This section presents the main modifications and steps that the THz time-domain system went through to successfully detect THz pulses with the PCA array. At first a classic THz time-domain system was built to characterize each of its component. A virtual lock-in amplifier was then implemented and the designed PCA array was integrated in place of the commercial single PCA detector. Finally, the SLM was used to address each pixel of the PCA array individually.

3.1 Building a Classic THz time-Domain System

The first step of the project was to build a functional THz time-domain system like the one presented in Figure 2-1. TERA8-1 Photoconductive antennas from *Menlo Systems* were used for both emitter and detector. They are low temperature (LT) gallium arsenide (LT-GaAs) PCA with a thickness of 350 μ m and gap length of 5 μ m as can be seen in Figure 3-1. We used a 2D micrometric optomechanical mount (T8-H2) to hold and precisely align the PCA. A third micrometric screw is also used to align the focusing lens (A375TM-B $f = 7.5$ mm) to focus the IR beam on the gap of the PCA. A hemispherical silicon lens is finally placed as close as possible of the PCA to focus or collimate the THz beam. The silicon lens is positioned this way to avoid back reflections. To maximize the emission power, the PCA should be driven to a maximum voltage of ± 35 V. This is impossible with a commercial function generator which generally only reaches ± 10 V. An ultra-low noise high-voltage amplifier from *Falco Systems* (WMA-200) was therefore used to amplify the exit signal of the function generator. Finally, a commercial lock-in amplifier SR830 from *Stanford Research Systems* was used in this part of the project. A *Labview* program was built to control the mechanical delay stage and the data acquisition from the lock-in amplifier. The main components of the THz time-domain system are presented in Table 3.

Table 3 : Main components of the THz time-domain system built

Components	Model
Emitter and detector	TERA8-1 from <i>Menlo Systems</i>
Lock-in amplifier	SR830 from <i>Stanford Research Systems</i>
Laser	C-fiber 780 from <i>Menlo Systems</i>
Function generator	GFG-8216A from <i>GWINSTEK</i>
Ultra-low noise voltage amplifier	WMA-200 from <i>Falco Systems</i>
Mechanical delay stage	100 mm DDS100 from <i>Thorlabs</i>
Parabolic mirrors	RFL=4" MPD249-M01 from <i>Thorlabs</i>

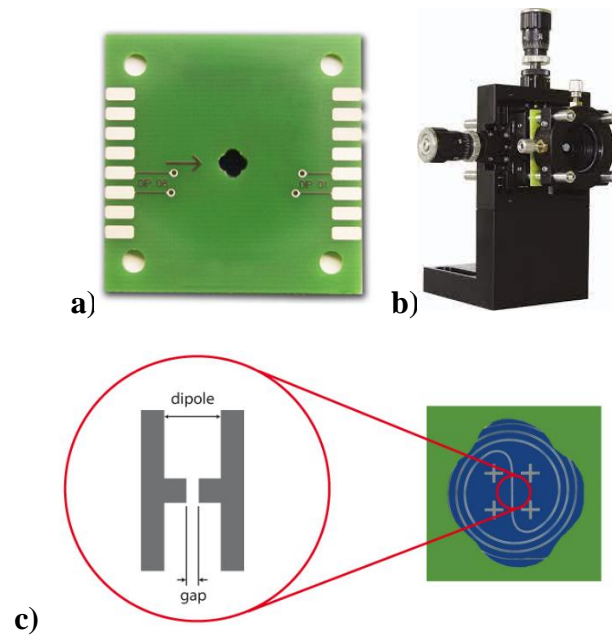


Figure 3-1 **a)** TERA8-1 PCA from Menlo System mounted on a PCB board **b)** Optomechanical mount T8-H2 from Thorlab **c)** Schematic representation of the gap of the PCA and a close look at the chip [113]

3.2 Implementing a virtual lock-in amplifier

The second step of the project was to implement a virtual lock-in amplifier in *Labview* and compare its performance with the *SR830*. Its operating principle is the same as for a traditional dual-phase lock-in amplifier such as the one presented in section 2.1.2 and Figure 2-4. Already built-in PLL, low-pass filter and demodulation algorithms were used to program it. The performances of this virtual lock-in were similar to the *SR830* when used in the system presented previously. However, to achieve similar SNR, higher integration times were necessary. All the different parameters were optimized experimentally such as the sample rate, number of samples, time constant, low pass-filter type and order. The sample rate and sample number were much higher than the bottom limit imposed by the Nyquist theorem. The best low-pass filter for the virtual lock-in was an infinite impulse response (IIR) type with a roll-off rate of 40 dB and order 1. The main limitation of the built virtual lock-in amplifier was the high integration time. A discussion on this topic can be found in the final chapter of this thesis.

The main reason why a commercial lock-in was not used with our PCA array is that 8 channels of detection are needed, and no commercial device offered such a number of channels. In our final setup, each channel of the PCA array is first connected via BNC cable to a transimpedance amplifier from *Femto*. We used two types of transimpedance amplifiers because we didn't know what would be the optimal gain for the system. At first, the DLPCA-200 with an adjustable gain from 10^3 to 10^{11} V/A allowed us to determine that 10^8 V/A was the optimal gain. We used four of these transimpedance amplifiers and then four LCA-40K-100M with fixed gain of 10^8 V/A. These devices are ultra-low noise with 19 fA/ $\sqrt{\text{Hz}}$ of equivalent input noise current. At the exit of the transimpedance amplifiers, the signal is then forward via BNC cable to a BNC-2110 and read by a data acquisition card (DAQ) from *National Instruments*. The BNC-2110 is simply a connection block with eight differential analog input signals. The signals are then forward to the actual DAQ. We used the PCIe-6376 as a first DAQ which has 8 analog inputs at 16 bits and 3.5 MS/s/ch. The reference signal and therefore the TTL output of the function generator was measured with a second BNC-2110 and a PCI-6132. This DAQ has 4 analog inputs at 14 bits and 2.5 MS/s/ch. In order to use the two DAQ simultaneously, their clock was synchronized with an RTSI cable from *National Instruments*. This means that we have a total of 12 detection channels at a maximum rate determined by the slowest of the two DAQ, which means 2.5 MS/s/ch. A schematic representation of the final setup is presented in Figure 3-2.

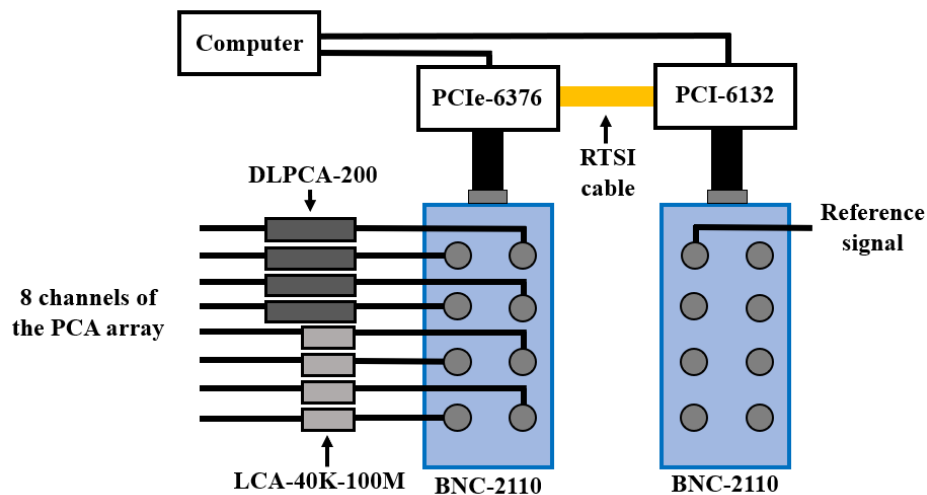


Figure 3-2 Schematic representation of the acquisition system

3.3 Integrating the PCA array

The third step was to actually use the designed PCA array in the THz time-domain system. The PCA from *Menlo Systems* was replaced by the PCA array which was mounted on a motorized 3D stage. To form the 3D stage, three MTS50-Z8 from *Thorlabs* were used. A schematic representation of the mentioned system is presented in Figure 3-3. While an SLM is used in future steps to focus the IR probe beam on the gaps of the PCA array, we didn't know at that time if this technique would work and if the power would be distributed equally over the whole chip. The main objectives of the current step were to first determine if a THz pulse could be detected with our PCA array and secondly to characterize the different channels of the PCA array under the same IR probe beam condition. To achieve this, the same focusing lens (A375TM-B $f = 7.5$ mm) that was previously used was mounted on a 3D printed holder in front of the detector. The PCA array was moved in 3 dimensions to find the different channels of the detector and THz signal were acquired for each antenna of the array.

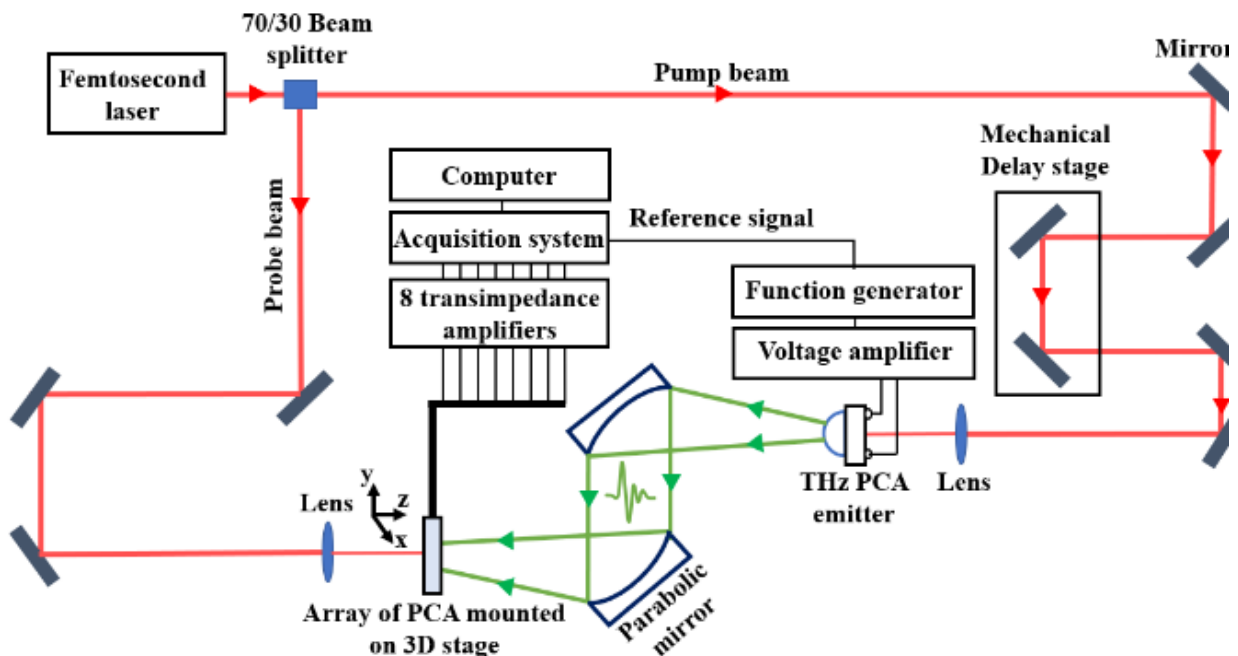


Figure 3-3 Schematic representation of the THz time-domain system with the PCA array mounted on a motorized 3D stage

We determined that all 8 channels of the detector were working correctly, and that each antenna had similar response to the IR probe beam. This response was based on the measured THz signal

at each pixel. The calibration process to find the exact position where THz signal is maximal for each pixel of the detector is well described in our paper presented in Section 4.7.

Finally, the detector was moved to the position (X, Y, Z) where the THz signal is maximal in the center of the chip (Line 4, col 4). This step is crucial in order to ensure that the THz beam is focused on the center of the detector and that it will be possible to detect a signal for all the pixels when the SLM is integrated in the next step.

3.4 Spatial Light Modulator Integration

A spatial light modulator (SLM) is a device that can modulate the amplitude, the phase and the polarization of light in space and time. The best-known example is the liquid-crystal display (LCD) projector commonly used to project images on a screen. In this project, the SLM is used to steer and focus the IR probe beam on the gap of each PCA of the array. The *PLUTO-2* from *Holoeye*[114] was used in this project. First of all, the *PLUTO-2* is a phase only Liquid Crystal on Silicon (LCOS) SLM used in reflection. It has a resolution of 1920x1080 pixels with $8 \times 8 \mu\text{m}^2$ pixel size. LCOS-SLM work on the principle that the birefringence of the liquid crystal can be changed with an electric field. The liquid crystal rotate proportionally to the electric field and the refractive index will change at the pixel location. This means that different phase retardation can be achieved at each pixel and the shape of the reflected wavefront can be controlled. The phase retardation of the incoming wavefront at each pixel is controlled with a grayscale. An image with 1920x1080 pixels is sent to the SLM with pixel values going from 0 to 256, representing a phase retardation going from 0 to 5.4π . The working principle of the LCOS SLM is illustrated in Figure 3-4 (a) and a schematic representation of the setup in which the SLM is used with the PCA array is illustrated in Figure 3-4 (b). The size of the probe beam is increased with a beam expander to cover the 8×8 mm active area of the SLM. The beam then goes through a polarizer that acts as a filter and is finally reflected by the SLM. The polarization of the incident beam needs to be aligned with the long axis of the SLM for a better efficiency.

In order to focus the IR probe beam and move its position horizontally and vertically with the SLM, two options were evaluated. The first one is to display a Fresnel lens pattern on the SLM to create a converging wavefront. By moving the center of the Fresnel lens pattern in both directions, it is possible to steer the IR probe beam. The second option is to display a 2D blaze grating pattern to

change the angle vertically and horizontally of the beam. By placing a physical lens in front of the PCA array, it is possible to focus the light on the gap of each PCA. However, this option was ruled out since the higher orders of diffraction were considerable and less power could be focus.

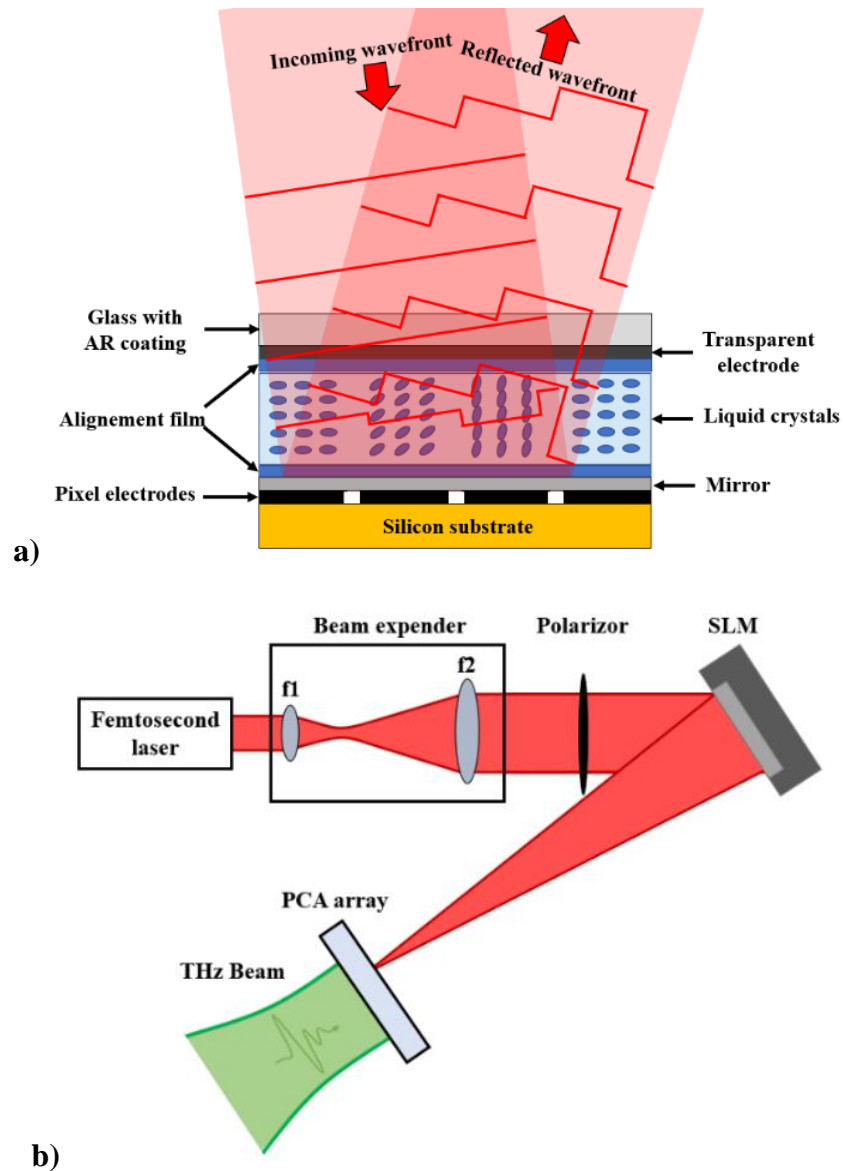


Figure 3-4 **a)** Working principle of LCOS SLM **b)** Schematic representation of the setup in which the SLM is used with the PCA array.

The physical principle behind the ability of SLM to focus light when a Fresnel lens (sometimes called Kinoform lens in the literature) pattern is displayed is well explained in Refs. [115-117]. Let's consider an incoming plane wavefront with a complex amplitude $U(x,y)$. When passing

through an optical medium, the wavefront will be transformed according to the complex amplitude transmittance function $T(x,y) = e^{i\varphi(x,y)}$ of the medium. The wavefront at the exit will be $U'(x,y)$.

$$U(x,y) = e^{i\varphi(x,y)} U'(x,y) \quad (36)$$

Let's consider a simple lens of thickness $d(x,y)$ and a refractive index n . We can define the phase function $\varphi(x,y) = k \cdot d(x,y) \cdot n$, where k is the wave number equal to $\frac{2\pi}{\lambda}$. For a thin lens and within the paraxial approximation, the complex amplitude transmittance function, where F is its focal length, is defined as:

$$T(x,y) = e^{-ik\frac{(x^2+y^2)}{2F}} \quad (37)$$

If we consider a symmetric lens where $r = \sqrt{x^2 + y^2}$, we have :

$$U(r) = e^{-ik\frac{r^2}{2F}} U'(r) \quad (38)$$

Therefore, since the lens changes the phase of the incident plane wave proportionally to r^2 , the planar wavefronts will be transformed into paraboloidal waves centered at the focal distance F . In Figure 3-5, we can see the parabolic phase function for a simple thin lens.

The basic principle of a Fresnel lens is that the phase function is limited between 0 and 2π . Therefore, the initial parabola is split into multiple regions. The phase function of this type of lens is also presented in Figure 3-5. These lenses are useful when high phase change can't be reached like in this project where the maximum phase change of the *Pluto-2* at 780 nm is 5.4π . Since the SLM is pixelated, the phase function is discretized. In order to achieve good diffraction efficiency η , the number of phase levels N in each region needs to be as high as possible. This diffraction efficiency is given by equation (39) [115, 118]. When N tends to infinity, all the power will be in the +1 order of diffraction. Therefore, the diffraction efficiency is simply the ratio of the power in the first order of diffraction over the power in the zeroth order of diffraction when the phase pattern is set to zero all over the SLM. For example, when $N = 8$, the diffraction efficiency for a blaze grating is approximately 96% [119]. This means that with a lower diffraction efficiency, more

optical power will go into the zeroth order and the measured THz signal will be weaker, the noise will be higher and the crosstalk in between the channels of the PCA array should be higher.

$$\eta = \text{sinc}^2\left(\frac{\pi}{N}\right) \quad (39)$$

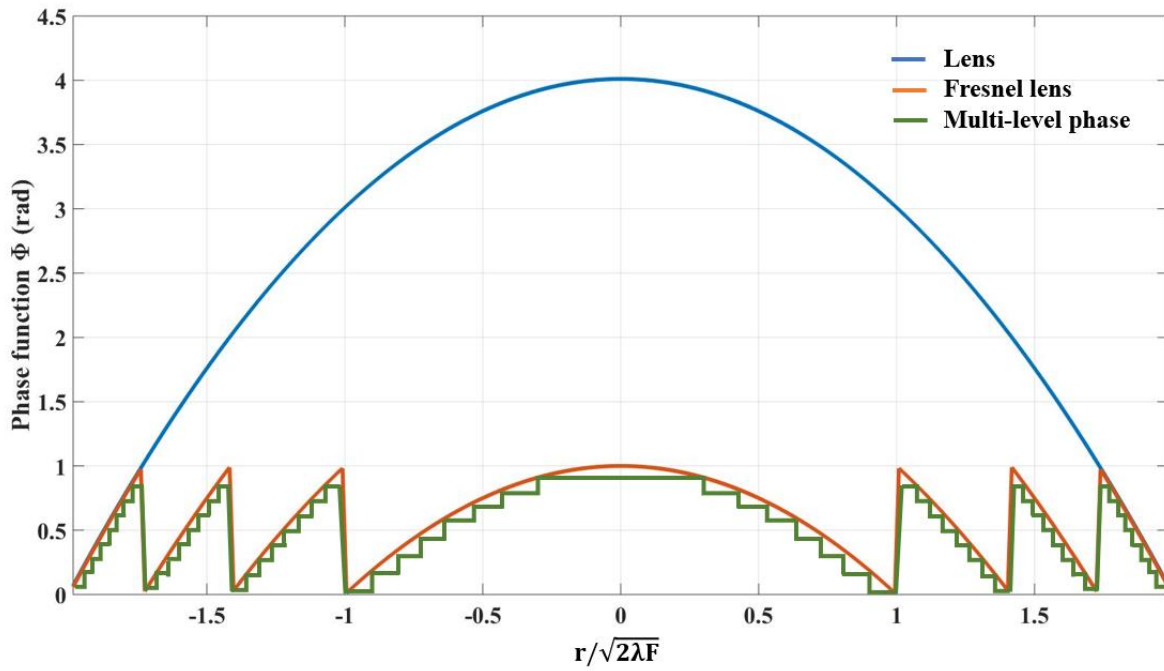


Figure 3-5 Phase function for thin lens, a Fresnel lens and a discretized multi-level phase lens

**CHAPTER 4 ARTICLE 1: FABRICATION AND
CHARACTERIZATION OF AN 8 X 8 TERAHERTZ PHOTOCONDUCTIVE
ANTENNAARRAY FOR SPATIALLY RESOLVED TIME-DOMAIN
SPECTROSCOPY AND IMAGING APPLICATIONS**

4.1 Information

This paper was published in the IEEE Access journal on August 19th 2021 in the Photonic Society section.

DOI : 10.1109/ACCESS.2021.3106227

Pages: 117691 - 117702

4.2 Authors

Henri R.¹, Nallappan K.¹, Member, IEEE, Ponomarev D.S.^{2,3}, Guerboukha H.⁴, Lavrukhin D.V.², Yachmenev A.E.², Khabibullin R.A.² and Skorobogatiy M.¹, Senior Member, IEEE

¹Génie physique, Polytechnique Montréal, 6079 C. P. Montréal, Quebec H3C 3A7, Canada

²Institute of Ultra High Frequency Semiconductor Electronics of RAS, 117105 Moscow, Russian Federation

³Prokhorov General Physics Institute of the Russian Academy of Sciences, Moscow 119991, Russia

⁴Brown University, Providence, RI, 02912, United-States

Corresponding author: Skorobogatiy M. (e-mail: maksim.skorobogatiy@polymtl.ca).

This work was supported in part by the Canada Research Chair Tier I in Ubiquitous Terahertz Photonics and by the Russian Science Foundation, grant #18-79-10195

4.3 Abstract

Terahertz (THz) technology is promising in several applications such as imaging, spectroscopy and communications. Among several methods in the generation and detection of THz waves, a THz time-domain system that is developed using photoconductive antennas (PCA) as emitter and detector presents several advantages such as simple alignment, low cost, high performance etc. In this work, we report the design, fabrication and characterization of a 2-D PCA array that is capable of detecting both the amplitude and phase of the THz pulse. The PCA array is fabricated using LT-GaAs and has 8 channels with 64 pixels (8x8). A novel approach using a spatial light modulator (SLM) to steer and focus the infrared probe beam towards pixels of the PCA array is presented. Each channel records the photocurrent generated by the THz signal (amplitude and phase) separately and frequencies up to 1.4 THz can be detected. Furthermore, the parameters such as directional time delay of the THz pulse, crosstalk between the channels etc., were characterized. Finally, we show that the proposed 2D PCA array design is flexible and can be used for accelerated THz spectral image acquisition.

4.4 Introduction

Terahertz (THz) frequency band (0.1 to 10 THz) has received a lot of attention in recent years due to increasing number of technological applications in the fields of telecommunications, imaging and sensing[120-126]. Due to its non-ionizing nature and higher penetration depth when compared to optical infrared (IR) waves, the THz imaging is promising in such applications as security screening[43, 45, 127], biomedical imaging[35, 50, 128-131] and industrial process control[49, 132]. Moreover, the THz waves feature higher spatial resolution when compared to microwaves which attracted development of commercial THz imaging systems[133].

The THz imaging systems can be classified into two types: continuous wave (CW) THz imaging systems and pulsed THz time-domain imaging systems. The CW THz imaging systems offer compact, cost-effective, and relatively high power (compared to the THz time-domain systems) solutions for industrial applications in which a THz image at a given frequency can be obtained via raster scanning using a photomixer or Schottky detector [134, 135]. Although the CW THz system has higher frequency resolution (~ 100 MHz) compared to a pulsed THz system, it requires a long

acquisition time (several minutes per pixel depending on the integration time and frequency resolution) to obtain a wide frequency spectrum with high signal-to-noise ratio, which limits its application in the fields of multi/hyperspectral imaging and real-time imaging. Moreover, emitters for CW THz imaging system in the form of photomixers are considerably more expensive than photoconductive antennas used in pulsed THz time-domain systems. On the other hand, the THz time-domain system is the most commonly used imaging system as it allows recording a broadband THz pulse in a single acquisition sweep, with the following full spectrum reconstruction via Fourier transform of a time-domain pulse. In such systems, the duration of the THz pulse acquisition is mainly limited by the sweeping speed of the optical delay line (typically in the form of a linear micro-positioning stage), as well as integration time that controls a signal-to-noise ratio. In the THz time-domain systems, the frequency resolution is typically on the order of ~ 10 GHz, and while finer resolutions are readily achievable ~ 1 GHz, they require higher values of optical delay (longer scanning ranges of a mechanical stage), thus resulting in longer image acquisition times. Similarly, smaller mechanical displacements of the optical delay stage are necessary in order to increase the upper frequency limit of the reconstructed THz spectrum, which again results in longer acquisition times. Several solutions have been proposed to decrease the acquisition time of the THz time-domain system such as asynchronous sampling[13, 136], fast rotary optical delay line[14], oscillating optical delay lines[15], etc. However, even if faster techniques for optical delay scanning are used, as the power in THz time-domain system is spread over a large frequency band, such systems tend to be noisier than the CW THz systems, thus requiring longer integration times. In the context of this work, the key advantage of the pulsed THz time-domain approach compared to CW THz approach is the ability of integrating many photoconductive antennas on a single chip, which is in stark contrast to photomixers, which are technologically more difficult to fabricate and are currently available only as stand-alone devices.

The image acquisition speed in THz time-domain systems is also limited by the necessity of 2D raster scanning using a single pixel detector such as a PCA [16], a nonlinear crystal [137, 138] or Air-based-coherent-detectors (ABCD) [139]. By employing mechanical beam steering [140, 141] or compressed sensing techniques such as phase mask encoding [142], spectral/temporal encoding[143], etc., the image acquisition speed can be improved even when using a single pixel detector[28].

To further improve the image acquisition speed in THz time-domain systems, the multipixel detectors such as bolometer arrays[64] and Complementary Metal Oxide Semiconductor (CMOS) cameras[144] are proposed. In these approaches, only the amplitude of the THz electric field is detected, while phase information is lost. In practical applications, however, phase information is highly desirable as it allows direct measurement of the material's dielectric constant and/or sample geometry [143].

One of the promising techniques to increase the image acquisition speed and simultaneously to record both amplitude and phase information is to use the PCA arrays. In 2002, Herrmann et al., proposed and demonstrated the first 1D PCA array with 8 antenna elements separated by 500 μm each [84]. The antenna was fabricated using low-temperature grown GaAs (LT-GaAs), while particular attention was given to the receiver electronics in which the authors used alternate pulse locked gated integrator (APOGI) by replacing the commercial multichannel lock-in amplifiers. In 2008, Pradarutti et al., demonstrated the 1D PCA array by increasing the number of antenna elements to 16[18]. There, the efficiency of the PCA array was improved by illuminating the probe beam using microlens array and by simultaneously measuring the THz pulse from all the antenna elements. They further increased the number of antenna elements to 128 (1-D) in the following work [85]. In 2014, Brahm et al., demonstrated the fabrication of a 1D PCA array (15 antenna elements)[111] using InGaAs/InAlAs multi-layer heterostructure substrate for the excitation wavelength of 1030 nm. All these works show that the fabrication of multipixel PCA array is promising for the development of high-speed THz imaging system. However, most of the systems discussed above use simultaneous illumination of the whole array with a high-power probing light, also requiring a microlens array for focusing the probing IR light onto the individual photoconductive antennas. The incorporation of a microlens array is an additional step in the fabrication process which further complicates the PCA chip design, while the necessity of using pulsed IR sources powerful enough to interrogate all the pixels simultaneously might considerably increase system costs. Moreover, by using the microlens array, the chance of cross-talk between the neighboring pixels is high as probing IR beams interrogate all the pixels simultaneously. Additionally, complex wiring required to access every PCA element in the array further complicates design of such chips and require novel solutions.

In order to increase the sensitivity of the PCA-based arrays, plasmonic nano-antenna arrays were proposed. Thus, in 2016, Yardimci et al. reported a large area detector with a high THz sensitivity (dynamic range of ~ 90 dB), and broadband operation range (~ 5 THz) [79]. In 2020, Li et al., presented a 63-pixel (9x7) focal plane array of plasmonic nano-antennas [19]. They achieved detection bandwidth of more than 2 THz for all their pixels with the signal-to-noise ratio greater than 60 dB. The main challenge with their design is the complexity of the readout circuit since each pixel was interrogated sequentially. Particularly, they used 4 multiplexers and a FPGA development board to route the THz signal from 63 pixels to a single transimpedance amplifier and a commercial single-channel lock-in amplifier. Therefore, they could only read 1 pixel at the time resulting in slower THz image acquisition speed.

In this article, we present the design, fabrication and characterization of an 8-channel array of 8x8 PCA antennas (64 pixels) with a goal of its further applications in real-time THz spectral imaging. The 2D PCA array was fabricated using LT-GaAs and its performance was characterized within the THz time-domain operation modality. A spatial light modulator (SLM) is used to form the wavefront of a probing IR beam by focusing it onto a single or multiple (chosen at will) PCA antenna elements. This novel approach for PCA array interrogation comes with multiple advantages. One of them is non-mechanic fast optical beam steering with the possibility of using multiple focal spots in order to interrogate multiple antennas simultaneously. In this case, antennas are grouped into separate channels (in our case 8 channels) that can be interrogated in parallel (i.e. by using 'N' transimpedance amplifiers for 'N' number of channels), thus speeding up image acquisition, and dramatically simplifying the on-chip wiring. Moreover, using SLM for interrogation allows smart power budget allocation depending on the total available power of the light source. For example, the number of pixels interrogated in parallel (hence, the number of focal spots generated by SLM) can be increased at the software level when using higher power pulsed IR lasers. At the same time, for a low power laser, one can use just a single beam spot (sequential pixel readout). Furthermore, by combining the proposed technique with the fast optical delay scanning [14](rotary delay line for example[145]), the image acquisition speed can be further improved.

4.5 Design and fabrication of the Photoconductive Antenna array

The schematic of the proposed PCA arrays is shown in Fig. 1 (a). The array is comprised of 8x8 dipole H-type PCAs featuring a 100 μm photoconductive gap. The distance between two neighboring electrodes is 150 μm , the area of contact pads is 150x150 μm^2 . The PCA array was fabricated in two steps. The LT-GaAs was used as a photoconductive substrate. The 0.5 μm thick LT-GaAs was grown via molecular-beam epitaxy using Riber 32P system at 220°C on a semi-insulating GaAs(001) wafer (BEP III/V ratio ~ 35). To improve the LT-GaAs characteristics [146] and isolate the photoconductor from the wafer, a 50 nm thick AlAs layer was sandwiched between the LT-GaAs and the wafer. The LT-GaAs was then annealed at 600°C within 20 min in the growth chamber.

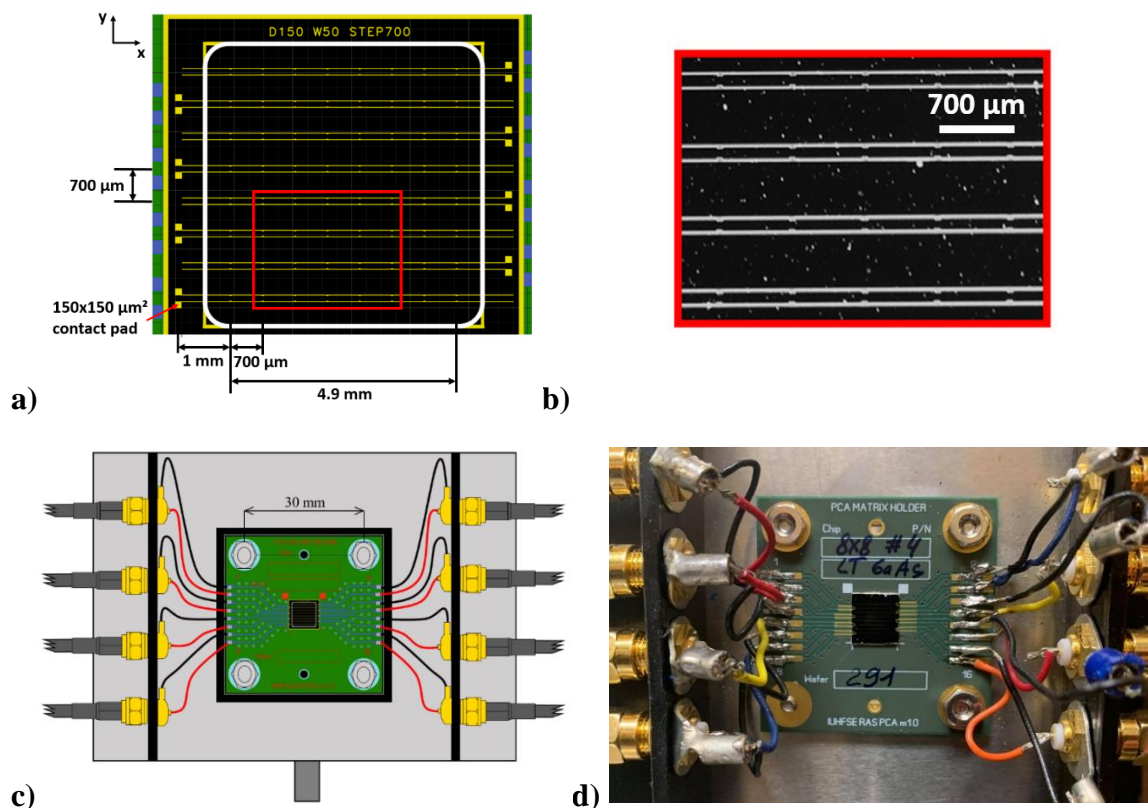


FIGURE 1. PCA detector array for THz time-domain imaging system. **a)** Schematic of the 8x8 PCA array. **b)** Microscope image of a part of the complete array showing 4 channels with 5 PCAs each **c)** Schematic of the PCB and holder assembly for the PCA array **d)** Photograph of the PCA array detector mounted on the PCB

Then, the PCA array was fabricated using an electron-beam lithography (EBL). The sample was dehydrated on the hotplate at 180°C and coated with 540 nm/250 nm thick Copolymer/PMMA 950K bilayer resist stack. The required pattern was exposed via Raith 150-TWO EBL system at 30 kV and developed in an IPA:DI water mixture (1:3) to provide a proper lift-off profile. Then, we used an oxygen plasma descum processing followed by HCl (1:5) solution pretreatment to remove the oxides from the surface of LT-GaAs. Finally, the 50 nm/450 nm thick Ti/Au metallization was deposited on the surface of LT-GaAs via resistive thermal evaporation. The fabrication routine of the single PCA in the array is similar to that reported in our previous paper[147, 148]. In Fig.1 (b), we present the microscope image of a part of the PCA array for the region marked in Fig.1 (a) showing 4 channels and 5 PCA elements each. The 6x6 mm² array was then mounted on a PCB board with a window for THz access on its backside as shown in Fig.1 (c-d).

On the PCB, there are 16 conductive tracks and each of them is connected to a contact pad. The two conductive tracks associated with one row of PCA are connected to a ring terminal with simple wires. A low noise cable with SMA and BNC connectors was then used to forward the signal towards the transimpedance amplifiers. This means that there are 8 detection channels and that each of them corresponds to a row of 8 PCA elements.

4.6 THz Time-domain system with SLM-Driven parallelized acquisition

Schematic of the experimental setup used for characterization of the THz PCA array is shown in Fig. 2. A femtosecond laser with the center wavelength of 780 nm, average power of 63 mW, pulse duration of <100 fs and repetition rate of 100 MHz was used as the IR laser source. The laser beam was divided into pump and probe beam using a 70:30 beam splitter (~19 mW for pump beam and ~44 mW for probe beam) and a PCA from Menlo system[113] was used as the THz emitter. A variable optical attenuator was used to control the power of the pump beam and finally a 10 mW pump power was used for the excitation of the THz emitter. In the detector section, due to higher reflection losses in SLM, the available probe power was much lower (~9 mW) for the excitation of the THz detector PCA array. Therefore, only a single spot was used (sequential pixel readout) during PCA interrogation. Two parabolic mirrors were used to collimate and focus the THz beam

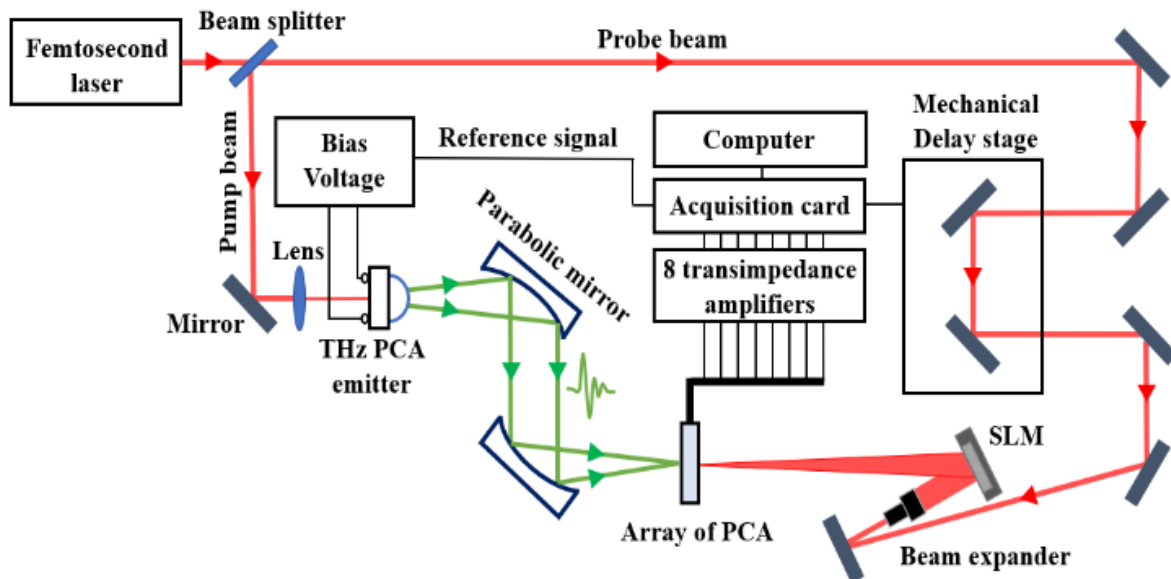


FIGURE 2. Schematic of the THz time-domain system for characterizing the PCA Array. A spatial light modulator was used for focusing and steering the femtosecond laser beam on each PCA element of the Array.

into the detector with the resultant THz beam spot roughly covering the entire 5mm x 5mm area of the PCA array. When compared with the standard THz time-domain system, the pump beam section (emitter side) is identical while the probe beam section (detector side) was modified for probing the PCA array. Particularly, a SLM (*Holoeye Pluto with 1920 X 1080 pixels*) [149] was used to steer and to focus the incoming expanded probe beam into the PCA array as shown in Fig. 2.

The spot size of the incident probe beam on the SLM was ~ 8 mm which covers $\sim 1000 \times 1000$ pixels. The SLM was placed 30 cm away from the PCA array and a single focal spot size of ~ 200 μm was achieved by displaying a Fresnel lens pattern on the SLM. It is also noted that the higher diffraction of the Fresnel lens pattern was ignored as they carry very low power and their influence in the characterization of PCA array was neglected. The main advantage of using SLM is that a multifocal spot can be trivially created to interrogate all 8 channels simultaneously, while the beam steering can be performed as fast as 60 Hz. Finally, the measured photocurrent from the 8 channels of the PCA array was amplified using 8 dedicated low-noise transimpedance amplifiers

from *FEMTO* [150]. A high-speed data acquisition device from *National Instrument* was used to measure the reference signal and the output signals of the 8 transimpedance amplifiers. A multichannel virtual lock-in in *LabVIEW* was developed to extract both phase and amplitude information of the THz pulse. It is noted that, when a lock-in amplifier is used to detect a THz signal modulated at a frequency Ω , two components $E_X(t)$ and $E_Y(t)$ are obtained.

$$E_X(t) = \langle J(t, t') \cos(\Omega t') \rangle \quad (1)$$

$$E_Y(t) = \langle J(t, t') \sin(\Omega t') \rangle \quad (2)$$

where $J(t, t')$ is an instant photocurrent as measured using transimpedance amplifier at a time t' for a fixed optical delay value t . Average $\langle \dots \rangle$ is a time integral over integration time t' . Here t is the time delay as provided by the optical delay line. By combining Eq. (1) and Eq. (2), we get a complex THz signal $E(t)$:

$$E(t) = E_X(t) + iE_Y(t) \quad (3)$$

The THz pulse amplitude in time-domain is defined as $abs(E(t))$. In the Fourier space $E(\omega) = FFT(E(t))$, the spectral amplitude is defined as $abs(E(\omega))$, while phase is $arg(E(\omega))$. The above definitions for the THz amplitude and phase were used in the rest of the paper.

4.7 Calibration of the THz Photoconductive Antenna array

Before imaging, we perform two calibration steps of the PCA array. The goal of the fully automated calibration process is to locate the position of the 64 PCA elements in the reference frame of the SLM. By moving the center of the Fresnel lens pattern displayed on the SLM pixel by pixel in both spatial directions (X and Y directions), the focused laser probe beam is steered to scan the whole surface of the PCA array. Therefore, 64 positions of the Fresnel lens pattern on the SLM must be identified, which represent the different positions on the PCA array where maximum THz pulse

amplitude is detected. It is noted that the focal length of the Fresnel lens on the PCA array was optimized and remains fixed throughout the calibration process.

The first step in the calibration is to locate each channel of the detector array by measuring the drop in the channel resistivity via photoexcitation of the charge carriers in the gap between the two electrodes of a channel. Particularly, the resistance of a channel will drop drastically when the laser probe beam is focused near either one of the two electrodes of a channel. Thus, by steering the laser beam along the Y axis of the detector, one can easily identify the approximate position of each channel. The second step is to locate precisely where the THz pulse is detected with a maximal amplitude. By moving the laser probe beam across the PCA array and recording the THz signal for each position, it is possible to identify the exact location where the detection of the signal is optimal. As recording the THz pulse takes longer duration due to the slow scanning speed of the optical delay line used in our system, measuring of the channel resistance first provides a time-efficient method to identify the region of interest on the PCA chip.

The schematic of the calibration process is shown in Fig.3 (a), where the incident laser probe beam on the SLM is focused onto the PCA array. One pixel in the SLM reference frame corresponds to $7\mu\text{m}$ distance in the PCA chip. This is identified based on the known dimensions of the PCA array ($100\mu\text{m}$ gap at the H-structure and $150\mu\text{m}$ spacing between the electrodes). In Fig. 3 (b), we present the normalized value of the channel resistance, as well as the THz pulse amplitude as measured while scanning the IR laser beam across the black dotted line that traverses channel 5 as shown in Fig. 3 (a). We clearly observe two positions near the electrodes where the channel resistance drops, as well as four maxima in the recorded THz signal amplitude when focusing laser beam at the electrode edges. The amplitude of the THz pulse depends on the polarity of the electrode that is connected to the transimpedance amplifier. This was verified by reversing the polarity of the channel and observing the two highest THz amplitude peaks switching to the adjacent 2-peak group. This phenomenon can be explained by noting that in addition to the structure of the antenna, the lifetime and mobility of the charge carriers play a significant role in the detection of THz signal [151]. In LT-GaAs, the electron and hole carrier lifetimes are 0.1 ps and 0.4 ps, and the initial electron and hole mobilities are $200\text{ cm}^2/\text{V s}$ and $30\text{ cm}^2/\text{V s}$, respectively. Due to the difference in the lifetimes and mobilities of electrons and holes, the detection at the electrode that is connected to the positive terminal of the transimpedance amplifier will be

predominant. This phenomenon is known for PCA emitters where the THz power is maximal when the laser beam is focused close to the anode[152-156].

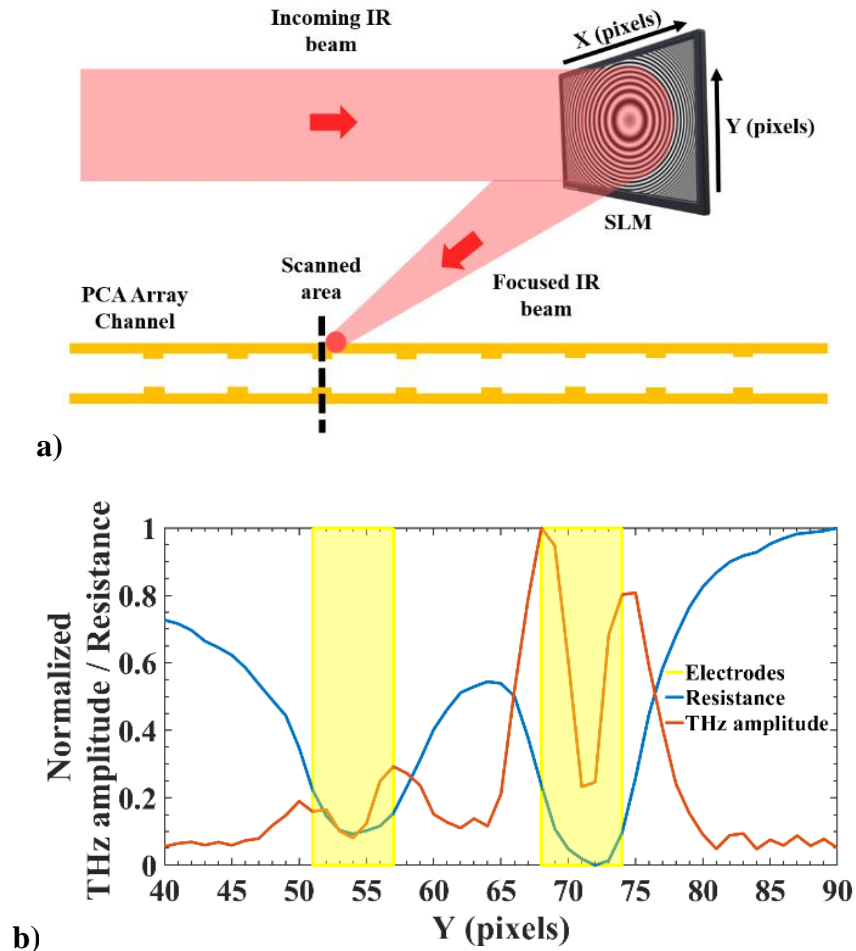


FIGURE 3. A single pixel (detector) characterization within an 8x8 PCA array **a)** Schematic of the probing beam path on the PCA array chip. The Fresnel lens pattern is used to focus and steer the laser probe beam of spot size $\sim 200 \mu\text{m}$. **b)** Resistance and THz amplitude of the third PCA element of channel 5 which is measured by steering the laser probe beam along the Y-direction (see black dotted line shown in **a)**). Two resistance drops are observed when the laser probe beam is focused directly on the metallic electrodes of the channel. Two THz pulses with higher amplitude were observed when the laser probe beam is focused on the edges of the metallic electrode associated with the positive terminal of the transimpedance amplifier and two THz pulses with lower amplitudes were observed while focusing at the edges of the negative terminal.

The final step in the calibration process is to precisely locate the 8 antenna elements of each channel (2D) of the detector. As an example, the resistance map measured in the channel 5 of the PCA array as the region of interest is shown in Fig. 4 (a). Similarly, the two THz peaks associated with the electrode that is connected to the positive terminal of the transimpedance amplifier were measured and the corresponding THz amplitude map is shown in Fig. 4 (b). It should be noted that the amplitude of the THz pulse is smaller at the edges of the channel (X-direction) when compared to its center because of the lower power of the laser probe beam at the edges due to higher diffraction order of the Fresnel lens pattern and also due to the Gaussian distribution of the incident THz beam. We can also observe that THz signal is detected by all 8 H-gap antennas (A1 to A8). It is also interesting to note that while the detected THz signal is the strongest when focusing the probing IR beam within the H-gaps, the weaker THz signal can be still detected by focusing laser beam elsewhere along the electrode edge within the channel. In Fig. 4(c) we show time-resolved THz pulses acquired at the positions of the maximal THz amplitude as determined during the calibration procedure presented in Fig. 4 (b). The relative time delay between the THz pulses is due to different spatial positions of the corresponding acquisition locations along the channel. The ability of a 2D antenna array to measure spatial distribution of a pulse delay can be used for the THz radar applications to locate the direction and extrapolate the location of a THz light source.

In Fig. 4 (d), we present the time-resolved THz pulses for the position A4 and A4' (4th antenna element of channel 5) as marked in Fig. 4 (b) which correspond to the laser beam being focused on either one of the two edges of the electrode that is connected to the positive terminal of the transimpedance amplifier.

In Fig. 4(e), we present the Fourier transform of one of the THz pulses measured with the array detector. The THz frequencies up to 1.4 THz can be detected. The oscillations in the spectrum can be explained by the Fabry-Perot effect due to resonances of the THz light inside the detector substrate. In a classical one-pixel PCA detector, a silicon lens is typically placed at the detector surface to focus the THz light into the antenna substrate, which also helps with decreasing the effect of standing waves. To reduce multiple reflections in the antenna array, an 8x8 micro-lens array could be designed to focus the THz light on each of the PCA detectors, or a THz antireflection coating can be used to optimize an array performance in the vicinity of a certain frequency, however, we defer further improvement to the array performance to our future work.

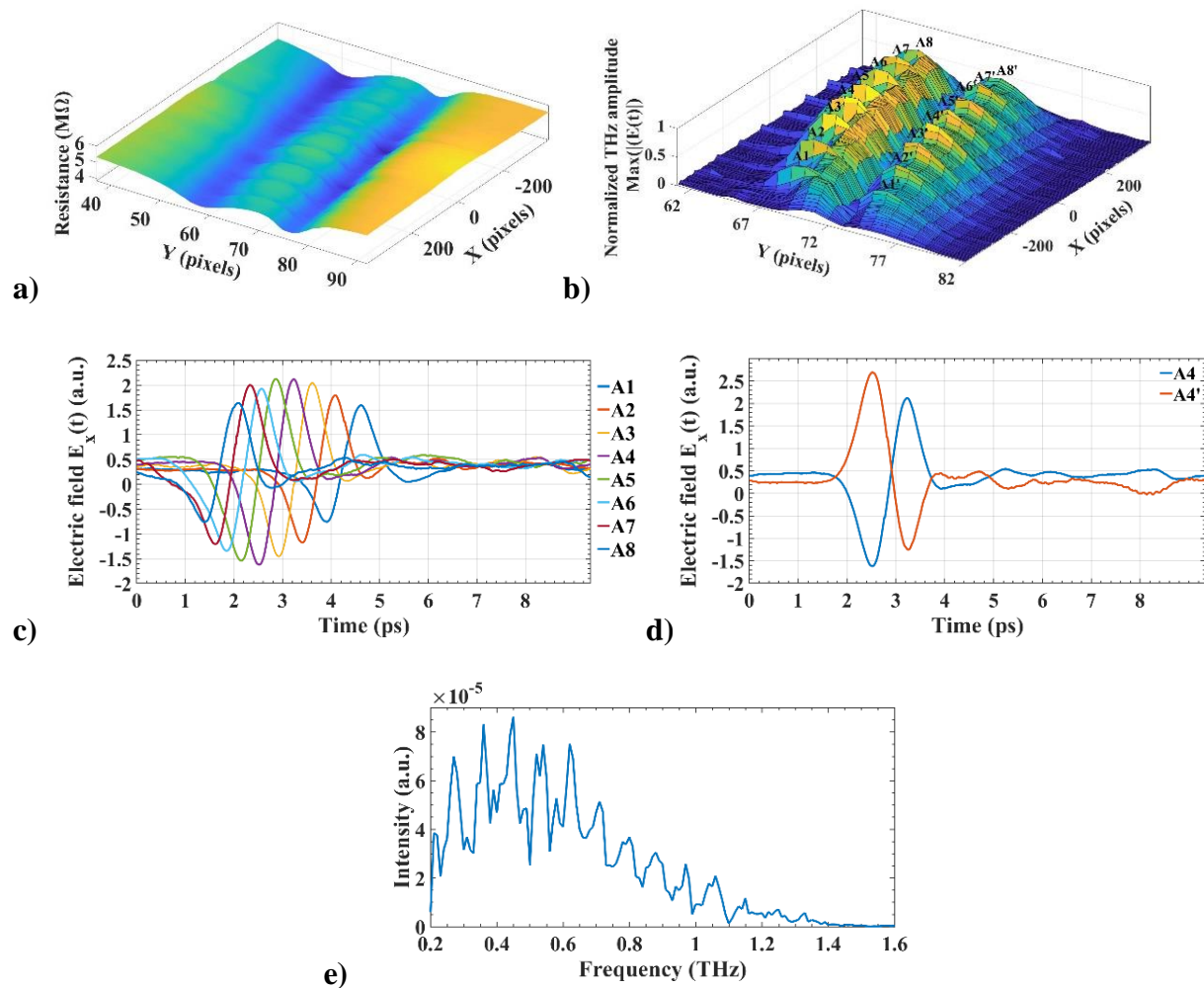


FIGURE 4. Channel characterization within an 8x8 PCA array. **a)** Resistance map for one of the channels (channel 5) in the array. The X and Y axes represent the position of the Fresnel lens center in the SLM reference frame. **b)** Amplitude of the THz pulse signal for the electrode that is connected to the positive terminal of the transimpedance amplifier (right electrode of the two seen in **a)**). **c)** THz pulses measured at the locations A1 to A8 as defined in **b)**. **d)** THz pulse measured in the position A4 and A4' as defined in **b)**. **e)** Fourier Transform of the pulse recorded at A4.

In array-based detectors, one of the major concerns is the channel crosstalk between the neighboring channels, which limits the sensitivity of the system. Therefore, in the following, we measure the crosstalk between the channels of the proposed PCA array. In order to estimate the channel crosstalk, the laser probe beam was focused into the fourth dipole antenna of the fifth channel located near the center of the PCA array. Then, the THz signal was measured at the neighboring channels as shown in Fig.5. From the figure we see that the maximal crosstalk of 15% (by field) is observed for the immediate neighboring channels (channel 4 and channel 6), while the crosstalk decreases rapidly for the channels that are further away. The channel crosstalk can be also minimized computationally after measuring all 64 spectrally resolved crosstalk matrices by exciting one antenna at a time and measuring crosstalk at the location of other antennas.

4.8 Imaging using the THz PCA array

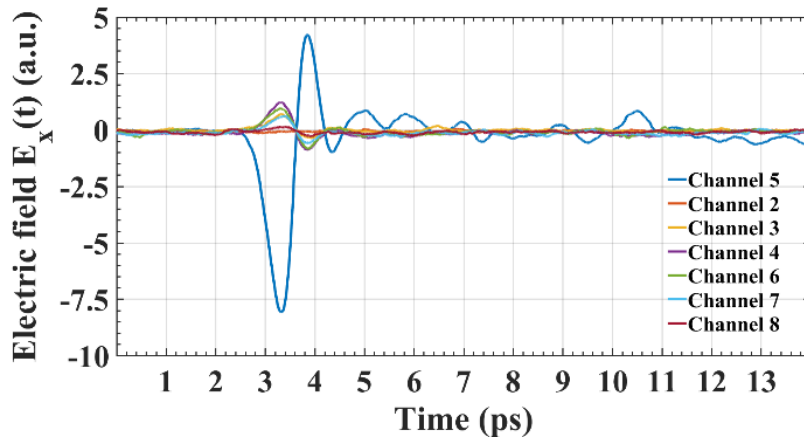


FIGURE 5. Inter-channel crosstalk within the PCA detector array. The laser beam is focused onto a single PCA element (#4) of the channel 5. The signals measured at the neighboring channels (2, 3, 4, 6, 7 and 8) are shown.

In order to use all the 8 channels of the detector for imaging, an array calibration is generally necessary. First, one must find the position of the 64 pixels (defined as locations of the local maxima in the THz amplitude), and then for each pixel (with indices $c=(1,8)$ for the channel number, and $p=(1,8)$ for the pixel number within a channel) record the complex reference THz pulses $E_{c,p}^{ref}(t)$ under illumination conditions that will be later used in imaging. Then, one would

insert an object under study into the path of a THz beam and record a modified set of the THz pulses $E_{c,p}^{obj}(t)$. The complex spectral images of an object $S_{c,p}(\square)$ (that include amplitude and phase information) can be retrieved by Fourier transforming the detected THz pulses and then dividing them by the complex spectral amplitudes of the reference pulses according to Eq.(4).

$$S_{c,p}(\omega) = \frac{E_{c,p}^{obj}(\omega)}{E_{c,p}^{ref}(\omega)} \quad (4)$$

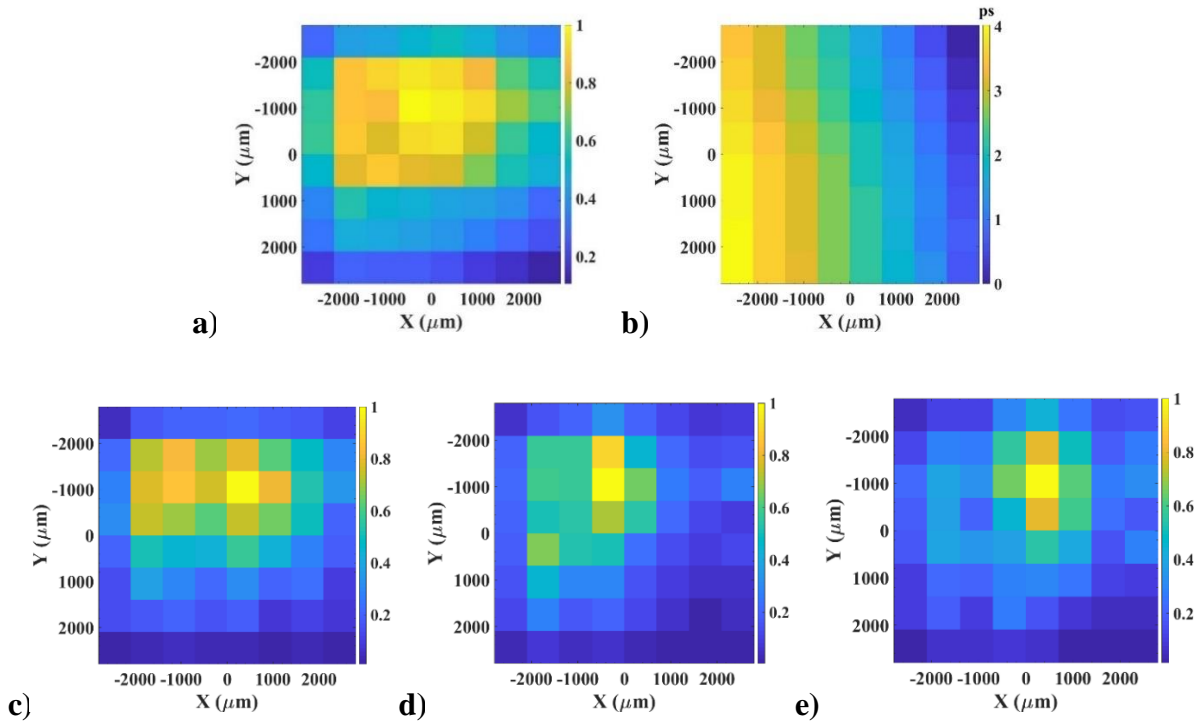


FIGURE 6. A reference image of the THz beam (empty system). **a)** Distribution of the maximal THz beam amplitude ($\max(\text{abs}(E_{c,p}^{ref}(t)))$) of the time-domain pulses as measured by the PCA array. **b)** Distribution of the relative time delay of the time-domain THz pulses with respect to that measured by the top right pixel of the array. Spectral intensity distributions $I_{c,p}^{ref}(\omega)$ of the THz beam at different frequencies **c)** 0.29 THz, **d)** 0.44 THz, and **e)** 0.52 THz.

In Fig. 6 (a), an example of a reference measurement is presented. There we show maximal amplitude distribution $\max(\text{abs}(E_{c,p}^{ref}(t)))$ for the time-domain THz pulses measured with the empty system. In Fig. 6 (b), we present the relative time delay of the THz pulses as registered by

different pixels of an array compared to the top right pixel of the detector. The relative time delay is defined by comparing the temporal positions of the pulse amplitude maxima. A maximum time delay of 4 ps is observed with the bottom left pixel that is 6.9 mm farther away from the top right pixel. There are several reasons for a variable time delay across the PCA array including inclination of the measured THz beam wavefront, as well as variable distance between a SLM and the individual pixels as probed by the focused IR beam. The ability to measure pulse delay distribution across the detector array paves the way to such advanced applications as full spatial characterization of the THz wavefront, distance ranging, THz incidence angle determination, etc., which we will explore in our future work. Although, the THz image obtained is pixelated (700 μm x 700 μm pixel size), the resolution could be improved by increasing the number of pixels along the channel since THz pulse can be detected even in between the H gaps as mentioned earlier. In Fig.6 (c-e), we present the spectral intensity distributions for the focused THz beam (by power) at different frequencies (0.29 THz, 0.44 THz and 0.52 THz), which are found by Fourier transforming the original data $I_{c,p}^{ref}(\omega) = (\text{abs}(E_{c,p}^{ref}(\omega)))^2$. It is then fitted using Gaussian beam profile (see Eq. (5)) along the X and Y direction. From Eq. (5), μ and σ are refers to mean and standard deviation of the Gaussian beam, respectively.

$$f(x, y) = \frac{1}{2\pi \sigma_x \sigma_y} e^{-\left[\frac{(x-\mu_x)^2}{2\sigma_x^2} + \frac{(y-\mu_y)^2}{2\sigma_y^2}\right]} \quad (5)$$

The corresponding frequency dependent spot size ($FWHM_x = 2\sqrt{2\ln 2}\sigma_x$) are found to be 4.4 mm, 2.7 mm and 2.5 mm, respectively. The beam spot size decreases at higher frequencies, which is consistent with the predictions of diffraction theory. From diffraction theory, the focal spot size $2w_0$ ($1/e^2$) for a lens of diameter D , focal length F and wavelength λ can be estimated using Eq. (6):

$$2w_0 = \left(\frac{4\lambda}{\pi}\right) \left(\frac{F}{D}\right) \quad (6)$$

In our THz time-domain imaging system, the focal length and the diameter of the focusing optics (parabolic mirror) are 101.6 mm and 50.8 mm respectively. The FWHM ($2w_0 \cdot \sqrt{\ln(2)} / \sqrt{2}$) for the corresponding THz frequencies (0.29 THz, 0.44 THz and 0.52 THz) are then calculated as 1.56mm, 1mm and 0.87 mm, respectively. When comparing the results of FWHM, we see that values obtained in the experiment are somewhat larger than the ones predicted by the diffraction theory. This can be explained by various factors such as uncertainty in the position of the parabolic mirror focal plane, errors in the beam collimation, as well as multiple reflections in the substrate of a PCA array. It should be noted that for the same reasons, the center of the focal spot of the THz beam at different frequencies changes somewhat its position across the array.

To further demonstrate the abilities of a PCA array to perform amplitude and phase imaging, we carried out two experiments. In the first experiment, the object (sample) is a binary amplitude mask. It was fabricated by printing a thin metallic sheet on paper using hot stamping technique[157, 158]. The schematic and the photograph of the binary amplitude mask is shown in Fig. 7 (a). The sample was placed in front of the detector (stand-off distance between sample and detector is 3 mm due to PCB board thickness) with a metal sheet covering half of the pixels, and the rest of the pixels covered with a paper sheet. As mentioned earlier, a reference was taken with an empty system as shown in Fig.6 (a). By dividing the THz intensity (square of the electric field, $E_{c,p}^{obj}(t)^2$) measured with the sample by the intensity of the reference ($E_{c,p}^{ref}(t)^2$), we obtain Fig.7. (b). Clearly, a maximum amplitude is recorded when the THz light passes through the paper and no signal is recorded for the area covered by the metallic sheet. Moreover, the effect of diffraction on the metallic sheet edge is clearly visible near the center of the sample (metal/paper boundary). In Fig.7 (c), we present the normalized intensity profile along the X-axis of the THz image (see Fig.7 (b)) and its first-order derivative in order to estimate the resolution of the imaging system. The estimated FWHM of the derivative is ~ 1.1 mm. Therefore, the resolution of the THz imaging system is ~ 1.5 pixels (distance between two PCA element is $700 \mu\text{m}$). Since the sample was placed 3 mm in front of the PCA array, the effect of diffraction reduces the resolution of the THz image to ~ 1.5 pixels. However, the resolution can be improved to 1-pixel by reworking the PCB integration and placing the sample closer to the PCA array. Finally, in Fig.7 (d), we present the relative time delay of the THz pulses when passing through the paper sheet as compared to the empty system (reference). As earlier, the relative time delay is defined by comparing the temporal

positions of the pulse amplitude maxima for a system with and without a sample. An average time shift of $\Delta t \sim 0.2$ ps was measured for the paper sheet. This is consistent with a simple estimate of $\Delta t = d(n_p - 1)/c \sim 0.15$ ps relative pulse delay caused by the paper of $100\mu\text{m}$ thick with the refractive index (RI) of $n_p \sim 1.45$ (see [159] for typical values of paper RI in THz).

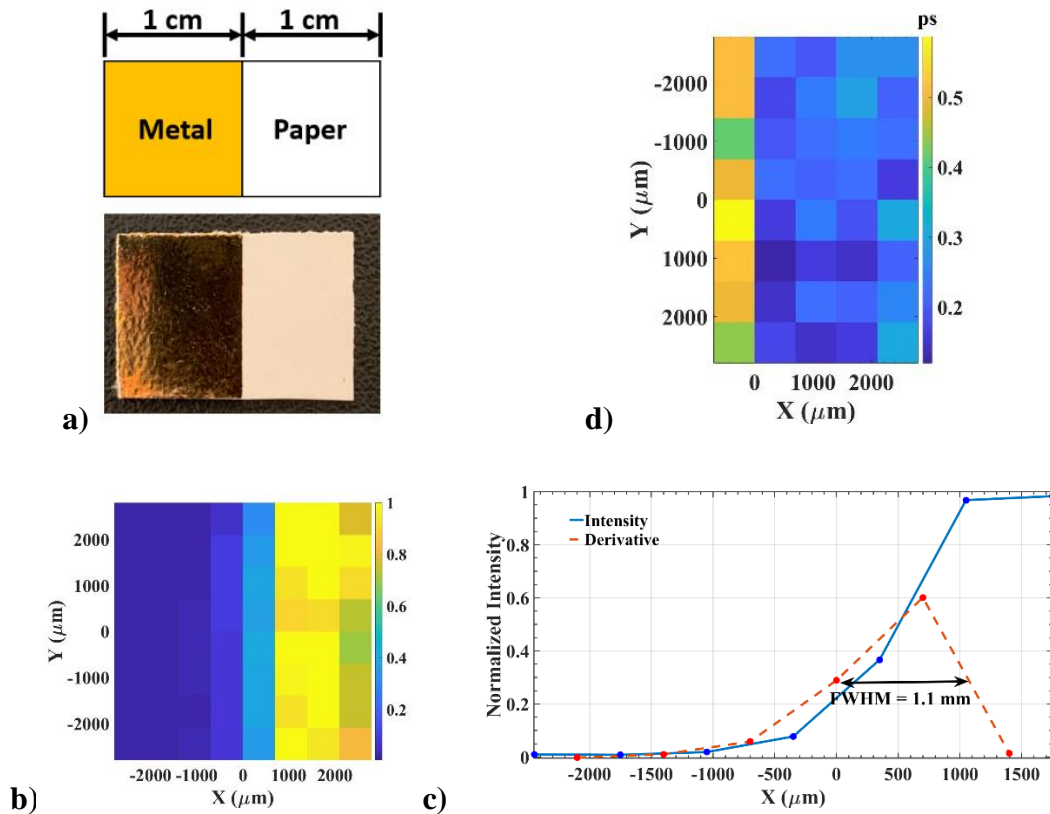


FIGURE 7. THz imaging of binary amplitude mask. **a)** Schematic and photograph of the binary amplitude mask which is fabricated using hot stamping technique. **b)** Relative intensity image of the THz time-domain pulse. **c)** Average intensity along the X axis and its corresponding first-order derivative. **d)** The relative time shift of the THz pulse due to the presence of the paper sheet.

In the second experiment, the sample is a phase mask which was fabricated using a 3D printing technique. A plastic cross with a thickness of $700\mu\text{m}$ was 3D printed on top of a $700\mu\text{m}$ thick substrate using a low-loss polypropylene (PP) polymer. The length and the width of the plastic cross were 2 cm and 1 mm, respectively. In Fig.8 (a-c), we present the schematic, photograph, and microscope image of the phase mask, respectively. The THz pulse was then recorded for each pixel

and the relative time delay of the THz pulse as compared to an empty system (reference) is shown in Fig. 8(d). The shape of the cross is clearly recognizable from the time delay distribution caused by the spatially variable object thickness. From a simple estimate we find that a 700 μm thick PP slab (RI of bulk PP at THz is ~ 1.49 [160]) should result in the relative time delay of ~ 1.1 ps. However, due to porosity of the fabricated structure, the RI of 3D printed PP is lower than the bulk material, and is calculated to be ~ 1.39 from the imaging data of Fig. 8(d). Thus, a relative time delay of ~ 0.9 ps is registered for the porous substrate (700 μm thick) of the phase mask and ~ 1.8 ps for the plastic cross (1400 μm thick), with the most optically dense part being in the cross center.

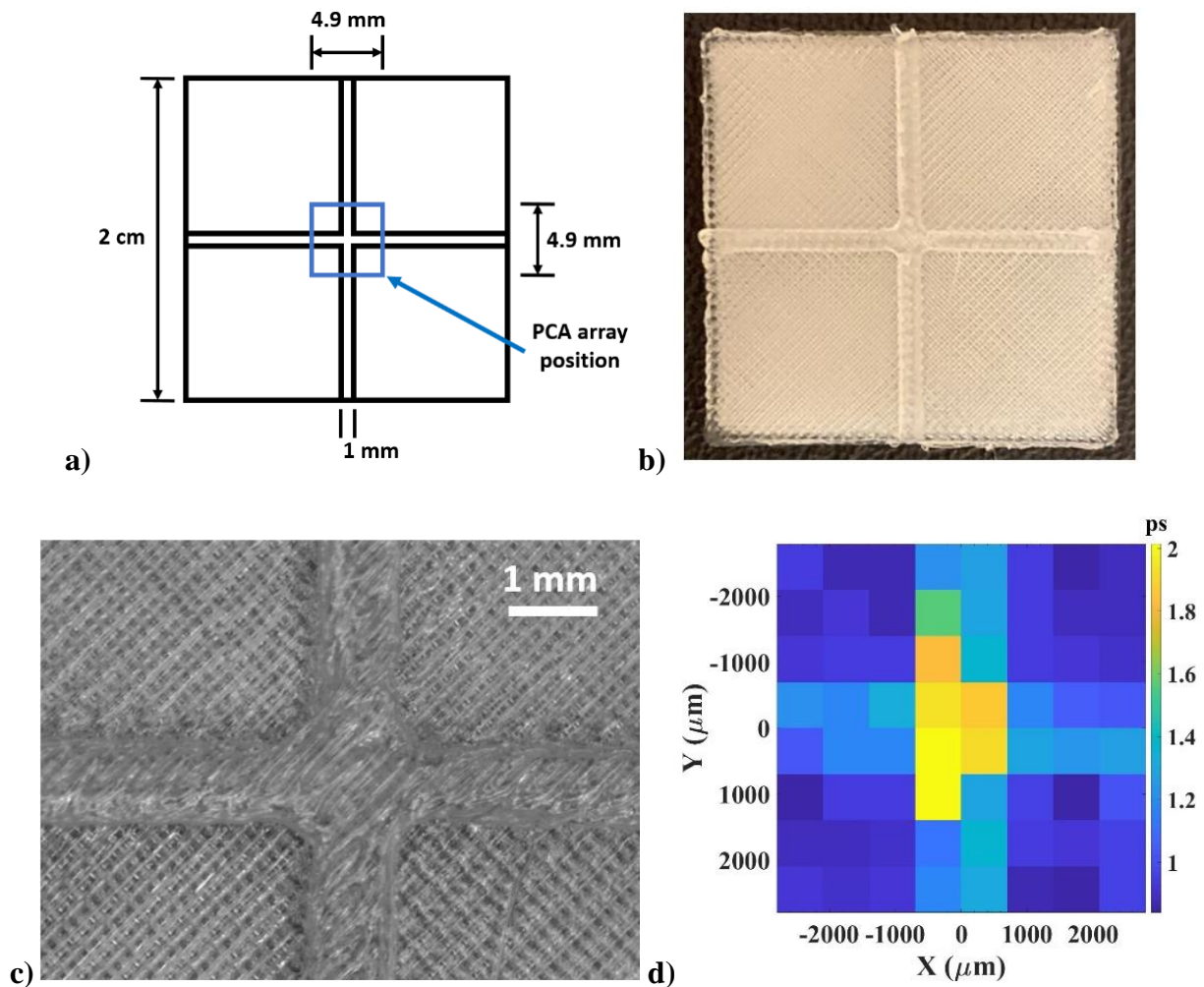


FIGURE 8. Relative time delay measurement of the phase mask. **a)** Schematic diagram of the phase mask (plastic cross). **b)** Photograph of the 3D printed phase mask **c)** Optical microscope image of the phase mask. **d)** The relative time delay of the THz pulse due to the presence of the phase mask as measured by the PCA array.

4.9 Conclusion

In this work, we presented the design, fabrication and characterization of a 2D 8x8 photoconductive antenna array for spatially resolved THz amplitude and phase imaging. First, the locations of optimal interrogation of the individual H-antennas in the detector array are mapped by steering the probe beam using a Spatial Light Modulator. The inter-channel crosstalk is estimated to be as low as ~15% (by field) for the adjacent channels. Then, calibration of the PCA array was performed by

recording THz time traces for an empty system. Finally, we used a thus optimized and calibrated 2-D PCA array to demonstrate both amplitude and phase imaging. For phase imaging, in particular, the relative THz pulse delay of both amplitude and phase mask was demonstrated. A somewhat suboptimal spatial resolution of ~ 1.5 pixels was observed within amplitude imaging modality due to PCB thickness and suboptimal packaging that resulted in ~ 3 mm stand-off distance between samples and PCA array. A high-speed THz image acquisition can be achieved with this system due to 8-channel parallel data acquisition using virtual lock-in, as well as fast multi-beam steering capability of the SLM (60 Hz). The THz image acquisition speed can be further improved by combining high-speed SLMs (up to 2 KHz) [161] which are available commercially with the fast delay line techniques such as rotary optical delay line, oscillating optical delay line, etc. Therefore, we believe that the proposed PCA array can be of practical importance in the development of next generation of real-time spectral imaging systems in the THz range.

4.10 Acknowledgment

Raphael Henri and Kathirvel Nallappan contributed equally to this work.

CHAPTER 5 GENERAL DISCUSSION

In this chapter, we will first discuss the various improvements and modifications on the THz time-domain system to achieve real-time imagery with the PCA array. While an average SNR by field of 35 dB was achieved with the detector, it could be further increased. The first major improvement would be to address all the channels of the detector simultaneously. This could be done by creating 8 focal spots with a diffraction pattern composed of 8 Fresnel lenses. The creation of multiple focal spots with a phase Fresnel lens array was demonstrated in Refs. [162-164]. In Figure 5-1, we can see an example of such array, where 4 Fresnel lenses were displayed on the SLM to create 4 focal spots [162]. For our detector, an array of 8x1 Fresnel lens could be generated to address the 8 channels of the detector simultaneously. This array would then be moved in the SLM's referential to address the 8 antennas of each channel. This means that only 8 frames would be necessary to get the signal from the 64 pixels. This was not implemented in this thesis for the main reason that the probe power was not sufficient.

As mentioned in our paper, the probe power was only 44 mW. Based on a rough approximation, a probe power of 352 mW could be used to create the 8 focal spots. In reality, the diffraction efficiency would decrease as the number of Fresnel lenses increases due to decreasing number of phase levels L (see equation (39)). Since the *Pluto-2* SLM can support up to 2 W/cm², a high-power fs laser, such as the *Mai Tai BB* from *Spectra Physics* with optical power up to 1.5 W and pulse duration below 80 fs [165], could be used. This kind of laser is, however, more expensive than the one used in this project. Moreover, with more power available for the pump beam, a more powerful emitter could be used. While the PCA from Menlo System can only support 10 mW of optical power, a photoconductive antenna array emitter like the *iPCA-21-05-1000-800-h* from *Batop optoelectronics* can support up to 3 W of optical power [166]. These emitters use a micro-lens array and are relatively easy to align. For a power of 1 W, they generate 100 μW of THz power which is much more than the current emitter used.

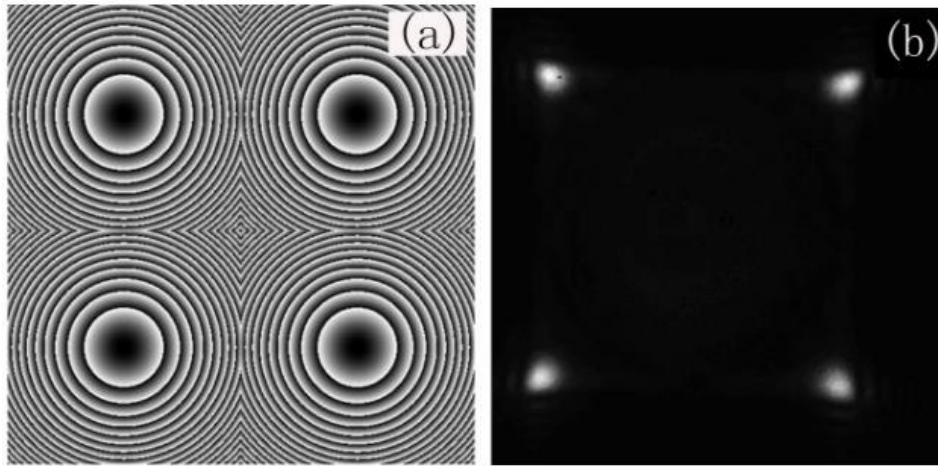


Figure 5-1 **a)** The 2 x 2 phase Fresnel Lens (PFL) array **b)** The 2 x 2 optical traps array generated from PFL array method [162]

The calibration technique proposed in our paper could still be applied with a Fresnel lens array. However, the complexity of the task would be much higher. The main issue is that the SLM and the detector array are not perfectly aligned. In other words, the SLM is slightly tilted horizontally and vertically in relation to the detector. For a single focal spot as proposed in this thesis, a position array (8x8) with the coordinates (x,y) of the center of the Fresnel lens was built. Each pixel is therefore associated with Fresnel lens coordinates where the THz signal is best detected as can be seen in Figure 5-2. Since the SLM is not perfectly aligned with the PCA array, the first pixel of the 4th channel (-322,-18) is a little bit lower than the last pixel of the same channel (334,-13) in the SLM's referential. While this small difference of 5 pixels seems negligible, to achieve a good SNR, the Fresnel lens needs to be positioned precisely as can be seen in Figure 3 (b) of the article. This means that in the case where 8 Fresnel lenses would be used, the process would not be straightforward, since the Fresnel lenses would not be perfectly stacked on top of each other. In fact, the 8 Fresnel lenses would be tilted, and the calibration process would need to be done iteratively to carefully find the 8 optimal positions. This process would be done 8 times to properly address the 64 pixels.

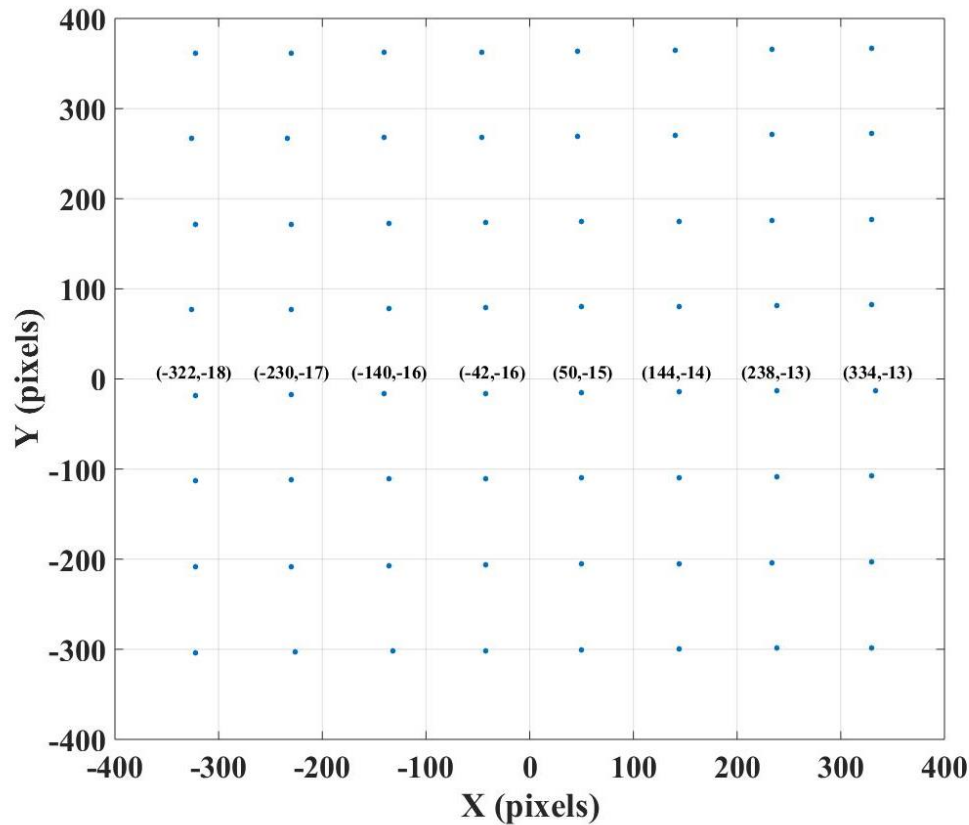


Figure 5-2 Position array associated with each PCA of the array detector. Each coordinate represents a position of the Fresnel lens pattern in the SLM's referential (X pixel, Y pixel). The SLM is slightly tilted compared to the PCA array and therefore each channel or line is not perfectly horizontal in the SLM's referential.

The second major improvement to the system would be to increase the acquisition speed of the system. While commercial SLM can be used as fast as 2 kHz, the main limitation right now is the integration time of the virtual lock-in amplifier. In the current setup, to acquire a THz pulse for one pixel of the PCA array, it takes more than 6 minutes. This means that it takes more than 6 hours to acquire a hyperspectral image with the 64 pixels. This is because an integration time of 500 ms is used to achieve sufficient SNR. To measure a sufficient spectral resolution and the upper frequencies of the spectrum, the delay line is moved on 15 mm (30 mm total) with step size of 0.02 mm for a total of 750 points. The algorithm of the virtual lock-in amplifier would need to be dramatically improved to achieve real-time imaging. Let's consider the hypothetical case where we would like to achieve an FPS of 10 Hz with the detector. If we used 8 Fresnel lenses as proposed

previously, we would need to switch the SLM's frame every 12.5 ms (80 FPS) which is not a problem with the current *Pluto-2*. If we use a rotary optical delay line for example, and we can change the optical path of 30 mm every 12.5 ms and take 750 points, the integration time of the lock-in amplifier would need to be at around 16.67 μ s. This is 30000 times faster than the current setup which is not realistic. There are however commercial single-channel lock-in amplifiers more efficient with these kinds of integration times. In the case where financial resources were not a barrier, 8 of these amplifiers could be used to achieve real-time coherent hyperspectral imaging. However, it is not certain that this kind of integration time would be high enough to achieve good SNR resulting in lower FPS than expected.

Another interesting improvement would be to use a micro-lens array on the THz side of the PCA array to further increase the SNR and to reduce back reflections. In Ref. [167], they proposed a 3D printed plastic micro-lens array for THz focal plane array (see Figure 5-3 a)). In their paper, they designed it to be used with a planar bolometer array and they used Acrylonitrile Butadiene Styrene (ABS) plastic. The refractive index of ABS is approximately 1.6 between 0.2 and 0.7 THz[168, 169]. The absorption coefficient of ABS at 0.5 THz is approximately 4.9 and 12.7 at 1 THz[169]. The main advantages of using the 3D printing technique are its low cost and the ability to quickly iterate the micro-lens array design to optimize the detection. Another interesting option would be to use a micro-lens array made of silicon. The main advantage of using silicon is its high refractive index (3.52 between 0.3 and 2 THz[170]). However, to build micro-lens array of silicon, microfabrication techniques are necessary such as the one proposed in Ref. [171] and shown in Figure 5-3 b). The integration of silicon micro-lens array would be harder since the fabrication process is longer and more expensive.

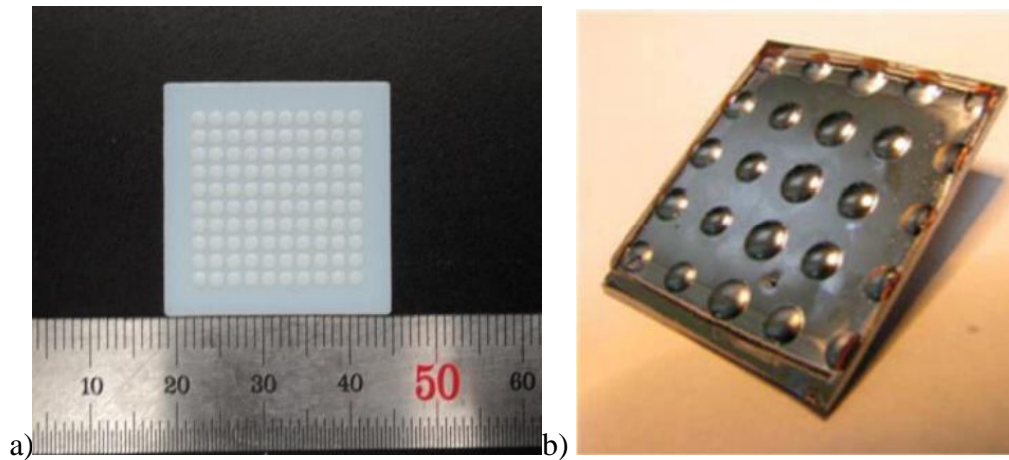


Figure 5-3 **a)** Photographs of fabricated THz lenses (10x10 in ABS) [167]**b)** Fabricated array of silicon shallow lenses [171].

Finally, the number of pixels could be increased on the PCA array. In that case, the number of PCA per channel could be increased as well as the number of channels and additional transimpedance amplifiers would need to be bought. Since the array would be bigger, the SLM would need to be further away from the PCA array, since the probe beam would need to be steered at higher angles (both horizontally and vertically). This would come with the drawback of having bigger focal spots. There is therefore a limit in terms of distance (or focal length) at which the SLM can be used with the PCA array to achieve significant SNR. If the focal spot is too big, the detection is not efficient. Furthermore, the number of channels is limited by the number of Fresnel lenses that can be displayed on the SLM. As mentioned previously, as the number of Fresnel lenses increases, the diffraction efficiency decreases.

One interesting application of the PCA array presented in this thesis is Fourier imaging as proposed in Ref. [143]. They used the fact in Fourier space, spatial frequencies can be equated to spectral frequencies. By using a broadband spectrum, they were able to reconstruct amplitude and phase images while using less pixels than for a normal imaging experiment. They moved their single-pixel PCA detector along a circle while an object is placed in the Fourier plane to create their images. The mathematics behind their technique is well described in their article and the image resolution δr is given by the equation (40).

$$\delta r = 0.5 \frac{cF}{\rho_{max} v_{max}} \quad (40)$$

Where c is the speed of light, F is the focal length, ρ_{max} is the radius of the circle in which the single pixel is scanned and v_{max} is the maximal frequency detected. In the current state of the system, the focal length would be 101.6 mm, ρ_{max} would be 4.9 mm which is the size of the PCA array and v_{max} would be around 1 THz. This means that the image resolution would be approximately 3 mm which is quite high. This resolution could be improved if the array size is increased, or it could be improved if the PCA array is moved along a circle. In order to move the PCA array, there are two solutions. The first one would be to put the SLM and the PCA array on the same 3D stage. Since the SLM is 30 cm in front of the PCA array, the 3D stage would need to be quite strong to precisely move all the components (SLM, SLM driver and power units, PCA array, collimator, optical fiber, beam expander, metallic plate to hold all the components). An optical fiber could be used to route the optical probe beam to the beam expander which would be mounted on the 3D stage. In this case, only one calibration would be necessary (64 positions of the Fresnel lenses) and the measurement would be straightforward. However, each component would need to be fixed solidly due to the sensitivity of the calibration. A small movement of the SLM for example would ruin the calibration and the process would need to be done from the beginning. The second option to move the PCA array would be to keep the system as it is right now and to mount the PCA array on a 3D stage. The goal would be to move the PCA array within the range of the SLM (maximum steering angle of the optical probe beam) and to do a complete calibration for every position of the PCA array (N array of 64 Fresnel lens position for N position of the PCA array). This option would be time-consuming, and the 3D stage would need to be precise with a good repeatability.

CHAPTER 6 CONCLUSION

In this thesis, an 8x8 array of photoconductive antennas was presented for spatially resolved time-domain spectroscopy and imaging applications. As we presented in the literature review, THz time-domain systems lack in coherent detector arrays. The most common way to do hyperspectral imaging is to proceed with a 2D raster scan with a single pixel PCA. This technique is time consuming and is not well suited for real-time imagery.

At first, we presented an elegant solution to address each pixel of the PCA array with a spatial light modulator. We proved that by displaying a Fresnel lens pattern and by moving it pixel by pixel on the SLM, small focal spots could be used to detect THz pulses. We showed that the detection was optimal when the IR probe beam was focused close to one of the electrodes of each channel.

A virtual lock-in amplifier was implemented in *Labview* to detect the 8 channels where each of them is associated with a transimpedance amplifier to further increase the signal. The integration of multiple PCA on the same detection channel is a novelty and opens the way for even bigger PCA array where NxN pixels are detected with N channels and N transimpedance amplifiers. Our virtual lock-in had good performances but the high integration times were needed to achieve sufficient SNR and thus limiting the acquisition speed of the system.

In our published paper, we presented the complete fabrication process and the design of the PCA array, and we presented the THz time-domain system in which it was characterized. A novel calibration technique using a digital multimeter to create a resistance map of each channel and the THz beam itself is proposed. A maximum crosstalk of 15% was observed between the channels and a Gaussian beam was measured with the whole array. An average SNR of 35dB was observed. As frequencies increased, the FWHM of the THz beam decreased as predicted by the diffraction theory. Two experiments were then carried out were at first an amplitude metallic mask was successfully imaged and a resolution of 1.5 pixels was measured. We believe this resolution could be improved to the pixel size in a near-field imaging experiment. In the current state of the PCA, the PCB keeps the object from being closer than 3 mm but simple improvements to the design of the detector could be done. Secondly, a plastic cross was 3D printed in PP and was successfully imaged using the arriving times of the THz pulses to the detector.

Finally, multiple improvements could be made to the PCA array as mentioned in Chapter 6. The first major improvement would be to do paralyzed acquisition with an array of 8x1 Fresnel lens. This could only be implemented if a new fs laser with higher power is bought. This new laser would allow the integration of a new emitter to further increase the THz power. A second improvement would be to design a micro-lens array for the THz signal in order to reduce the back reflections and to increase the SNR. Examples of such arrays have been presented where a plastic 3D printed solution seems to be the easiest one in the short term. Last but not least, a Fourier imaging technique was discussed and is currently a work in progress.

REFERENCES

1. Yang, X., et al., *Biomedical applications of terahertz spectroscopy and imaging*. Trends in biotechnology, 2016. **34**(10): p. 810-824.
2. Wan, M., J.J. Healy, and J.T. Sheridan, *Terahertz phase imaging and biomedical applications*. Optics & Laser Technology, 2020. **122**: p. 105859.
3. Liu, H.-B., et al., *Terahertz spectroscopy and imaging for defense and security applications*. Proceedings of the IEEE, 2007. **95**(8): p. 1514-1527.
4. Kemp, M.C., et al. *Security applications of terahertz technology*. in *Terahertz for Military and Security Applications*. 2003. International Society for Optics and Photonics.
5. Latva-aho, M. and K. Leppänen, *Key drivers and research challenges for 6G ubiquitous wireless intelligence (white paper)*. 6G Flagship research program, University of Oulu, Finland, 2019.
6. Naftaly, M. and R.E. Miles, *Terahertz time-domain spectroscopy for material characterization*. Proceedings of the IEEE, 2007. **95**(8): p. 1658-1665.
7. Fischer, B., et al., *Chemical recognition in terahertz time-domain spectroscopy and imaging*. Semiconductor Science and Technology, 2005. **20**(7): p. S246.
8. Bawuah, P. and J.A. Zeitler, *Advances in terahertz time-domain spectroscopy of pharmaceutical solids: A review*. TrAC Trends in Analytical Chemistry, 2021: p. 116272.
9. Reid, C.B., et al., *Terahertz time-domain spectroscopy of human blood*. IEEE journal of biomedical and health informatics, 2013. **17**(4): p. 774-778.
10. Borovkova, M., et al., *Terahertz time-domain spectroscopy for non-invasive assessment of water content in biological samples*. Biomedical optics express, 2018. **9**(5): p. 2266-2276.
11. Gowen, A.A., C. O'Sullivan, and C. O'Donnell, *Terahertz time domain spectroscopy and imaging: Emerging techniques for food process monitoring and quality control*. Trends in Food Science & Technology, 2012. **25**(1): p. 40-46.
12. Surkamp, N., et al. *Terahertz time-domain spectroscopy by asynchronous sampling with modelocked semiconductor lasers*. in *2018 First International Workshop on Mobile Terahertz Systems (IWMTS)*. 2018. IEEE.
13. Yasui, T., E. Saneyoshi, and T. Araki, *Asynchronous optical sampling terahertz time-domain spectroscopy for ultrahigh spectral resolution and rapid data acquisition*. Applied Physics Letters, 2005. **87**(6): p. 061101.
14. Guerboukha, H., et al., *Time resolved dynamic measurements at THz frequencies using a rotary optical delay line*. IEEE Transactions on Terahertz Science and Technology, 2015. **5**(4): p. 564-572.
15. Jin, Y.-S., et al., *Fast scanning of a pulsed terahertz signal using an oscillating optical delay line*. Review of Scientific Instruments, 2007. **78**(2): p. 023101.
16. Burford, N.M. and M.O. El-Shenawee, *Review of terahertz photoconductive antenna technology*. Optical Engineering, 2017. **56**(1).

17. Brahm, A., et al., *Multichannel terahertz time-domain spectroscopy system at 1030 nm excitation wavelength*. Opt Express, 2014. **22**(11): p. 12982-93.
18. Pradarutti, B., et al., *Terahertz line detection by a microlens array coupled photoconductive antenna array*. Optics Express, 2008. **16**(22): p. 18443-18450.
19. Li, X. and M. Jarrahi. *A 63-Pixel Plasmonic Photoconductive Terahertz Focal-Plane Array*. in *2020 IEEE/MTT-S International Microwave Symposium (IMS)*. 2020. IEEE.
20. Piao, Z.-S., M. Tani, and K. Sakai. *Carrier dynamics and THz radiation in biased semiconductor structures*. in *Terahertz Spectroscopy and Applications*. 1999. International Society for Optics and Photonics.
21. Jepsen, P.U., D.G. Cooke, and M. Koch, *Terahertz spectroscopy and imaging - Modern techniques and applications*. Laser & Photonics Reviews, 2011. **5**(1): p. 124-166.
22. Tani, M., et al., *Emission characteristics of photoconductive antennas based on low-temperature-grown GaAs and semi-insulating GaAs*. Applied optics, 1997. **36**(30): p. 7853-7859.
23. Withayachumnankul, W. and M. Naftaly, *Fundamentals of measurement in terahertz time-domain spectroscopy*. Journal of Infrared, Millimeter, and Terahertz Waves, 2014. **35**(8): p. 610-637.
24. Pupeza, I., R. Wilk, and M. Koch, *Highly accurate optical material parameter determination with THz time-domain spectroscopy*. Optics express, 2007. **15**(7): p. 4335-4350.
25. Duvillaret, L., F. Garet, and J.-L. Coutaz, *A reliable method for extraction of material parameters in terahertz time-domain spectroscopy*. IEEE Journal of selected topics in quantum electronics, 1996. **2**(3): p. 739-746.
26. Withayachumnankul, W., et al., *Uncertainty in terahertz time-domain spectroscopy measurement*. JOSA B, 2008. **25**(6): p. 1059-1072.
27. Neu, J. and C.A. Schmuttenmaer, *Tutorial: An introduction to terahertz time domain spectroscopy (THz-TDS)*. Journal of Applied Physics, 2018. **124**(23): p. 231101.
28. Guerboukha, H., K. Nallappan, and M. Skorobogatiy, *Toward real-time terahertz imaging*. Advances in Optics and Photonics, 2018. **10**(4): p. 843-938.
29. Jansen, C., et al., *Terahertz imaging: applications and perspectives*. Applied optics, 2010. **49**(19): p. E48-E57.
30. Guillet, J.P., et al., *Review of terahertz tomography techniques*. Journal of Infrared, Millimeter, and Terahertz Waves, 2014. **35**(4): p. 382-411.
31. Malhotra, I., K.R. Jha, and G. Singh, *Terahertz antenna technology for imaging applications: A technical review*. International Journal of Microwave and Wireless Technologies, 2018. **10**(3): p. 271-290.
32. Mittleman, D.M., *Twenty years of terahertz imaging [Invited]*. Opt Express, 2018. **26**(8): p. 9417-9431.
33. Hu, B.B. and M.C. Nuss, *Imaging with terahertz waves*. Optics letters, 1995. **20**(16): p. 1716-1718.

34. Sim, Y.C., et al., *Terahertz imaging of excised oral cancer at frozen temperature*. Biomedical optics express, 2013. **4**(8): p. 1413-1421.
35. Bowman, T.C., M. El-Shenawee, and L.K. Campbell, *Terahertz imaging of excised breast tumor tissue on paraffin sections*. IEEE Transactions on Antennas and Propagation, 2015. **63**(5): p. 2088-2097.
36. Brun, M.-A., et al., *Terahertz imaging applied to cancer diagnosis*. Physics in Medicine & Biology, 2010. **55**(16): p. 4615.
37. Woodward, R., et al., *Terahertz pulsed imaging of skin cancer in the time and frequency domain*. Journal of Biological Physics, 2003. **29**(2): p. 257-259.
38. Sun, Y., et al., *A promising diagnostic method: Terahertz pulsed imaging and spectroscopy*. World journal of radiology, 2011. **3**(3): p. 55.
39. Berrier, A., et al., *Selective detection of bacterial layers with terahertz plasmonic antennas*. Biomedical optics express, 2012. **3**(11): p. 2937-2949.
40. Park, S., et al., *Sensing viruses using terahertz nano-gap metamaterials*. Biomedical optics express, 2017. **8**(8): p. 3551-3558.
41. Taylor, Z.D., et al., *THz and mm-wave sensing of corneal tissue water content: in vivo sensing and imaging results*. IEEE transactions on terahertz science and technology, 2015. **5**(2): p. 184-196.
42. Woolard, D.L., J.O. Jensen, and R.J. Hwu, *Terahertz science and technology for military and security applications*. Vol. 46. 2007: world scientific.
43. Chen, J., et al., *Absorption coefficients of selected explosives and related compounds in the range of 0.1–2.8 THz*. Optics express, 2007. **15**(19): p. 12060-12067.
44. Kawase, K., et al., *Non-destructive terahertz imaging of illicit drugs using spectral fingerprints*. Optics express, 2003. **11**(20): p. 2549-2554.
45. AlNabooda, M.O., et al., *Terahertz spectroscopy and imaging for the detection and identification of Illicit drugs*, in *2017 Sensors Networks Smart and Emerging Technologies (SENSET)*. 2017. p. 1-4.
46. Davies, A.G., et al., *Terahertz spectroscopy of explosives and drugs*. Materials today, 2008. **11**(3): p. 18-26.
47. Federici, J.F., et al., *THz imaging and sensing for security applications—explosives, weapons and drugs*. Semiconductor Science and Technology, 2005. **20**(7): p. S266.
48. Molter, D., et al., *Mail Inspection Based on Terahertz Time-Domain Spectroscopy*. Applied Sciences, 2021. **11**(3): p. 950.
49. Ok, G., et al., *High-speed terahertz imaging toward food quality inspection*. Appl Opt, 2014. **53**(7): p. 1406-12.
50. Stubling, E.M., et al., *Application of a robotic THz imaging system for sub-surface analysis of ancient human remains*. Sci Rep, 2019. **9**(1): p. 3390.

51. Wilke, I., et al., *Time-domain Terahertz spectroscopy as a diagnostic tool for the electrodynamic properties of high temperature superconductors*. *Physica C: Superconductivity*, 2000. **341**: p. 2271-2272.
52. Lee, H.-T., et al., *Measuring Complex Refractive Indices of a Nanometer-Thick Superconducting Film Using Terahertz Time-Domain Spectroscopy with a 10 Femtoseconds Pulse Laser*. *Crystals*, 2021. **11**(6): p. 651.
53. Mackenzie, D.M., et al., *Quality assessment of terahertz time-domain spectroscopy transmission and reflection modes for graphene conductivity mapping*. *Optics express*, 2018. **26**(7): p. 9220-9229.
54. Whelan, P.R., et al., *Conductivity mapping of graphene on polymeric films by terahertz time-domain spectroscopy*. *Optics express*, 2018. **26**(14): p. 17748-17754.
55. Whelan, P.R., et al., *Case studies of electrical characterisation of graphene by terahertz time-domain spectroscopy*. *2D Materials*, 2021. **8**(2): p. 022003.
56. Picometrix. *T-Ray 4000 TD-THz system*. 2007 [cited 2021; Available from: https://www.4science.net/goods/detail.do?glt_no=18270].
57. Abraham, E., et al. *A wavefront analyzer for terahertz time-domain spectrometers*. in *2017 42nd International Conference on Infrared, Millimeter, and Terahertz Waves (IRMMW-THz)*. 2017. IEEE.
58. Tian, Y., et al., *Femtosecond-laser-driven wire-guided helical undulator for intense terahertz radiation*. *Nature Photonics*, 2017. **11**(4): p. 242-246.
59. Han, S.-P., et al., *Optical fiber-coupled InGaAs-based terahertz time-domain spectroscopy system*. *Optics letters*, 2011. **36**(16): p. 3094-3096.
60. Shurakov, A., Y. Lobanov, and G. Goltsman, *Superconducting hot-electron bolometer: from the discovery of hot-electron phenomena to practical applications*. *Superconductor Science and Technology*, 2015. **29**(2): p. 023001.
61. Dufour, D., et al., *Review of terahertz technology development at INO*. *Journal of Infrared, Millimeter, and Terahertz Waves*, 2015. **36**(10): p. 922-946.
62. Zolliker, P., et al., *Real-Time High Resolution THz Imaging with a Fiber-Coupled Photo Conductive Antenna and an Uncooled Microbolometer Camera*. *Sensors*, 2021. **21**(11): p. 3757.
63. Qi, L., et al., *Antenna-Coupled Titanium Microbolometers: Application for Precise Control of Radiation Patterns in Terahertz Time-Domain Systems*. *Sensors*, 2021. **21**(10): p. 3510.
64. Oden, J., et al., *Imaging of broadband terahertz beams using an array of antenna-coupled microbolometers operating at room temperature*. *Optics express*, 2013. **21**(4): p. 4817-4825.
65. SwissTerahertz. *RIGI Camera uncooled real-time THz imager*. 2021; Available from: <https://www.swissterahertz.com/rigicamera>.
66. Kanda, N., et al., *Real-time broadband terahertz spectroscopic imaging by using a high-sensitivity terahertz camera*. *Scientific reports*, 2017. **7**(1): p. 1-10.

67. Nemoto, N., et al., *High-sensitivity and broadband, real-time terahertz camera incorporating a micro-bolometer array with resonant cavity structure*. IEEE Transactions on Terahertz Science and Technology, 2015. **6**(2): p. 175-182.
68. Lee, Y.-S., *Principles of terahertz science and technology*. Vol. 170. 2009: Springer Science & Business Media.
69. Yang, J., S. Ruan, and M. Zhang, *Real-time, continuous-wave terahertz imaging by a pyroelectric camera*. Chinese optics letters, 2008. **6**(1): p. 29-31.
70. Spiricon. *Pyrocam IIIHR Beam Profiling Camera*. 2021; Available from: <https://www.ophiropt.com/laser--measurement/beam-profilers/products/Beam-Profiling/Camera-Profiling-with-BeamGage/Pyrocam-IIIHR>.
71. Müller, R., et al., *Characterization of a large-area pyroelectric detector from 300 GHz to 30 THz*. Journal of Infrared, Millimeter, and Terahertz Waves, 2015. **36**(7): p. 654-661.
72. Globisch, B., et al., *Absolute terahertz power measurement of a time-domain spectroscopy system*. Optics letters, 2015. **40**(15): p. 3544-3547.
73. Müller, R., et al., *Novel detectors for traceable THz power measurements*. Journal of Infrared, Millimeter, and Terahertz Waves, 2014. **35**(8): p. 659-670.
74. Koulouklidis, A.D., et al., *Observation of extremely efficient terahertz generation from mid-infrared two-color laser filaments*. Nature communications, 2020. **11**(1): p. 1-8.
75. Li, Y., et al., *Strong terahertz radiation from relativistic laser interaction with solid density plasmas*. Applied Physics Letters, 2012. **100**(25): p. 254101.
76. Auston, D.H., K.P. Cheung, and P.R. Smith, *Picosecond photoconducting Hertzian dipoles*. Applied physics letters, 1984. **45**(3): p. 284-286.
77. Mitrofanov, O., et al., *Photoconductive terahertz near-field detector with a hybrid nanoantenna array cavity*. ACS Photonics, 2015. **2**(12): p. 1763-1768.
78. Bashirpour, M., et al., *Improvement of terahertz photoconductive antenna using optical antenna array of ZnO nanorods*. Scientific reports, 2019. **9**(1): p. 1-8.
79. Yardimci, N.T. and M. Jarrahi, *High sensitivity terahertz detection through large-area plasmonic nano-antenna arrays*. Scientific reports, 2017. **7**(1): p. 1-8.
80. Turan, D., N.T. Yardimci, and M. Jarrahi, *Plasmonics-enhanced photoconductive terahertz detector pumped by Ytterbium-doped fiber laser*. Optics express, 2020. **28**(3): p. 3835-3845.
81. Lepeshov, S., et al., *Boosting terahertz photoconductive antenna performance with optimised plasmonic nanostructures*. Scientific reports, 2018. **8**(1): p. 1-7.
82. Jooshesh, A., et al., *Plasmon-enhanced below bandgap photoconductive terahertz generation and detection*. Nano letters, 2015. **15**(12): p. 8306-8310.
83. Ghorbani, S., et al., *Thin film tandem nanoplasmonic photoconductive antenna for high performance terahertz detection*. Superlattices and Microstructures, 2018. **120**: p. 598-604.
84. Henmann, M., et al., *Towards multi-channel time-domain terahertz imaging with photoconductive antennas*. 2002.

85. Brahm, A., et al. *128 channel THz ultrashort pulse system*. in *2009 34th International Conference on Infrared, Millimeter, and Terahertz Waves*. 2009. IEEE.
86. Brahm, A., et al. *Development of a multichannel lock-in amplifier for terahertz time-domain systems*. in *2012 37th International Conference on Infrared, Millimeter, and Terahertz Waves*. 2012. IEEE.
87. van der Valk, N.C., T. Wenckebach, and P.C. Planken, *Full mathematical description of electro-optic detection in optically isotropic crystals*. *JOSA B*, 2004. **21**(3): p. 622-631.
88. Pradarutti, B., et al., *Multichannel balanced electro-optic detection for Terahertz imaging*. *Optics express*, 2007. **15**(26): p. 17652-17660.
89. Wu, Q., T. Hewitt, and X.C. Zhang, *Two-dimensional electro-optic imaging of THz beams*. *Applied Physics Letters*, 1996. **69**(8): p. 1026-1028.
90. Wang, X., et al., *Terahertz real-time imaging with balanced electro-optic detection*. *Optics Communications*, 2010. **283**(23): p. 4626-4632.
91. Matsubara, E., M. Nagai, and M. Ashida, *Ultrabroadband coherent electric field from far infrared to 200 THz using air plasma induced by 10 fs pulses*. *Applied Physics Letters*, 2012. **101**(1): p. 011105.
92. Karpowicz, N., et al., *Coherent heterodyne time-domain spectrometry covering the entire "terahertz gap"*. *Applied Physics Letters*, 2008. **92**(1): p. 011131.
93. Wang, T., et al., *Linearity of air-biased coherent detection for terahertz time-domain spectroscopy*. *Journal of Infrared, Millimeter, and Terahertz Waves*, 2016. **37**(6): p. 592-604.
94. Granja, A.B., et al. *Ultra-Broadband W-Band Balanced Schottky Diode Envelope Detector for High-Data Rate Communication Systems*. in *2018 43rd International Conference on Infrared, Millimeter, and Terahertz Waves (IRMMW-THz)*. 2018. IEEE.
95. Rettich, F., et al., *Field intensity detection of individual terahertz pulses at 80 MHz repetition rate*. *Journal of Infrared, Millimeter, and Terahertz Waves*, 2015. **36**(7): p. 607-612.
96. Han, S.-P., et al., *InGaAs Schottky barrier diode array detector for a real-time compact terahertz line scanner*. *Optics Express*, 2013. **21**(22): p. 25874-25882.
97. TopticaPhotonics. *Terahertz Technologies Systems and Accessories*. Available from: https://www.toptica.com/fileadmin/Editors_English/11_brochures_datasheets/01_brochures/toptica_BR_Terahertz_Technologies.pdf.
98. Quimby, R.S., *Photonics and lasers, an Introduction, Chapter 14.4.2 - Schottky Photodiode*. 2006.
99. Semenov, A., et al., *Application of zero-bias quasi-optical Schottky-diode detectors for monitoring short-pulse and weak terahertz radiation*. *IEEE Electron Device Letters*, 2010. **31**(7): p. 674-676.

100. Han, S.-P., et al. *Terahertz imaging using InGaAs Schottky barrier diode array detectors*. in *2013 38th International Conference on Infrared, Millimeter, and Terahertz Waves (IRMMW-THz)*. 2013. IEEE.
101. Ouyang, C., et al., *Terahertz strong-field physics in light-emitting diodes for terahertz detection and imaging*. *Communications Physics*, 2021. **4**(1): p. 1-9.
102. Knap, W., et al., *Field effect transistors for terahertz detection: Physics and first imaging applications*. *Journal of Infrared, Millimeter, and Terahertz Waves*, 2009. **30**(12): p. 1319-1337.
103. Öjefors, E., et al., *Terahertz imaging detectors in CMOS technology*. *Journal of Infrared, Millimeter, and Terahertz Waves*, 2009. **30**(12): p. 1269-1280.
104. Teppe, F., et al., *Plasma wave resonant detection of femtosecond pulsed terahertz radiation by a nanometer field-effect transistor*. *Applied Physics Letters*, 2005. **87**(2): p. 022102.
105. El Fatimy, A., et al., *Plasma wave field effect transistor as a resonant detector for 1 terahertz imaging applications*. *Optics Communications*, 2009. **282**(15): p. 3055-3058.
106. Ikamas, K., et al., *Silicon field effect transistor as the nonlinear detector for terahertz autocorellators*. *Sensors*, 2018. **18**(11): p. 3735.
107. Verghese, S., et al., *Generation and detection of coherent terahertz waves using two photomixers*. *Applied Physics Letters*, 1998. **73**(26): p. 3824-3826.
108. Safian, R., G. Ghazi, and N. Mohammadian, *Review of photomixing continuous-wave terahertz systems and current application trends in terahertz domain*. *Optical Engineering*, 2019. **58**(11): p. 110901.
109. Kaveev, A., E. Kaveeva, and E. Adaev, *Pulse shape measurement using Golay detector*. *Journal of Infrared, Millimeter, and Terahertz Waves*, 2012. **33**(3): p. 306-318.
110. Herrmann, M., et al. *Multi-channel signal recording with photoconductive antennas for THz imaging*. in *Proceedings, IEEE Tenth International Conference on Terahertz Electronics*. 2002. IEEE.
111. Brahm, A., et al., *Multichannel terahertz time-domain spectroscopy system at 1030 nm excitation wavelength*. *Optics express*, 2014. **22**(11): p. 12982-12993.
112. Ho, I.-C., X. Guo, and X.-C. Zhang, *Design and performance of reflective terahertz air-biased-coherent-detection for time-domain spectroscopy*. *Optics express*, 2010. **18**(3): p. 2872-2883.
113. MenloSystems. *TERA8-1 THz-Antennas for 800nm*. 2019 april 15, 2020]; Available from: https://www.menlosystems.com/assets/datasheets/THz-Time-Domain-Solutions/MENLO_TERA8-1-D-EN_2019-12_3w.pdf.
114. Holoeye, *PLUTO-2 PHASE ONLY SPATIAL LIGHT MODULATOR (REFLECTIVE)*. 2020.
115. Lin, Y.-H., Y.-J. Wang, and V. Reshetnyak, *Liquid crystal lenses with tunable focal length*. *Liquid Crystals Reviews*, 2017. **5**(2): p. 111-143.
116. Carcolé, E., J. Campos, and S. Bosch, *Diffraction theory of Fresnel lenses encoded in low-resolution devices*. *Applied optics*, 1994. **33**(2): p. 162-174.

117. Leach, J., et al., *Interactive approach to optical tweezers control*. Applied optics, 2006. **45**(5): p. 897-903.
118. Swanson, G.J., *Binary optics technology: theoretical limits on the diffraction efficiency of multilevel diffractive optical elements*. 1991, MASSACHUSETTS INST OF TECH LEXINGTON LINCOLN LAB.
119. Gongjian, Z., Z. Man, and Z. Yang, *Wave front control with SLM and simulation of light wave diffraction*. Optics express, 2018. **26**(26): p. 33543-33564.
120. Beck, M., et al., *High-speed THz spectroscopic imaging at ten kilohertz pixel rate with amplitude and phase contrast*. Opt Express, 2019. **27**(8): p. 10866-10872.
121. Watts, C.M., et al., *Terahertz compressive imaging with metamaterial spatial light modulators*. Nature Photonics, 2014. **8**(8): p. 605-609.
122. Zanotto, L., et al., *Time-domain terahertz compressive imaging*. Opt Express, 2020. **28**(3): p. 3795-3802.
123. Mohr, T., et al., *Two-dimensional tomographic terahertz imaging by homodyne self-mixing*. Opt Express, 2015. **23**(21): p. 27221-9.
124. Song, H.-J. and T. Nagatsuma, *Present and Future of Terahertz Communications*. IEEE Transactions on Terahertz Science and Technology, 2011. **1**(1): p. 256-263.
125. Akyildiz, I.F., J.M. Jornet, and C. Han, *Terahertz band: Next frontier for wireless communications*. Physical Communication, 2014. **12**: p. 16-32.
126. Mittleman, D.M., *Twenty years of terahertz imaging*. Optics express, 2018. **26**(8): p. 9417-9431.
127. Quast, H. and T. Loffler. *Towards real-time active THz range imaging for security applications*. in *2009 International Conference on Electromagnetics in Advanced Applications*. 2009. IEEE.
128. Sadwick, L.P., et al., *Development of terahertz endoscopic system for cancer detection*, in *Terahertz, RF, Millimeter, and Submillimeter-Wave Technology and Applications IX*. 2016.
129. Sun, Q., et al., *Recent advances in terahertz technology for biomedical applications*. Quant Imaging Med Surg, 2017. **7**(3): p. 345-355.
130. Park, S.J., et al., *Sensing viruses using terahertz nano-gap metamaterials*. Biomed Opt Express, 2017. **8**(8): p. 3551-3558.
131. Zhang, R., et al., *Terahertz Microfluidic Metamaterial Biosensor for Sensitive Detection of Small-Volume Liquid Samples*. IEEE Transactions on Terahertz Science and Technology, 2019. **9**(2): p. 209-214.
132. Miao, X., et al., *Discriminating the Mineralogical Composition in Drill Cuttings Based on Absorption Spectra in the Terahertz Range*. Appl Spectrosc, 2017. **71**(2): p. 186-193.
133. Fukunaga, K., et al. *Terahertz imaging systems: a non-invasive technique for the analysis of paintings*. in *O3A: Optics for Arts, Architecture, and Archaeology II*. 2009. International Society for Optics and Photonics.

134. Schiselski, M., et al. *A planar Schottky diode based integrated THz detector for fast electron pulse diagnostics*. in *2016 IEEE MTT-S International Microwave Symposium (IMS)*. 2016. IEEE.
135. Roggenbuck, A., et al., *Using a fiber stretcher as a fast phase modulator in a continuous wave terahertz spectrometer*. *JOSA B*, 2012. **29**(4): p. 614-620.
136. Bartels, A., et al., *Ultrafast time-domain spectroscopy based on high-speed asynchronous optical sampling*. *Review of Scientific Instruments*, 2007. **78**(3): p. 035107.
137. Hebling, J., et al., *High-power THz generation, THz nonlinear optics, and THz nonlinear spectroscopy*. *IEEE Journal of Selected Topics in Quantum Electronics*, 2008. **14**(2): p. 345-353.
138. Yang, Z., et al., *Large-size bulk and thin-film stilbazolium-salt single crystals for nonlinear optics and THz generation*. *Advanced Functional Materials*, 2007. **17**(13): p. 2018-2023.
139. Lu, X. and X.-C. Zhang, *Balanced terahertz wave air-biased-coherent-detection*. *Applied Physics Letters*, 2011. **98**(15): p. 151111.
140. Maki, K.-i. and C. Otani, *Terahertz beam steering and frequency tuning by using the spatial dispersion of ultrafast laser pulses*. *Optics Express*, 2008. **16**(14): p. 10158-10169.
141. Llombart, N., et al., *Confocal ellipsoidal reflector system for a mechanically scanned active terahertz imager*. *IEEE Transactions on Antennas and Propagation*, 2010. **58**(6): p. 1834-1841.
142. Guerboukha, H., et al., *Supplementary Information for: Super-resolution Orthogonal Deterministic Imaging Technique for Terahertz Subwavelength Microscopy*.
143. Guerboukha, H., K. Nallappan, and M. Skorobogatiy, *Exploiting k-space/frequency duality toward real-time terahertz imaging*. *Optica*, 2018. **5**(2): p. 109-116.
144. Carranza, I.E., et al., *Terahertz metamaterial absorbers implemented in CMOS technology for imaging applications: scaling to large format focal plane arrays*. *IEEE Journal of Selected Topics in Quantum Electronics*, 2016. **23**(4): p. 1-8.
145. Skorobogatiy, M., *Linear rotary optical delay lines*. *Optics express*, 2014. **22**(10): p. 11812-11833.
146. Jooshesh, A., et al., *Plasmon-enhanced LT-GaAs/AlAs heterostructure photoconductive antennas for sub-bandgap terahertz generation*. *Optics express*, 2017. **25**(18): p. 22140-22148.
147. Lavrukhin, D., et al., *Terahertz photoconductive emitter with dielectric-embedded high-aspect-ratio plasmonic grating for operation with low-power optical pumps*. *AIP Advances*, 2019. **9**(1): p. 015112.
148. Lavrukhin, D., et al., *Shaping the spectrum of terahertz photoconductive antenna by frequency-dependent impedance modulation*. *Semiconductor Science and Technology*, 2019. **34**(3): p. 034005.
149. Holoeye. *PLUTO-2.1 LCOS SPATIAL LIGHT MODULATOR PHASE ONLY (REFLECTIVE)*. 2021; Available from: <https://holoeye.com/slm-pluto-phase-only/>.

150. FEMTO. *LOW-FREQUENCY VOLTAGE AMPLIFIERS SERIES DLPVA*. 2021; Available from: <https://www.femto.de/en/products/voltage-amplifiers/variable-gain-100-khz-dlpva.html>.
151. Zhang, J., et al., *Contribution assessment of antenna structure and in-gap photocurrent in terahertz radiation of photoconductive antenna*. Journal of Applied Physics, 2018. **124**(5): p. 053107.
152. Paz-Martínez, G., et al., *Focus and Alignment Tolerance in a Photoconductive Terahertz Source*. Journal of Infrared, Millimeter, and Terahertz Waves, 2015. **36**(9): p. 830-837.
153. Carthy, J.L., et al., *Terahertz focusing and polarization control in large-area bias-free semiconductor emitters*. Journal of Infrared, Millimeter, and Terahertz Waves, 2018. **39**(3): p. 223-235.
154. Cliffe, M., et al., *Generation of longitudinally polarized terahertz pulses with field amplitudes exceeding 2 kV/cm*. Applied Physics Letters, 2014. **105**(19): p. 191112.
155. Gregory, I.S., et al., *Optimization of photomixers and antennas for continuous-wave terahertz emission*. IEEE Journal of Quantum electronics, 2005. **41**(5): p. 717-728.
156. Ralph, S.E. and D. Grischkowsky, *Trap-enhanced electric fields in semi-insulators: The role of electrical and optical carrier injection*. Applied physics letters, 1991. **59**(16): p. 1972-1974.
157. Cao, Y., et al., *Additive manufacturing of highly reconfigurable plasmonic circuits for terahertz communications*. Optica, 2020. **7**(9): p. 1112-1125.
158. Guerboukha, H., et al., *High-volume rapid prototyping technique for terahertz metallic metasurfaces*. Optics Express, 2021. **29**(9): p. 13806-13814.
159. Yan, G., et al., *Resonant THz sensor for paper quality monitoring using THz fiber Bragg gratings*. Optics letters, 2013. **38**(13): p. 2200-2202.
160. Jin, Y.-S., G.-J. Kim, and S.-G. Jeon, *Terahertz dielectric properties of polymers*. Journal of the Korean Physical Society, 2006. **49**(2): p. 513-517.
161. Ljungblad, U.B., et al. *A high-end mask writer using a spatial light modulator*. in *MOEMS Display and Imaging Systems III*. 2005. International Society for Optics and Photonics.
162. Yunfeng, J., et al. *Multiple optical tweezers generated from phase Fresnel lens array*. in *2012 Photonics Global Conference (PGC)*. 2012. IEEE.
163. Rastani, K., et al., *Binary phase Fresnel lenses for generation of two-dimensional beam arrays*. Applied optics, 1991. **30**(11): p. 1347-1354.
164. Hasegawa, S., Y. Hayasaki, and N. Nishida, *Holographic femtosecond laser processing with multiplexed phase Fresnel lenses*. Optics Letters, 2006. **31**(11): p. 1705-1707.
165. SpectraPhysics, *Mai Tai® One Box Ti:Sapphire Ultrafast Lasers*. 2021.
166. BatopOptoelectronics, *Instruction manual and data sheet iPCA-21-05-1000-800-h*. 2021.
167. Park, K.Y., N. Wiwatcharagoses, and P. Chahal. *Wafer-level integration of micro-lens for THz focal plane array application*. in *2013 IEEE 63rd Electronic Components and Technology Conference*. 2013. IEEE.

168. Tanabe, T., et al., *Terahertz Detection of Halogen Additive-Containing Plastics*. Optics and Photonics Journal, 2020. **10**(12): p. 265-272.
169. Peng, H.-Y., et al., *Terahertz complex refractive index properties of acrylonitrile butadiene styrene with rice husk ash and its possible applications in 3D printing techniques*. Optical Materials Express, 2021. **11**(9): p. 2777-2786.
170. Rønne, C., et al., *Investigation of the temperature dependence of dielectric relaxation in liquid water by THz reflection spectroscopy and molecular dynamics simulation*. The Journal of chemical physics, 1997. **107**(14): p. 5319-5331.
171. Lombart, N., et al., *Silicon micromachined lens antenna for THz integrated heterodyne arrays*. IEEE Transactions on Terahertz Science and Technology, 2013. **3**(5): p. 515-523.